Department of Physics
University of Jyväskylä
Research Report No. 12/2008

# HIGH PRECISION $Q_{\mathrm{EC}}$ VALUE MEASUREMENTS OF SUPERALLOWED $0^+ \rightarrow 0^+$ BETA DECAYS WITH JYFLTRAP

by
**Tommi Eronen**

Academic Dissertation
for the Degree of
Doctor of Philosophy

*To be presented, by permission of the*
*Faculty of Mathematics and Natural Sciences*
*of the University of Jyväskylä,*
*for public examination in Auditorium FYS-1 of the*
*University of Jyväskylä on December 16, 2008*
*at 12 o'clock noon*

Jyväskylä, Finland
December 2008

# Preface

The work reported in this thesis has been carried out in the IGISOL group during the years 2003-2008 at the Department of Physics in the University of Jyväskylä, Finland.

I want to sincerely thank my supervisors Prof. Juha Äystö and Dr. Ari Jokinen for all their encouragement and guidance. I am in gratitude to all past and present JYFLtrappers, especially to Dr. Ulrike Hager for all efforts in commissioning JYFLTRAP, Dr. Sami Rinta-Antila for his wisdom in aspects of technical design and MSc Jani Hakala for realizing all my requested features for the control system and for helping me out in computer programming. MSc Viki-Veikko Elomaa and Dr. Saidur Rahaman have been invaluable help in running and developing the trap setup. Dr. Christine Weber and Dr. Anu Kankainen are acknowledged for their critical eye for manuscripts.

I would also like to thank the rest of the IGISOL group members for participating in experiments. Msc Antti Saastamoinen has always kept the IGISOL up and running, Dr. Thomas Kessler introduced me to the wonderful world of laser lights and Dr. Iain Moore for his english corrections and all expertise.

In general, I would like to thank the whole staff of the Department of Physics for providing a pleasant working atmosphere.

I am also very grateful of collaboration with Prof. John Hardy who did the major (re)writing of the publications II and III and enlightened me on various topics in the field of superallowed beta emitters.

I want to thank my parents for encouraging me in my physics studies. Finally I warmly thank MSc Jonna Piilonen for all her support in this thesis work and in everyday life and bearing with me even when long experiments have occupied me around the clock.

Jyväskylä, December 2008

Tommi Eronen

**Author**

Tommi Eronen
Department of Physics
University of Jyväskylä
Finland

**Supervisors**

Prof. Dr. Juha Äystö
Department of Physics
University of Jyväskylä
Finland

Dr. Ari Jokinen
Department of Physics
University of Jyväskylä
Finland

**Reviewers**

Prof. Dr. Klaus Blaum
Max-Planck-Institut für Kernphysik
Heidelberg
Germany

Prof. Dr. Jens Dilling
University of British Columbia
Deparment of Physics and Astronomy
Vancouver, Canada

**Opponent**

Prof. Dr. Georg Bollen
National Superconducting Cyclotron Laboratory
Michigan State University
USA

# Abstract

Eronen, Tommi
High precision $Q_{\mathrm{EC}}$ value measurements of superallowed $0^+ \rightarrow 0^+$ beta decays with JYFLTRAP
Jyväskylä: University of Jyväskylä, 2008, xiv + 109 pp.
Department of Physics, University of Jyväskylä, Research Report 12/2008.
ISBN 978-951-39-3405-7
ISSN 0075-465X

For this thesis work, several $Q_{\mathrm{EC}}$ values of superallowed $\beta$ emitters having isospin $T = 1$ were measured using the JYFLTRAP Penning trap setup at the IGISOL facility in the Accelerator Laboratory of the University of Jyväskylä. The $Q_{\mathrm{EC}}$ values of eight $0^+ \rightarrow 0^+$ superallowed transitions of $^{26}\mathrm{Al}^m$, $^{26}$Si, $^{42}$Sc, $^{42}$Ti, $^{46}$V, $^{50}$Mn, $^{54}$Co and $^{62}$Ga were obtained with sub-keV precision. The results of these measurements have been published in three letter articles with exception of $^{42}$Ti which will be published in the near future. In the cases of $^{62}$Ga, $^{26}$Si and $^{42}$Ti the $Q_{\mathrm{EC}}$ value precision were improved dramatically over the existing values. In other cases the already well-known $Q_{\mathrm{EC}}$ values were checked. Especially the $^{46}$V case turned out to be controversial due to large deviation between Penning trap and old reaction-based measurements.

Since some of the measured nuclei (namely $^{50}$Mn and $^{54}$Co) have isomeric contaminant states, a novel isomeric cleaning procedure was developed and is now in routine use at JYFLTRAP. Also several improvements and optimizations to the Penning trap setup were done during the course of this thesis work The implementation of the ion motion excitation with time-separated oscillatory RF-fields was one major improvement that increased the precision for the very short-lived nuclei as the forementioned $^{50}$Mn and $^{54}$Co. Similar offsets than in $^{46}$V case were reported in these two cases as well.

The new $Q_{\mathrm{EC}}$ values significantly increased the $\mathcal{F}t$ values in these three cases and supported the re-evaluation of the theoretical– especially the isospin-mixing – corrections that are needed for obtaining $\mathcal{F}t$ values. Currently, the world-average $\mathcal{F}t$ value for the 13 well known superallowed $T = 1$ $\beta$ emitters are consistent with normalised $\chi^2$ of 0.22. The derived $V_{\mathrm{ud}}$ value of the Cabibbo-Kobayashi-Maskawa (CKM) quark

mixing matrix from superallowed $\beta$ decay is now $|V_{\rm ud}| = 0.97408(26)$ and the top-row square-sum of the CKM matrix 0.9998(10), which is in perfect agreement with Standard Model expectations.

# Acknowledgments

This work has been supported by the EU within the 6th framework programme "Integrating Infrastructure Initiative — Transnational Access", Contract Number: 506065 (EURONS, JRA TRAPSPEC) and within the NIPNET RTD project under Contract No. HPRI-CT-2001-50034. We also acknowledge support from the Academy of Finland under the Finnish Centre of Excellence Programmes 2000–2005 (Project No. 44875, Nuclear and Condensed Matter Physics Programme at JYFL) and 2006–2011 (Project No. 213503, Nuclear and Accelerator Based Physics Programme at JYFL).

Author of this work expresses gratitude for financial support from the rector of the University of Jyväskylä and from Academy of Finland under the Centre of Excellence Programmes. The Graduate School in Particle and Nuclear Physics (GRASPANP) is acknowledged for financing travels to numerous schools and conferences.

# List of Publications

I *Q-value of the superallowed $\beta$ decay of $^{62}Ga$*
T. Eronen, V.-V. Elomaa, U. Hager, J. Hakala, A. Jokinen, A. Kankainen, I. Moore, H. Penttilä, S. Rahaman, S. Rinta-Antila, A. Saastamoinen, T. Sonoda, J. Äystö, A. Bey, B. Blank, G. Canchel, C. Dossat, J. Giovinazzo, I. Matea and N. Adimi
Phys. Lett. B **636**, 191 (2006), arXiv:nucl-ex/0512010.

II *Q Values of the Superallowed $\beta$ Emitters $^{26}Al^m$, $^{42}Sc$, and $^{46}V$ and Their Impact on $V_{\rm ud}$ and the Unitarity of the Cabibbo-Kobayashi-Maskawa Matrix*
T. Eronen, V. Elomaa, U. Hager, J. Hakala, A. Jokinen, A. Kankainen, I. Moore, H. Penttilä, S. Rahaman, J. Rissanen, A. Saastamoinen, T. Sonoda, and J. Äystö
Phys. Rev. Lett. **97**, 232501 (2006), arXiv:nucl-ex/0606035.

III *$Q_{\rm EC}$ Values of the Superallowed $\beta$ Emitters $^{50}Mn$ and $^{54}Co$*
T. Eronen, V.-V. Elomaa, U. Hager, J. Hakala, J. C. Hardy, A. Jokinen, A. Kankainen, I. D. Moore, H. Penttilä, S. Rahaman, S. Rinta-Antila, J. Rissanen, A. Saastamoinen, T. Sonoda, C. Weber, and J. Äystö
Phys. Rev. Lett. **100**, 132502 (2008), arXiv:nucl-ex/0712.3463.

IV *Preparing isomerically pure beams of short-lived nuclei at JYFLTRAP*
T. Eronen, V.-V. Elomaa, U. Hager, J. Hakala, A. Jokinen, A. Kankainen, S. Rahaman, J. Rissanen, C. Weber and J. Äystö
(EMIS2007 Conference Proceedings)
Nucl. Instrum. Meth. Phys. Res. B **266**, 4527 (2008), arXiv:nucl-ex/0801.2904

V *JYFLTRAP: mass spectrometry and isomerically clean beams*
T. Eronen, V.-V. Elomaa, U. Hager, J. Hakala, A. Jokinen, A. Kankainen, S. Rahaman, J. Rissanen, C. Weber, J. Äystö and the IGISOL group
(XXX Mazurian Lakes conference proceedings)
Acta Phys. Pol. B **39**, 445 (2008).

VI *The mass and the $Q_{\rm EC}$ value of $^{26}Si$*
T. Eronen, V.-V. Elomaa, U. Hager, J. Hakala, A. Jokinen, A. Kankainen, T. Kessler, I. D. Moore, S. Rahaman, J. Rissanen, C. Weber, and J. Äystö
submitted to Phys. Rev. C (2008).

The author has performed data analysis in all publications. The author is the main writer of publications IV–VI and has helped writing publications I–III.

# Contents

# List of Tables

# List of Figures

# 1 Introduction

Nuclei with approximately the same number of protons and neutrons are studied extensively due to their symmetry properties. Those are used for testing fundamental interactions, nuclear structure calculations and also for astrophysics. In the field of fundamental interactions, the superallowed $\beta$ decays between isobaric analog states having spin-parity of $J^\pi = 0^+$ and isospin $T = 1$ provide valuable information for the testing of the Standard Model of particle physics. One of the three experimental quantities required for such tests is the decay energy, the $Q_{\mathrm{EC}}$ value. The two other experimental quantities are the half-life and the branching ratio to the isobaric analog state. The data from superallowed beta decays enable the most precise determination of the $V_{\mathrm{ud}}$ element of the Cabibbo-Kobayashi-Maskawa (CKM) quark mixing matrix using the conserved vector current (CVC) hypothesis [1].

The $Q_{\mathrm{EC}}$ values of superallowed $\beta$ emitters have conventionally been measured using nuclear reactions by determining the decay energy from reaction kinematics. In the last half a decade, Penning trap spectrometers have also become available for determining the $Q_{\mathrm{EC}}$ values. By measuring the masses of the parent and daughter nuclei the $Q_{\mathrm{EC}}$ value can be determined from the mass difference or even more directly from the mass ratio of the parent and daughter nuclei.

The mass difference measurement with an on-line Penning trap setup such as JYFLTRAP at the Accelerator Laboratory of the University of Jyväskylä is a delicate process. The trapped sample should only consist of the ions of interest. In several cases there are isobaric and isomeric contaminations present which need to be removed. As some of the superallowed $\beta$ emitters are very short-lived, the whole measurement procedure needs to be rather fast.

In addition to mass and $Q_{\mathrm{EC}}$ value measurements, Penning traps can be used to provide high-purity radioactive ion beams for decay spectroscopy. At JYFLTRAP, branching ratios and half-lives of superallowed $\beta$ emitters have been measured by using the trap as a high-resolution mass filter.

# 2 Physics motivation

## 2.1 Nuclear mass and binding energy

Atoms consist of nucleons (bound protons and neutrons) and of electrons. The protons and neutrons form the core of the atom which is commonly called nucleus. The electrons orbit around the nucleus. Most of the mass of an atom is in the nucleus and only a small fraction of the mass is due to that of electrons. An atom is a bound system. Removing any of the constituents from the atom will require energy to overcome the binding energy. It is therefore convenient to define a binding energy for an atom. If an atom consists of $Z$ protons and electrons and $N$ neutrons the total binding energy $B(Z,N)$ is the sum of the masses of the constituents minus the mass of the atom $M(Z,N)$:

$$B(Z,N) = Zm_p + Nm_n + Zm_e - M(Z,N), \tag{2.1}$$

where $m_p, m_n$ and $m_e$ are masses of a single proton, neutron and electron, respectively. Nuclear binding energies are on the MeV scale whereas atomic electron binding energies range from eV for simply charged ions to about one hundred keV for highly-charged bare heavy ions.

Several thousand isotopes each with different masses are known to exist. It is convenient to tabulate masses of different elements in tables according to their proton and neutron numbers. The present atomic mass standard is based on $^{12}$C which consists of six protons, neutrons and electrons, and its mass is defined to be 12 *atomic mass units*, u. The atomic masses of known isotopes with extrapolated values for a few unknown cases are tabulated in the Atomic Mass Evaluation, AME03 [2].

Since both of the nucleons — protons and neutrons — have almost the same mass, it is convenient to give atomic mass as a mass excess over the $A\times$u. Mass of an atom having $A$ nucleons and $Z$ protons is thus

$$M(A,Z) = A\mathrm{u} + \Delta(A,Z), \tag{2.2}$$

where $A = N + Z$ and $\Delta(A,Z)$ is the *mass excess* of an atom having $A$ nucleons and $Z$ protons. Isotopes with the same mass number are called *isobars* and the

mass differences between different isobars are rather small, on the order of MeV/$c^2$, compared to different mass numbers, approximately 1 GeV/$c^2$.

Other important quantities that are related to atomic masses are so-called $Q$ values. If isotope $A$ transforms into isotope $B$, the energy released in the process is the $Q$ value.

$$Q = (M_A - M_B)c^2, \tag{2.3}$$

where $M_A$ and $M_B$ are the masses of the atoms $A$ and $B$. If the $Q$ value is negative, the reaction can only proceed if energy amounting to $-Q$ or more is provided.

In addition to the ground state, a nucleus can exist in a long-living excited state [3]. These are called isomeric states and their lifetimes range from $10^{-9}$ s up to millions of years. Isomeric states are produced in any nuclear reactions such as in fusion or fission.

The vast majority of the nuclei that are presently known are radioactive and decay to other, more stable nuclei. The most common transmutation modes are alpha, proton and beta decays as well as spontaneous fission. Isomeric states usually decay to the ground state of the nucleus but also beta and alpha decaying isomers are common [4–6].

Transuranic nuclei typically $\alpha$ decay, that is, they emit $\alpha$ particles that are nuclei of $^4$He atoms. For instance, $^{233}$U is $\alpha$ active with a half-life of $1.6 \times 10^5$ years and decays to $^{229}$Th

$$^{233}_{92}\mathrm{U}_{141} \rightarrow ^{229}_{90}\mathrm{Th}_{139} + ^{4}_{2}\mathrm{He}_{2}. \tag{2.4}$$

In beta decay, one nucleon in the nucleus changes either from a proton to a neutron or vice versa. Nuclei that lie far from the valley of beta stability can in addition to $\beta$ decay, also decay by spontaneous nucleon emission. In the neutron deficient side of the nuclear chart spontaneous emission can occur if the proton binding energy is negative. Several proton emitters have been discovered and even direct mass measurements of proton emitters have been performed with Penning traps [7]. Proton emission half-lives are in a reasonable time scale ($>$ ms) due to hindrance caused by the Coulomb barrier. Recently, even two-proton emitters have been found [8]. Neutron radioactivity, on the other hand, has not been detected so far, perhaps due to its prompt character or the distance from the valley of stability on the neutron rich side which is more difficult to access in experiments.

A relatively common decay mode for heavy elements such as uranium is spontaneous fission. Here, a heavy nucleus splits into two medium-heavy fragments. Since a heavy nucleus has an excess amount of neutrons, fission fragments are neutron rich

**Table 2.1:** The particles of the Standard Model. Given are the three generations of quarks and leptons and the force mediating particles.

| **Matter particles** | Generation 1 | | Generation 2 | | Generation 3 | |
|---|---|---|---|---|---|---|
| Quarks | up | u | Charm | c | Top | t |
| | down | d | Strange | s | Bottom | b |
| Leptons | Electron neutrino | $\nu_e$ | Muon neutrino | $\nu_\mu$ | Tau neutrino | $\nu_\tau$ |
| | Electron | $e^-$ | Muon | $\mu^-$ | Tau | $\tau^-$ |

| **Force particles** | | interaction |
|---|---|---|
| Photon | $\gamma$ | Electromagnetic |
| Gauge bosons | $Z^0, W^\pm$ | Weak |
| Gluons | $g$ | Strong |

compared to the stable nucleus having the same mass number. The fission fragments undergo $\beta^-$ decays and some even $\beta$-delayed neutron emission before reaching the valley of stability.

## 2.2 Beta decay and the Standard Model

The Standard Model of Particle Physics is a theory that describes the strong, weak and electromagnetic interactions but does not include gravitation. The Standard Model is based on quantum electroweak theory and on quantum chromodynamics which describe interactions between all the experimentally observed particles. Two types of elementary matter particles exist: quarks and leptons, which are spin-$\frac{1}{2}$ particles, called fermions. In addition, there are three generations of particles. Ordinary matter consists only of the so-called first generation matter: up and down quarks, electrons and electron neutrinos. The force-mediating particles are spin-1 bosons. The electromagnetic force is mediated by massless photons, the weak force by either of the three gauge bosons, $W^\pm$ and $Z^0$ operating between quarks and leptons and the strong force is mediated with gluons between quarks. The Standard Model particles are summarised in table 2.1. The only particle that is predicted by the Standard Model but not yet experimentally found is the Higgs boson which plays a key role in explaining the origin of mass of elementary particles.

### 2.2.1 Weak interaction

As mentioned, the weak interaction affects both leptons and quarks. It is called the weak interaction since it is at least $10^{10}$ times weaker than the strong or the electromagnetic interactions. It is the only force that can change flavours of quarks, for instance an up-quark to a down-quark in $\beta^+$ decay or vice versa in $\beta^-$ decay. Effectively this means that one proton changes to a neutron and vice versa.

In $\beta^+$ decay a proton ($p$) inside a nucleus changes to a neutron ($n$) in the reaction

$$p \rightarrow n + e^+ + \nu_e, \tag{2.5}$$

where $e^+$ is positron (anti electron) and $\nu_e$ an electron-neutrino. $\beta^-$ decay is similar, in which a neutron inside the nucleus is converted into a proton

$$n \rightarrow p + e^- + \overline{\nu}_e, \tag{2.6}$$

where $e^-$ is an electron and $\overline{\nu}_e$ an electron anti-neutrino. It should be noted that a free proton is not radioactive (the known lower limit of proton lifetime is $4 \times 10^{23}$ years [9]) but a free neutron will $\beta$ decay to a proton (free neutron lifetime is about 15 min [10]). The $\beta$ decay is a three-body process, where in addition to charged particle emission (electron or anti-electron) there is also a neutral particle (neutrino or anti-neutrino) emitted. Thus, the amount of energy released in the reaction $Q$ value is distributed among all three particles involved.

Also related to $\beta$ decay is the electron capture process which occurs in parallel to $\beta^+$ decay. In this process, a nucleus captures one of the atomic electrons and a proton is converted to a neutron with a neutrino ($\nu_e$) emitted:

$$p + e^- \rightarrow n + \nu_e. \tag{2.7}$$

The energy released in a $\beta^+$ decay of the atom $(A, Z)$ to $(A, Z-1)$ is

$$Q\left(\beta^+\right) = \left[m(A, Z) - m(A, Z-1) - 2m_e\right] c^2, \tag{2.8}$$

where $m(A, Z)$ and $m(A, Z-1)$ are the masses of the parent and daughter atoms, respectively, and $m_e$ is the mass of an electron. The electron-capture $Q$ value, $Q_{\mathrm{EC}}$, is $2m_e c^2$ higher

$$Q_{\mathrm{EC}} = \left[m(A, Z) - m(A, Z-1)\right] c^2. \tag{2.9}$$

Thus in some cases the $\beta^+$ decay is not energetically possible however the electron capture can proceed. The $Q$ value of the $\beta^-$ decay of the atom $(A, Z)$ to $(A, Z+1)$ is

$$Q\left(\beta^-\right) = \left[m(A, Z) - m(A, Z+1)\right] c^2. \tag{2.10}$$

### 2.2.2 Allowed beta decay

In allowed $\beta$ decay the final state leptons are emitted in an s ($l = 0$) state relative to the nucleus so that orbital angular momentum of the leptons cannot change the nuclear total angular momentum. The emitted leptons can either couple their spins parallel ($S = 1$) or anti-parallel ($S = 0$), thus the nuclear angular momentum $J$ can change by 0 or 1. Decays with no angular momentum change are called *Fermi transitions* and those with angular momentum change of 1 are called *Gamow-Teller transitions*.

The $\beta$ decay transition probability is calculated using the Fermi golden rule

$$ft = \frac{K}{B_{\mathrm{F}} + B_{\mathrm{GT}}}, \tag{2.11}$$

where $K/(\hbar c)^6 = 2\pi^3 \hbar \ln 2/(m_e c^2)^5 = (8120.271 \pm 0.012)$ GeV$^{-4}$s, $f$ is the phase-space integral that contains the lepton kinematics and $t$ the half-life of the transition. The reduced transition probabilities $B_{\mathrm{F}}$ and $B_{\mathrm{GT}}$ are

$$B_{\mathrm{F}} = G_{\mathrm{V}}^2 \langle M_{\mathrm{F}} \rangle^2, \qquad B_{\mathrm{GT}} = G_{\mathrm{A}}^2 \langle M_{\mathrm{GT}} \rangle^2, \tag{2.12}$$

where $G_{\mathrm{V}}$ is the vector coupling constant which is determined from the conserved vector current hypothesis (CVC) and $G_{\mathrm{A}}$ the axial-vector coupling constant which is obtained from the partially conserved axial-vector current (PCAC) hypothesis.

The Fermi and Gamow-Teller matrix elements can be written

$$\langle M_{\mathrm{F}} \rangle^2 = \langle J_f M T_f T_{fz} | \mathbf{1} \sum_{k=1}^{A} t_{\pm}(k) | J_i M T_i T_{iz} \rangle \tag{2.13}$$

$$\langle M_{\mathrm{GT}} \rangle^2 = \frac{1}{2J_i + 1} \sum_{m M_i M_f} \left| \langle J_f M_f T_f T_{fz} | \sum_{k=1}^{A} \sigma_m(k) t_{\pm}(k) | J_i M_i T_i T_{iz} \rangle \right|^2 \tag{2.14}$$

where index $i$ stands for initial state and $j$ for final state, $J_i$ is the angular momentum of the initial nuclear state ($J_f$ for the final state), $T_i, T_{iz}$ the isospin quantum number of the initial state ($T_f, T_{fz}$ for the final state), $t_{\pm}(k)$ is the isospin raising and lowering operator and $\sigma_m$ the spin operator in spherical components $\sigma_m = \{\sigma_{-1}, \sigma_0, \sigma_{+1}\}$ and $\mathbf{1}$ unit operator [11].

Isospin in nuclear physics treats protons and neutrons bound in a nucleus as different states. The isospin quantum number is denoted with $T$. A proton has isospin projection $T_z = -\frac{1}{2}$ and neutron $T_z = +\frac{1}{2}$. The total isospin $z$-projection of the

nucleus, $T_z$, is the sum of isospin $z$-projections of all nucleons. Thus the $N = Z$ nuclei have $T_z = 0$. In general, the isospin $z$-component of a nucleus is written as

$$T_z = \frac{1}{2}(N - Z), \tag{2.15}$$

where $N$ and $Z$ are neutron and proton numbers of a nucleus, respectively. The isobars having the same same $T$ and different $T_z$ form isospin multiplets so that $T_z = T, T-1, \ldots, -T$. For example for $A = 46$ the isospin $T = 1$ nuclei are $^{46}$Cr ($T_z = -1$), $^{46}$V ($T_z = 0$) and $^{46}$Ti ($T_z = +1$).

A special case of the allowed beta decay is the *superallowed decay* between the isobaric analog states possessing the same quantum number $(T, J) = (T, 0)$ and parity $\pi = +$. The most extensively studied decays are between isospin $T = 1$ nuclei having $A \leq 74$ [1]. Since there is no spin nor parity change, the superallowed transition is purely of *Fermi* type. However, the parent $T = 1, J^\pi = 0^+$ state can also decay to other states with a Gamow-Teller type transition. As there is no Gamow-Teller contribution in a superallowed transition, the $ft$ value is written as

$$ft = \frac{K}{G_V^2 \left| M_{\mathrm{F}} \right|^2}. \tag{2.16}$$

The Fermi transitions are described by the operator

$$\mathbf{1} \sum_{k=1}^{A} t_{\pm}(k) = \mathbf{1} T_{\pm} = \mathbf{1}(T_x \pm \mathrm{i} T_y) \tag{2.17}$$

and thus the squared Fermi matrix element in transitions between isobaric analog states (same $T$) is given by

$$\begin{aligned} \langle M_{\mathrm{F}} \rangle^2 = \left| \langle JMTT_{fz} | \mathbf{1} \sum_{k=1}^{A} t_{\pm}(k) | JMTT_{iz} \rangle \right|^2 &= (T \mp T_{iz})(T \pm T_{iz} + 1) \\ &= T(T+1) - T_{iz} T_{fz}, \end{aligned} \tag{2.18}$$

where $T_{iz}$ and $T_{fz}$ are the isospin $z$-component of the initial and final nucleus, respectively. For superallowed $T = 1$ emitters the pure Fermi matrix element is

$$\langle M_{\mathrm{F}} \rangle^2 = 1(1+1) = 2 \quad \text{(superallowed } T = 1 \text{ emitters)}, \tag{2.19}$$

since either $T_{iz}$ or $T_{fz}$ is zero.

### Conserved vector current hypothesis

The conserved vector current hypothesis indicates that the $ft$ values of the $0^+ \rightarrow 0^+$ superallowed beta decays should be the same irrespective of the nucleus. The hypothesis asserts that the vector coupling constant $G_V$ is a true constant and not renormalized to another value in the nuclear medium. The $ft$ values are not exactly constants because isospin is not an exact symmetry in nuclei due to, for instance, Coulomb interaction between protons. Due to this, a few corrections have to be included.

The corrected $ft$-value for superallowed transitions, denoted $\mathcal{F}t$, is written as

$$\mathcal{F}t = ft\,(1+\delta_R')\,(1+\delta_{\rm NS}-\delta_C) = \frac{K}{2G_V^2\,(1+\Delta_R^V)}, \tag{2.20}$$

where the quantities inside the parenthesis ($\delta_R'$, $\delta_{\rm NS}$, $\delta_C$ and $\Delta_R^V$) are different corrections which are explained in more detail later in this section.

### Theoretical corrections

In order to meet the requirements of the constant vector current hypothesis the $ft$ values need to be corrected. These corrections modify the $ft$ values by about 1 %. The corrections need to be calculated with an accuracy of 10 % to be comparable with the current experimental uncertainties of the $ft$ values. The latest evaluation of the correction terms can be found from Ref. [12].

As the isospin is not an exact symmetry, the Fermi matrix element is modified as $\langle M_F\rangle^2 = |M_0|^2(1-\delta_C)$, where $M_0$ is the exact symmetry value $|M_0| = \sqrt{2}$ and $\delta_C$ the isospin-symmetry-breaking correction. In a second quantization formulation, the Fermi matrix element is written as

$$M_{\rm F} = \langle f|t_+|i\rangle = \sum_{\alpha,\beta}\langle f|a_\alpha^\dagger a_\beta|i\rangle\langle\alpha|t_+|\beta\rangle, \tag{2.21}$$

where $a_\alpha^\dagger$ creates a neutron in quantum state $\alpha$ and $a_\beta$ annihilates a proton in quantum state $\beta$. The single particle matrix element

$$\langle\alpha|t_+|\beta\rangle = \delta_{\alpha,\beta}\int_0^\infty R_\alpha^n(r)\,R_\beta^p(r)r^2dr \equiv \delta_{\alpha,\beta}\,r_\alpha. \tag{2.22}$$

If the radial functions are identical then $r_\alpha = 1$.

Equation (2.21) can be written as an $(A-1)$-particle system, $|\pi\rangle$,

$$M_{\mathrm{F}} = \sum_{\pi,\alpha} \langle f|a_\alpha^\dagger|\pi\rangle\langle\pi|a_\alpha|i\rangle r_\alpha^\pi. \tag{2.23}$$

If isospin is an exact symmetry the Hermicity $\langle\pi|a_\alpha|i\rangle = \langle f|a_\alpha^\dagger|\pi\rangle^*$ should be fulfilled.

The isospin-symmetry-breaking correction can be in first order divided in two independent parts

$$\delta_C = \delta_{C1} + \delta_{C2}, \tag{2.24}$$

where $\delta_{C1}$ arises from the non-Hermiticity of $a_\alpha$ and $a_\alpha^\dagger$ operators in Eq. (2.23) and $\delta_{C2}$ from the mismatch of $R_\alpha^n$ and $R_\beta^p$ radial functions in Eq. (2.22). Experimental information such as spectroscopic factors for neutron pickup [13], proton separation energy (amount of energy that is needed to separate a proton from the nucleus) of the decaying nucleus, neutron separation energy of the daughter nucleus [2] and coefficients of the isobaric mass multiplet equation (IMME) [14, 15] are needed to evaluate the correction.

The transition-dependent radiative correction is split into two parts $\delta_R'$ and $\delta_{\mathrm{NS}}$. The first, $\delta_R'$ is also known as the nucleus-dependent outer radiative correction, and is a function of the electron's energy and the charge of the daughter nucleus. It can be further divided as follows,

$$\delta_R' = \frac{\alpha}{2\pi}\left[\bar{g}(E_m) + \delta_2 + \delta_3 + \delta_{\alpha^2}\right], \tag{2.25}$$

where $\delta_2$ and $\delta_3$ are contributions of order $Z\alpha^2$ and $Z^2\alpha^3$, respectively. The function $\bar{g}(E_m)$ is averaged over the electron spectrum and was first defined by Sirlin [16]. $\delta_{\alpha^2}$ is difference between definitions of $\delta_R'$ given in Ref. [12].

The nuclear structure dependent correction $\delta_{\mathrm{NS}}$, is divided into two parts

$$\delta_{\mathrm{NS}} = \frac{\alpha}{\pi}\left[C_{\mathrm{NS}}^{\mathrm{quenched}} + (q-1)C_{\mathrm{Born}}^{\mathrm{free}}\right]. \tag{2.26}$$

See Refs. [12, 17] for a more detailed explanation.

The inner radiative correction $\Delta_R^V$ is the transition-independent correction which has a value of $(2.361 \pm 0.038)$ % [12, 18]. For more explanations and details about the correction the reader is referred to Ref. [12] and references therein.

### Experimental quantities

The $ft$ value is entirely composed of experimental quantities. The phase-space integral $f$ (also called as Fermi integral) needs the decay $Q$-value and is defined as

$$f = f(Z, W) = \int_1^{E_0} W\sqrt{W^2 - 1}(W_0 - W)^2 F(Z, W) S(Z, W) dW, \tag{2.27}$$

where $W$ is the total energy of the positron in electron rest mass units, $W_0$ is the maximum positron energy (the end-point energy), $Z$ is the charge number of the daughter state, $F(Z, W)$ the Fermi function and $S(Z, W)$ the shape-correction function. The effect of the shape-correction function is about 0.2 % for $A = 10$ and 5.7 % for $A = 74$ and it takes into account the screening of the atomic electrons and that the lepton wave functions exhibit some $r^2$ dependence over the nuclear volume. Also the electron wave functions must be an exact functions of nuclear charge-density distribution [1]. Further details regarding the shape-correction function can be found from Ref. [19]. A precise evaluation of the Fermi integral is not at all trivial due to the many corrections needed. The decay $Q$ values (or the end-point energies) are on the order of MeVs, increasing as a function of $Z^{1/3}$ due to Coulomb energy differences added with the proton-neutron mass difference.

The other quantity $t$ is the partial half-life of the emitter. In order to determine $t$, the half-life ($t_{1/2}$) and the superallowed branching ratio $R$ need to be experimentally measured to high precision. The partial half-life $t$ can be written as

$$t = \frac{t_{1/2}}{R}\left(1 + P_{\mathrm{EC}}\right), \tag{2.28}$$

where $P_{\mathrm{EC}}$ is the electron-capture branching ratio which also needs to be taken into account since the decay mode competes with $\beta^+$ decay. The electron-capture branching ratios are calculated and exhibit a correction typically on the order of 0.1 % [20]. The half-lives range from several seconds down to a few tens of milliseconds. The branching ratios of $T_z = 0$ emitters are in all cases very close to 100 %. In heavier cases (for example in $^{62}$Ga and $^{74}$Rb) there are several very weak Gamow-Teller transitions to $1^+$ states. Even in these cases the overall branching to the analogue state is more than 99 %. The branching ratios of the $T_z = -1$ emitters vary between 1.5–99.3 %.

The most precise $ft$ values have a precision of about $5 \times 10^{-4}$. To reach this precision, the $Q$ value has to be measured to a precision of $5 \times 10^{-5}$ or better since $\Delta f \propto Q^5$ and the half-life and branching ratio to a precision of about $1 \times 10^{-4}$.

### 2.2.3 $V_{ud}$ of the Cabibbo-Kobayashi-Maskawa quark-mixing matrix

The vector coupling constant $G_V$ in Eq. (2.20) can be linked to the $V_{ud}$ matrix element of the Cabibbo-Kobayashi-Maskawa (CKM) quark-mixing matrix element using the Fermi constant $G_F$ derived from the muon lifetime,

$$G_V = G_F V_{ud}, \tag{2.29}$$

where $G_F = 1.16637(1) \times 10^{-5}$ GeV$^{-2}$ [21]. The CKM matrix transforms the quark-mass eigenstates $|x\rangle$ to weak eigenstates $|x'\rangle$ according to

$$\begin{bmatrix} V_{ud} & V_{us} & V_{ub} \\ V_{cd} & V_{cs} & V_{cb} \\ V_{td} & V_{ts} & V_{tb} \end{bmatrix} \begin{bmatrix} |d\rangle \\ |s\rangle \\ |b\rangle \end{bmatrix} = \begin{bmatrix} |d'\rangle \\ |s'\rangle \\ |b'\rangle \end{bmatrix}. \tag{2.30}$$

The CKM matrix should be unitary. All of the matrix elements are experimentally determined. The most precisely determined element is $V_{ud}$ obtained from superallowed $\beta$ decays [1, 12]. Using Eq. (2.20) the $V_{ud}$ of the CKM matrix derived from superallowed $\beta$ decays is

$$V_{ud} = \frac{K}{2G_F^2 \left(1 + \Delta_R^V\right) \overline{\mathcal{F}t}}, \tag{2.31}$$

where $\overline{\mathcal{F}t}$ is the world-average $\mathcal{F}t$ value and $G_F$ is the weak-interaction constant for the purely leptonic muon decay [21]. The value of $V_{ud}$ in the review by Hardy and Towner in 2005 [1] (before the JYFLTRAP $Q_{EC}$ value measurements) is

$$V_{ud} = 0.9738(4) \text{ (superallowed decays 2005 [1])}. \tag{2.32}$$

As the elements of the CKM matrix are experimentally determined, it is possible to test the unitarity of the matrix. The most stringent test is the sum-squared of the top row which should equal to one

$$|V_{ud}|^2 + |V_{us}|^2 + |V_{ub}|^2 = 1. \tag{2.33}$$

Taking $V_{us} = 0.2200(26)$ and $V_{ub} = 0.00367(47)$ from the 2004 Particle Data Group (PDG) review [22] that were compiled prior to this thesis work, Eq. (2.33) becomes

$$|V_{ud}|^2 + |V_{us}|^2 + |V_{ub}|^2 = 0.9966(14), \tag{2.34}$$

which is off from the Standard Model expectations by $2.4\sigma$. The motivation of this thesis work was to improve the value of $V_{ud}$ and thus test the Standard Model.

In general, the unitarity requirement of the CKM matrix imposes

$$\begin{aligned} \sum_i V_{ij} V_{ik}^* &= \delta_{jk} \\ \sum_j V_{ij} V_{kj}^* &= \delta_{ik}. \end{aligned} \tag{2.35}$$

One such requirement is

$$V_{ud} V_{ub}^* + V_{cd} V_{cb}^* + V_{td} V_{tb}^* = 0 \tag{2.36}$$

which is tested in the field of high-energy physics. Another requirement is the sum-squared of the first column of the CKM matrix

$$|V_{\mathrm{ud}}|^2 + |V_{\mathrm{cd}}|^2 + |V_{\mathrm{td}}|^2 = 1. \tag{2.37}$$

Different unitarity tests are well described for instance in [23].

### 2.2.4 Other ways to determine $V_{ud}$

Although the superallowed $\beta$ decays are the most precise way to determine $V_{\mathrm{ud}}$ of the CKM matrix, this is by no means the only method. The easiest method from a nuclear structure point of view is the decay of a neutron to a proton. Although the nuclear structure dependent correction is not needed, the precision of the $V_{\mathrm{ud}}$ obtained from neutron decay is inferior to superallowed decays. From the most recent compilation of the Particle Data Group 2008 (PDG 2008) [24] the $V_{\mathrm{ud}}$ derived from neutron $\beta$ decay

$$V_{\mathrm{ud}} = 0.9746(19) \text{ (neutron decay)}. \tag{2.38}$$

Similarly, $V_{\mathrm{ud}}$ can be obtained from pion decay [25]

$$\pi^+ \rightarrow \pi^0 + e^+ + \nu_e. \tag{2.39}$$

This pion $\beta$ decay is very rare and has a branching ratio on the order of $10^{-8}$. However, it is a pure vector transition between two spin-zero members of an isospin triplet and is therefore analogous to superallowed Fermi transitions in nuclear beta decay. The resulting $V_{\mathrm{ud}}$ from pion decay [25]

$$V_{\mathrm{ud}} = 0.9728(30) \text{ (pion decay)}, \tag{2.40}$$

which is consistent with the value obtained from both neutron decay and superallowed $\beta$ decays.

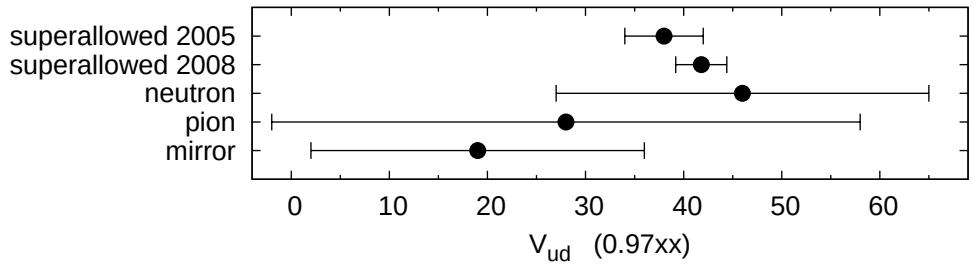


**Figure 2.1:** Comparison of different $V_{\rm ud}$ values. Clearly the most precise value comes from superallowed $\beta$ decays. The value from mirror decays can be improved by adding more nuclei measured with equal or better precision to the set, which presently consists of only three nuclei (see text).

Just recently it has been demonstrated that $V_{\rm ud}$ can be determined from nuclear mirror decays [26]. Since these decays are mixed Fermi and Gamow-Teller transitions, the mixing ratio of these different decay modes needs to experimentally determined. The $\mathcal{F}t$ value for mixed transitions is [26]

$$\mathcal{F}t = \frac{K}{G_F^2 V_{\rm ud}^2} \frac{1}{C_V^2 |M_F^0|^2 (1+\Delta_R^V)(1+f_A\rho^2/f_V)}, \tag{2.41}$$

where $K$, $C_V$ and $G_F$ are constants, $\Delta_R^V$ is the transition independent radiative correction [18], $f_A$ the statistical rate function for the axial-vector part of the interaction, $f_V$ the uncorrected statistical rate function and $\rho$ the Gamow-Teller to Fermi mixing ratio defined in Ref. [27]. Using the $\mathcal{F}t$ values for mirror decays from the recent compilation [27], it is possible to extract $V_{\rm ud}$. What is required is the $\beta$-neutrino angular correlation coefficient and the $\beta$-decay asymmetry parameter. For the current study in Ref. [26], three mirror transitions of $^{19}$Ne, $^{21}$Na and $^{35}$Ar were used yielding

$$V_{\rm ud} = 0.9719(17) \text{ (nuclear mirror transitions)}. \tag{2.42}$$

The value from mirror decays slightly deviates from the value obtained from superallowed $\beta$ decays. For comparison, the different values of $V_{\rm ud}$ are plotted in Fig. 2.1. The $V_{\rm ud}$ value from mirror decays at the moment consists of only three transitions. As more nuclei are measured the value will become more precise. It should be noted that the experimental quantities are much more difficult to measure to high precision; especially the $\beta$-neutrino correlations which are not needed for superallowed $\beta$ decays but needed for mirror decays. The $\beta$-neutrino correlations can be measured for instance with WITCH trap at CERN [28].

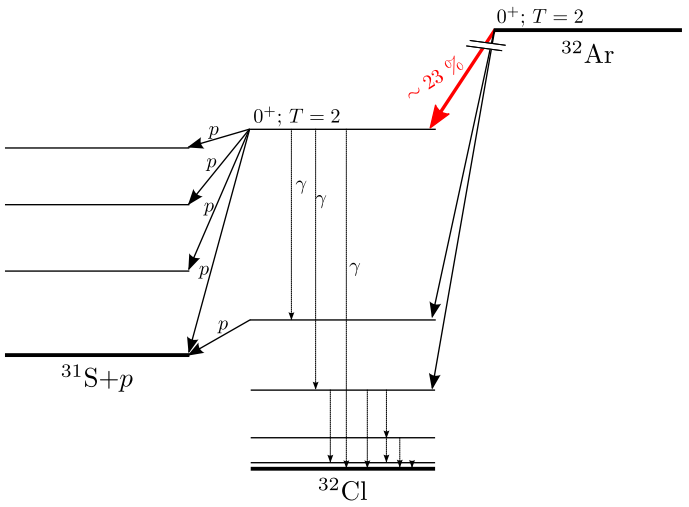


**Figure 2.2:** Decay scheme of $^{32}$Ar. The superallowed decay having about 23 % branching ratio is marked with a thick red arrow. The $T = 2$ isobaric analog state in $^{32}$Cl decays mainly by emitting protons.

### Superallowed decay of $T_z = -2$ nuclei

In principle, the $V_{\mathrm{ud}}$ value can also be determined from $T = 2$ superallowed $\beta$ decay. One such case already exists, $^{32}$Ar. However, instead of determining the $\mathcal{F}t$ value, the isospin-breaking correction was determined. In order to do so, the half-life, branching ratio and the decay $Q_{\mathrm{EC}}$ value was needed. The branching ratio determination [29] was difficult since the daughter $0^+$ state also decayed by emitting protons. The mass of $^{32}$Ar was measured with ISOLTRAP [30] and the mass of the $0^+$ state in the daughter $^{32}$Cl was determined from the $\beta$-delayed proton spectrum using the well-known masses of $^{31}$S and the proton [29]. The decay scheme of $^{32}$Ar is shown in Fig. 2.2. It is difficult to access $T = 2$ nuclei since they are located far from the valley of $\beta$ stability: the emitters have four more protons than neutrons. Nevertheless, it is possible to determine $V_{\mathrm{ud}}$ from these decays however accurate theoretical isospin-breaking corrections are needed.

# 3 Principle of a Penning trap

A Penning trap is an electromagnetic trap for electrically charged particles [31, 32]. Once the particles are inside the trap, they cannot escape without applied external forces. The trapping is achieved with superposition of a magnetic and electric fields. To simplify the motion of the particles in the trap, a homogenous magnetic and quadrupolar electric fields are used. It is convenient to assign $z$-axis as the magnetic field axis (so-called axial direction). The electric field is aligned such that strongest confinement with the field is along the $z$-axis. The confinement perpendicular to the $z$-axis (radial plane) is achieved with the magnetic field.

To form a quadrupole electric field, hyperbolical or cylindrical electrodes are commonly used. In cylindrical coordinates ($z$,$\rho$) the potential is of the form

$$V(z,\rho) = \frac{U_0}{4d^2}\left(2z^2 - \rho^2\right), \tag{3.1}$$

where $U_0$ is the potential difference between the ring and the endcap electrodes, $d = \sqrt{2z_0^2 + r_0^2}$ is the characteristic trap parameter defined by the trap geometry: $2z_0$ is the distance between the endcap electrodes and $r_0$ is the inner radius of the ring electrode. See Fig. 3.1 for examples.

With hyperbolical electrodes it is easier to form a quadrupolar electric field as the shape of the field is determined by the electrode geometry. Nevertheless, correction electrodes are needed to compensate for field imperfections for both electrode configurations. In a hyperbolical geometry, the electrodes need to be truncated and holes for ion injection and extraction provided, which will create electric field imperfections. In a cylindrical geometry, typically one or two correction electrodes are used to form a proper electric potential, see Fig. 3.1(b).

The Penning traps in JYFLTRAP are of a cylindrical configuration, with two correction electrodes on both sides of the ring electrode. Voltages of 10. . . 100 V across the ring and endcaps have been used with a magnetic field of 7 T. A similar electrode configuration is in use at MLLTRAP in Munich [33] and with somewhat modified geometry at SHIPTRAP, GSI [34].

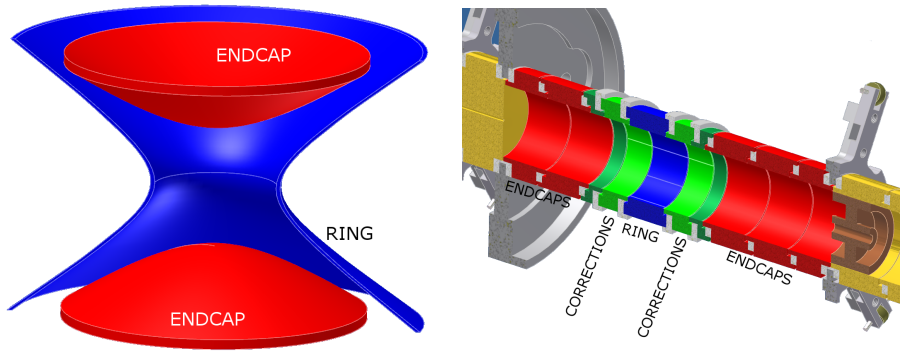


(a) (b)

**Figure 3.1:** Hyperbolical (a) and cylindrical (b) Penning traps. The ring electrode is colored with blue and endcap electrodes with red. Electric field imperfections can be compensated by using additional correction electrodes (green).

## 3.1 Ion motion in a Penning trap

The motion of an ion in a magnetic field $\vec{B}$ and in an electric field $\vec{E}$ is described by the Lorentz force

$$\vec{F} = m\ddot{\vec{r}} = q(\dot{\vec{r}} \times \vec{B} + \vec{E}), \tag{3.2}$$

where $\vec{E} = \vec{\nabla} V$. Since the electric field is of the form of a quadrupole, the field can be written

$$\vec{E} = \frac{U_0}{2d^2} \begin{bmatrix} x \\ y \\ -2z \end{bmatrix}. \tag{3.3}$$

The equation of motion (3.2) thus becomes

$$\begin{bmatrix} \ddot{x} \\ \ddot{y} \\ \ddot{z} \end{bmatrix} - \frac{q}{m} B \begin{bmatrix} \dot{y} \\ -\dot{x} \\ 0 \end{bmatrix} - \frac{q}{m} \frac{U_0}{2d^2} \begin{bmatrix} x \\ y \\ -2z \end{bmatrix} = 0. \tag{3.4}$$

The solution in the axial ($z$) direction is a simple harmonic oscillator with amplitude $A_z$ and angular frequency

$$\omega_z = \sqrt{\frac{qU_0}{md^2}}. \tag{3.5}$$

Using the coordinate transformation $u = x + iy$, the solution in the radial plane is

$$u = Ae^{-i\omega_+ t} + Be^{-i\omega_- t} \tag{3.6}$$

with frequencies

$$\omega_\pm = \frac{1}{2}\left(\omega_c \pm \sqrt{\omega_c^2 - 2\omega_z^2}\right). \tag{3.7}$$

The two frequencies $\omega_+$ and $\omega_-$ are called the reduced cyclotron frequency and the magnetron frequency, respectively. In an ideal trap the sum of the two frequencies

$$\omega_+ + \omega_- = \omega_c = \frac{q}{m}B, \tag{3.8}$$

is the cyclotron frequency of a particle with mass $m$ and charge $q$ in an electric field free magnetic field. The position of an ion in a Penning trap at a given time $t$ is

$$x(t) = A_+ \cos(\omega_+ t + \phi_+) + A_- \cos(\omega_- t + \phi_-) \tag{3.9}$$

$$x(t) = A_+ \sin(\omega_+ t + \phi_+) + A_- \sin(\omega_- t + \phi_-) \tag{3.10}$$

$$y(t) = A_z \cos(\omega_z t + \phi_z). \tag{3.11}$$

The ion motion in a Penning trap has been illustrated in Fig. 3.2. It is worth noting that the magnetron motion is almost mass independent and in first order polynomial approximation can be written as

$$\omega_- \approx \frac{U_0}{2Bd^2}. \tag{3.12}$$

The relative magnitudes of the Penning trap frequencies are

$$\omega_c > \omega_+ \gg \omega_z \gg \omega_-. \tag{3.13}$$

The eigenfrequencies of the ion motion are linked to the cyclotron frequency $\nu_c = \frac{1}{2\pi}\omega_c = \frac{1}{2\pi}\frac{q}{m}B$ via the so-called invariance theorem [31, 35]

$$\nu_-^2 + \nu_+^2 + \nu_z^2 = \nu_c^2, \tag{3.14}$$

which is highly immune to misalignments of the electric and magnetic fields axis and to quadrupolar electric field imperfections.

### 3.1.1 Dipolar excitations

Any of the eigenmotions can be excited[1] by applying an additional dipole radiofrequency (r.f.) electric field of the corresponding frequency. For the axial motion, the

[1] Excitation in this sense means changing the motional amplitude of the ions

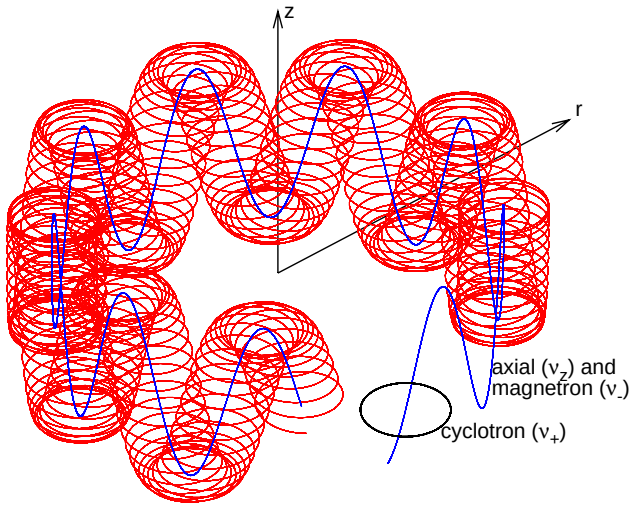


**Figure 3.2:** Ion motion in a Penning trap. The superposition of the three eigenmotions is illustrated. Frequencies of $\nu_- = 1.4$ kHz, $\nu_+ = 300$ kHz and $\nu_z = 13$ kHz and amplitudes of $\rho_- = 1.5$ mm, $\rho_+ = 0.3$ mm and $\rho_z = 10$ mm were used to create the plot.

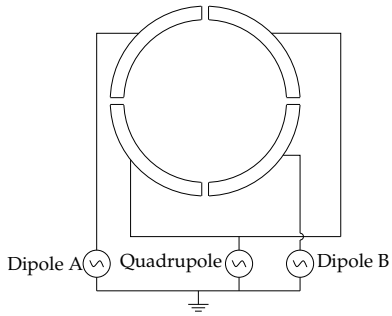


**Figure 3.3:** Four-fold splitted ring electrode. Two of the quadrants are used for quadrupole excitation (two-plate configuration) and the other two for dipole excitations: Dipole A for magnetron and Dipole B for reduced cyclotron motion excitations.

r.f. field has to be applied between the endcap electrodes, while for the radial motion a dipole field across the ring electrode is needed. For this purpose the ring electrode is split so that azimuthal r.f. field can be applied. Applying the r.f. electric field with corresponding eigenfrequency will linearly change the amplitude of the motion. It is also possible to reduce the motion amplitude with a dipole excitation.

Typically, an electric dipole excitation with the magnetron frequency is used to increase the radius of all ions in the trap since the magnetron frequency is almost mass independent. On the other hand, excitation with the reduced cyclotron frequency is used to mass selectively drive the motion of one ion species. One possible configuration to apply voltage to the ring electrode is shown in Fig. 3.3.

### 3.1.2 Quadrupolar excitation

The dipole excitations are used to excite the ion motion with r.f. electric fields having the frequency of one of the eigenfrequencies. Quadrupole excitations are used to excite the ion motion at sums or differences of the eigenfrequencies and can be used to convert one motion into the other. The most common form of quadrupole excitation used in this work is the conversion between the two radial motions with cyclotron frequency $\nu_c$. Usually, ions are first prepared so that they have only magnetron ($-$) motion. The quadrupole excitation is switched on and the magnetron motion is mass-selectively converted to cyclotron motion.

The conversion is periodic and the excitation time ($T_{\mathrm{RF}}$), frequency ($\nu_{\mathrm{RF}}$) and amplitude ($V_{\mathrm{RF}}$) determine the number of conversions performed. Usually the excitation

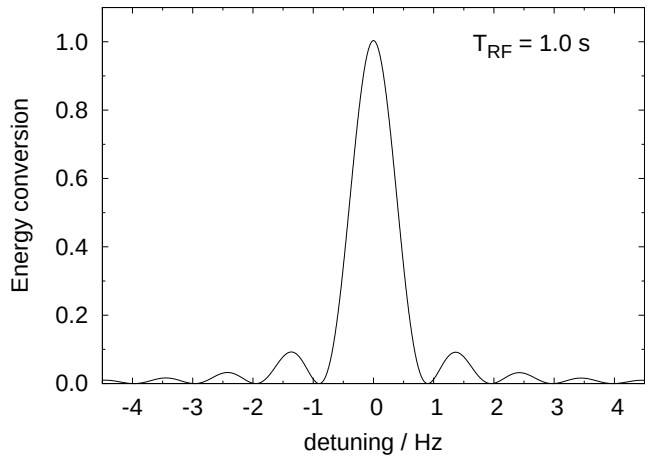


**Figure 3.4:** Energy conversion as a function of detuning frequency when one full conversion occurs at $\nu_{\mathrm{RF}} = \nu_c$. An excitation time of 1 second was used.

time and amplitude is chosen such that one full conversion occurs at the resonance frequency $\nu_c$. The needed amplitude is given by

$$V_{\mathrm{RF}} = 2a^2 B \frac{\pi}{T_{\mathrm{RF}}}, \tag{3.15}$$

where $a$ is the inner diameter of the ring electrode. Conversion close to $\nu_{\mathrm{RF}} = \nu_c$ is illustrated in Fig. 3.4.

Figure 3.4 shows the energy conversion in an ideal trap. The ions are prepared such that prior to the excitation they have solely one motion at the beginning of the conversion and there is no dissipative forces such as damping due to ion-atom collisions in residual gas.

The eigenmotion amplitudes as a function of excitation time are solved in Ref. [36]. Assuming a dissipative force

$$\vec{F}_{\mathrm{damp}} = -\delta m \vec{v}, \tag{3.16}$$

where $\delta$ is a damping coefficient, $m$ mass of the ion and $\vec{v}$ the velocity of the ion. The amplitudes of the radial eigenmotions in the presence of a radiofrequency quadrupole

electric field are

$$\begin{aligned}\rho^{\pm}(t) =& e^{-\frac{\delta}{2}t}\Bigg\{\rho^{\pm}\cosh\left(\omega_B e^{i\theta}t\right) \mp \frac{1}{2}\frac{\rho^{\pm}(0)\left[\gamma\omega_c + i\left(\omega_{RF}-\omega_c\right)\right] + \rho^{\mp}(0)k_0^{\pm}}{\omega_B e^{i\theta}} \\ & \times \sinh\left(\omega_B e^{i\theta}t\right)\Bigg\} e^{i\frac{1}{2}(\omega_{RF}-\omega_c)t},\end{aligned} \tag{3.17}$$

where $\rho^{\pm}(0)$ are the amplitudes of the motions at $t = 0$, $\omega_{RF}$ the excitation frequency and $\omega_c$ the cyclotron frequency of the ion. The frequency $\omega_B$, the phase $\theta$ and the coupling constants $k_0^{\pm}$ are

$$\begin{aligned}\omega_B &= \sqrt{\omega_{B+}\omega_{B-}} \\ \theta &= \tfrac{1}{2}\left(\theta_+ + \theta_-\right) \\ k_0^{\pm} &= k_0 e^{\pm i\Delta\phi},\end{aligned} \tag{3.18}$$

where

$$\begin{aligned}\omega_{B\pm} &= \tfrac{1}{2}\sqrt{\left(\omega_{RF}-\omega_c\right)^2 + \left(\gamma\omega_c \mp k_0\right)^2} \\ \theta_{\pm} &= \arctan\tfrac{\omega_{RF}-\omega_c}{\gamma\omega_c \mp k_0} \\ \Delta\phi &= \varphi_{RF} - \left(\varphi_+ + \varphi_-\right).\end{aligned} \tag{3.19}$$

The constant $k_0$ is a coupling constant and is proportional to the amplitude of the driving quadrupole field and $\Delta\phi$ is the phase difference between the driving r.f. field and the ion motion. The damping coefficient

$$\gamma = \frac{\delta}{\omega_+ - \omega_-} \approx \frac{\delta}{\omega_c}, \tag{3.20}$$

since $\omega_+ \gg \omega_-$. Values of $k_0$ and $\gamma$ can be determined experimentally.

## 3.2 Resonance frequency determination

As described in the previous section, under the quadrupole driving field the maximal conversion between the two radial motion occurs when the exciting field has a frequency $\nu_c$. For ions having $q = 1e$ and $A = 100$, the cyclotron frequency in a 7 T magnetic field is on the order of 1 MHz. On the other hand, the magnetron frequency is much lower, $\approx$ 1 kHz. Since the radial kinetic energy is $\propto \nu^2$, the energy of an ion in purely cyclotron motion is $\approx 10^6$ the energy of an ion in purely magnetron motion.

The resonance is detected using the time-of-flight ion-cyclotron resonance (TOF-ICR) technique [37]. After the quadrupole excitation the ions are released from the trap and are allowed to drift to a detector that can register the time-of-flight of the ions. The ions feel a force due to the gradient of the magnetic field. There, the radial energy of the ions gets converted to axial energy, which increases the velocity of the ions. Since the energy difference between the two radial motions is $\approx 10^6$, the ions that arrive at the detector considerably earlier have more cyclotron motion.

The time-of-flight of the ions can be calculated by integrating over the electric and magnetic fields from the trap to the detector position

$$T(\omega_{\mathrm{RF}}) = \sqrt{\frac{m}{2}} \int_{z_0}^{z_1} \sqrt{\frac{1}{E_0 - q \cdot V(z) - \mu\,(\omega_{\mathrm{RF}}) \cdot B(z)}}, \tag{3.21}$$

where $V(z)$ and $B(z)$ are the electric and magnetic fields along the ion path (which is also the magnetic field axis) from the trap ($z_0$) to the detector ($z_1$) and $E_0$ is the *total* kinetic energy of the ions. The magnetic moment

$$\mu(\omega_{\mathrm{RF}}) = \frac{E_r(\omega_{\mathrm{RF}})}{B}, \tag{3.22}$$

where $E_r(\omega_{\mathrm{RF}})$ is the total radial kinetic energy of the ions. Since the energy of the magnetron motion is so small compared to the energy of the cyclotron motion, the radial energy can be approximated

$$E_r(\omega_{\mathrm{RF}}) \approx E_+(\omega_{\mathrm{RF}}) = \frac{1}{2} m \big(\rho_+(\omega_{\mathrm{RF}})\big)^2 \omega_+^2, \tag{3.23}$$

where $\rho_+(\omega_{\mathrm{RF}})$ is obtained from Eq. (3.17). Furthermore, for time-of-flight calculations, it can be approximated that $\omega_+ \approx \omega_c$. An example of a time-of-flight resonance is shown in Fig. 3.5. Fitting of the resonance curve thus require eight (8) parameters:

1. Resonance frequency, $\nu_c$
2. Damping coefficient, $\delta$
3. Initial axial energy, $E_{\mathrm{axial}} = E_0 - E_r$
4. Initial magnetron radius, $\rho_-(t = 0)$
5. Initial cyclotron radius, $\rho_+(t = 0)$

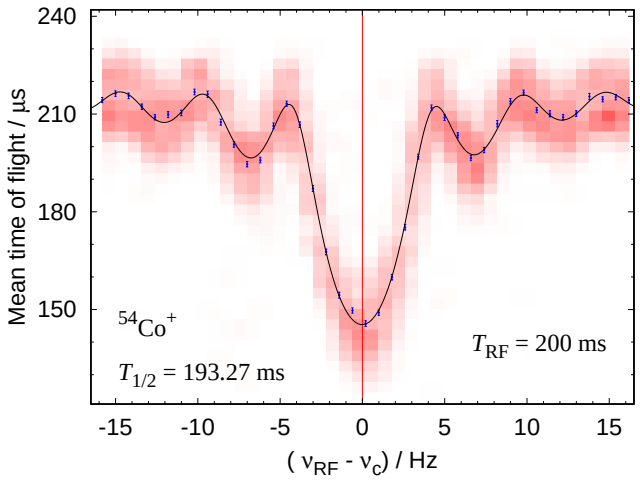


**Figure 3.5:** Time-of-flight ion-cyclotron (TOF-ICR) resonance of $^{54}$Co. An excitation time ($T_{\mathrm{RF}}$) of 200 ms and amplitude ($A_{\mathrm{RF}}$) of 56 mV was used. The mean time-of-flight of the ions is plotted as a function of detuning frequency from the cyclotron resonance frequency, $\nu_c$. The different shades of red indicate the number of detected ions: the darker the color, the more ions were detected.

6. Phase between the driving field and the initial cyclotron motion, $\phi$
7. Excitation time, $T_{\mathrm{RF}}$
8. Excitation amplitude $A_{\mathrm{RF}}$

Usually the ions are prepared such that there is no initial cyclotron motion ($\rho_+(t = 0) \approx 0$), which also implies that the phase difference, $\Delta\phi$, has no effect. This is also the case shown in Fig. 3.5.

## 3.3 Excitation with time-separated oscillatory fields

Excitations with time-separated oscillatory fields (the so-called Ramsey method) has been recently introduced to on-line Penning trap facilities [38,39]. The method itself is old, and was invented by N. F. Ramsey [40] in 1949 when improving the molecular-beam magnetic-resonance method developed by I. I. Rabi [41–45]. The first Ramsey resonances were obtained at ISOLTRAP in 1992 [46] however since

the fitting function was not available at that time the technique was only used for testing. The first mass measurement employing the Ramsey excitation scheme was the $^{38}$Ca experiment at ISOLTRAP [47].

In the Ramsey method the excitation is split to in two or more parts by interrupting the exciting wave while preserving phase coherence over the break. The most often used Ramsey excitation scheme is the so-called two-fringe excitation where the exciting wave is switched on for a given time $\frac{1}{2}T_{\mathrm{RF}}$, then switched off for a time period $T_{\mathrm{wait}}$ and then on again for another period of $\frac{1}{2}T_{\mathrm{RF}}$. The excitation amplitude needs to be scaled with a factor $(T_{\mathrm{RF}} + T_{\mathrm{wait}})/T_{\mathrm{RF}}$ in order to obtain a full conversion at the resonance frequency.

For the Ramsey excitation to fully work, the exciting sinusoidal wave has to be phase coherent over the whole excitation pattern. The effect of the Ramsey excitation compared with the conventional method is that the sideband structure is enhanced. The longer the waiting period $T_{\mathrm{wait}}$, the more enhanced the sideband structure will be. In addition, the width of the main peak gets narrower and in the case of very long waiting time between the $T_{\mathrm{RF}}$-on periods, the enhancement is as high as 40 %. A comparison between the conventional and Ramsey excitation method is shown in Fig. 3.6.

At the time of writing this thesis the fitting function exists only for an ideal resonance. That is, no damping effect due to the presence of residual gas in the trap is incorporated to the fitting function. However, the theoretical description of the Ramsey excitation with damping will soon be available [48]. Also, it has to be assumed that the ion motion in the trap prior to the excitation is purely magnetron. One such resonance is shown in Fig. 3.7, which was obtained under similar conditions than the resonance shown in Fig. 3.5, except splitting the excitation into two parts of 50 ms of duration and a waiting time of 100 ms.

Due to the missing damping, the initial cyclotron and phase terms, the fitting function is slightly simpler. The energy conversion ($F_2$) is given by [39]

$$F_2(\delta, \tau_0, \tau_1, g) = \frac{4g^2}{\omega_R^2} \cdot \sin^2 \frac{\omega_R \tau_1}{2} \cdot \left[ 2 \cos \frac{\delta \tau_0}{2} \cdot \cos \frac{\omega_R \tau_1}{2} - 2 \frac{\delta}{\omega_R} \sin \frac{\delta \tau_0}{2} \cdot \sin \frac{\omega_R \tau_1}{2} \right]^2, \tag{3.24}$$

where $\delta = \omega_{\mathrm{RF}} - \omega_c$ is the frequency detuning, $\omega_R = \sqrt{(2g)^2 + \delta^2}$ the Rabi frequency, $\tau_0$ the waiting period between the excitation fringes and $\tau_1$ the duration of one excitation fringe. The coupling constant $g$ can be renormalized such that it resembles the excitation amplitude. Thus to fit a two-fringe Ramsey time-of-flight ion-cyclotron resonance curve, 6 parameters are needed:

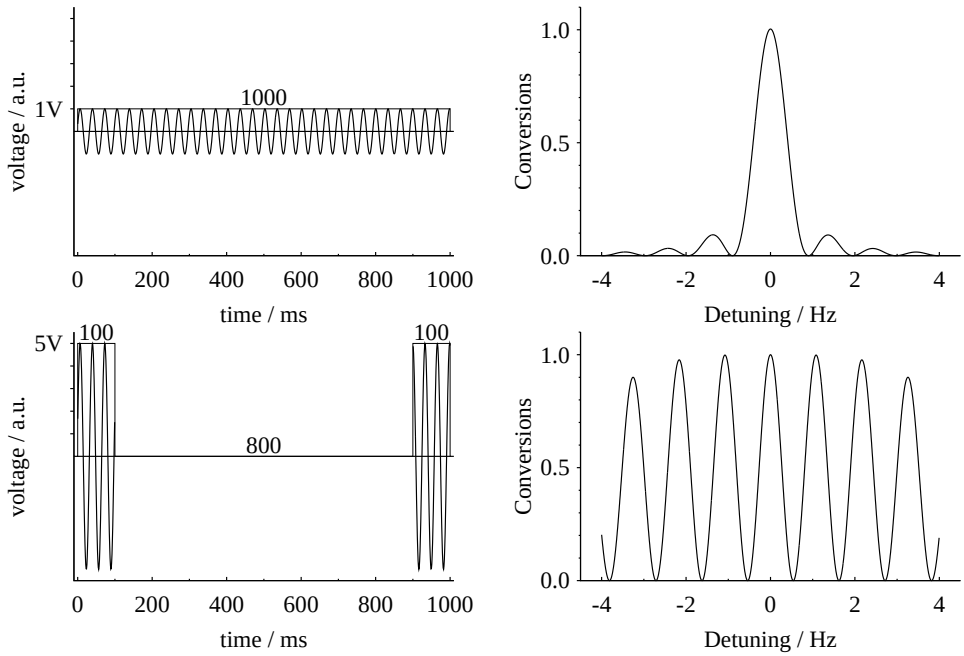


**Figure 3.6:** A comparison of an excitation with the conventional and time-separated timing patterns. The excitation pattern and relative amplitudes are shown on the left (the frequency is not to scale). The response energy conversion is shown on the right. For Ramsey excitation, the amplitude has to be increased to account for the waiting time. The sideband structure is enhanced and the main peak width reduced.

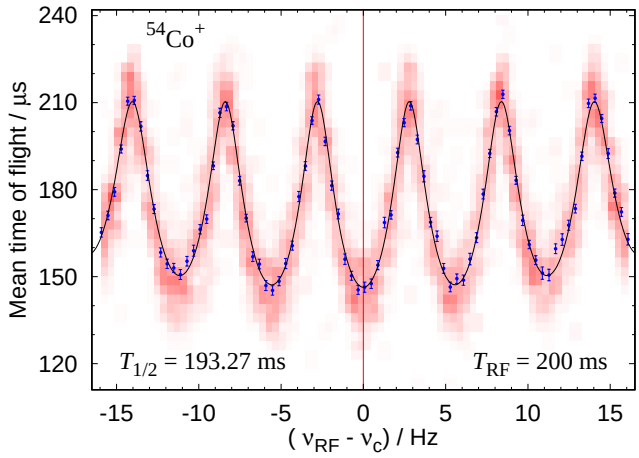


**Figure 3.7:** Time-of-flight ion-cyclotron resonance of singly-charged $^{54}$Co using an excitation with time-separated oscillatory fields. The excitation is split into two parts of 25 ms duration with 150 ms waiting time in between. An excitation amplitude $A_{\mathrm{RF}}$ of 224 mV was used.

1. Resonance frequency, $\nu_c$
2. Initial axial energy, $E_{\mathrm{axial}} = E_0 - E_r$
3. Initial magnetron radius, $\rho_-(t = 0)$
4. Excitation fringe time, $\tau_1$
5. Waiting time, $\tau_0$
6. Excitation amplitude $A_{\mathrm{RF}} \propto g$.

## 3.4 Octupolar excitation

Instead of a four-fold segmented ring electrode the octupole excitation employs an eight-fold segmented ring electrode to form an octupolar r.f. electric field. To convert motion from one radial motion to another, the driving r.f. field should have frequency close to $2\nu_c$. Although there has been huge efforts to understand the

octupole excitation, no analytical solution exists for the resonance lineshape. Octupolar excitation has been extensively studied at LEBIT at Michigan State University [49] and with SHIPTRAP at GSI Darmstadt [50]. It has been shown that about a factor of ten improvement in resolving power has been achieved in comparison to conventional quadrupole excitation with a similar excitation time. Even though the improvement factor looks very promising, the lineshape of the excitation is not yet fully understood and thus octupolar excitation has so far been only used in tests.

# 4 Experimental methods

## 4.1 Production and separation of radioactive nuclei

Short-lived ($T_{1/2} \gtrsim 1\mu$s) nuclei are studied in various laboratories around the world. Due to short half-lives, the produced nuclei have to be produced and immediately used for the experiments. Another important factor is the separation of the element of interest from contaminants. As the different production and separation techniques are complementary, the experiments that use the rare beams are similar from one facility to another. On-line Penning trap mass spectrometers are no exception to this and many facilities now have these devices.

In this section the most commonly used production and separation mechanism for short-lived nuclei are described and a short overview of the Penning trap setups are given.

### 4.1.1 ISOL technique

Two major ISOL facilities in the world are ISOLDE at CERN, Geneva, Switzerland [51] and ISAC at TRIUMF in Vancouver, Canada [52]. The radioactive ions are produced by hitting a thick stationary target (g/cm$^2$) with a high-energy ($E \gtrsim 500$ MeV) proton beam. The radioactive nuclei are produced in fission, fragmentation and spallation reactions [53]. The target is made such that the reaction products can diffuse out from the target matrix as efficiently as possible. Once the products are out from the target container, they effuse in a gas phase to an ion source for ionization. Four different types of ionization methods are available:

- surface ion sources
- plasma ion sources
- electron bombardment ion sources
- laser ion sources

The three aforementioned sources ionize several elements simultaneously while the laser ion source is element specific, but only if ions produced with other ionization methods (usually surface ions) can be suppressed. After ionization, the ions are accelerated typically to 30—60 keV and later mass separated with magnetic separators. Since some elements have very poor diffusion or effusion properties, not all elements are available. The refractory elements such as zirconium or molybdenum are the most difficult and presently are not available as ion beams at ISOL facilities. Also, the release times can be so long that too short-lived nuclei can not be extracted (typically if $T_{1/2} < 5$ ms). If the element is chemically "easy", the ISOL facilities can produce extremely exotic nuclei that are both far from the stability and also rather short-lived. For instance yields of rubidium isotopes at ISOLDE range from very neutron deficient $^{74}$Rb ($T_{1/2} = 65$ ms and has 11 less neutrons than the stable $^{85}$Rb) up to $^{102}$Rb ($T_{1/2} = 37$ ms and has 13 more neutrons than the stable $^{87}$Rb).

Both ISOLDE and ISAC have working Penning trap setups for mass measurements. The ISOLTRAP Penning trap [54] at ISOLDE, CERN is the pioneering Penning trap experiment for exotic nuclei and is still operational. Two Penning traps are used: one for beam purification and preparation and the other for high-precision mass spectroscopy. The Penning trap experiment TITAN [55] at ISAC, TRIUMF has just recently been commissioned and is used for mass measurements of exotic highly-charged ions. TITAN has also measured the shortest-lived isotope ever in a Penning trap ($^{11}$Li, $T_{1/2} = 8.8$ ms) [56].

### 4.1.2 In-flight fusion and fission technique

The production mechanism in in-flight production differs dramatically from the ISOL technique. Here, a medium-energy ($5 - 50A$ MeV) beam impinges on a thin target where reaction products are produced in fusion-evaporation or in fission reactions. The nuclei accessible with fusion-evaporation reactions are limited to neutron deficient but currently this is the only method to produce transuranium elements. After production, the reaction products continue to fly in the forward direction and are separated from the primary beam using velocity filters. The reaction products need to be slowed down from energies of a few MeV/u before they can be used for instance in trap experiments. This production mechanism is rather fast ($\sim \mu$s) and is chemically insensitive.

Two Penning trap facilities are in use which use this kind of production mechanism – SHIPTRAP [34] at GSI, Darmstadt, Germany and the Canadian Penning trap [57] at ANL, Argonne, USA. In 2008 the first-ever Penning trap mass measurement of

transuranic element was carried out successfully at SHIPTRAP.

### 4.1.3 In-flight projectile fragmentation technique

This production technique uses a high-energy ($> 50A$ MeV) heavy-ion beam impinging on a thin light-element (like beryllium) target. Instead of fusion the primary beam is fragmented. With this method radioactive ion beams that are lighter than the primary beam can be produced. The incident primary beam energies are about 100 MeV/u or more and since the target is light, the fragmented beam has a similar energy. The reaction products are separated in fragment separators. Good examples of currently working fragment separators are the FRS at GSI [58], the A1900 at NSCL [59] and just recently, the commissioned BigRIPS at RIKEN, Japan [60]. This production and separation mechanism is also fast ($\sim \mu$s), chemically insensitive and allows access to very exotic short-lived isotopes. The future facilities such as the superFRS of the FAIR project (or the already commissioned BigRIPS) will be able to produce very exotic nuclei close to or beyond the driplines, where either proton or neutron separation energy is negative.

Since the production fragments have very high velocity, they need to be decelerated to more manageable speeds before low-energy experiments such as traps can be used. This is usually achieved with gas stoppers, where the reaction products are thermalized prior to extraction as low energy beams. The only Penning trap facility using beams from projectile fragmentation is the LEBIT facility [61] at NSCL, East Lansing, USA.

### 4.1.4 IGISOL technique

The IGISOL method has been developed and is used at Jyväskylä, Finland [62]. The basic principle is to use light (like protons, $E = 5 - 100$ MeV) or medium-heavy (like calcium, $E \approx 5A$ MeV) beams impinging on thin target(s) and to stop the reaction products in a gas and extract ions out as a low-energy ion beam. Three different *ion guides* are used for different types of reaction [63]. The guide "guides" ions out from the gas cell to a differentially pumped sextupole RF ion guide [64]. After, the ions are accelerated to an energy of $30q$ keV and are mass separated with a dipole magnet which has a mass resolving power $R = M/\Delta M$ of about 300. A schematic layout of the IGISOL facility is shown in Fig. 4.1. The target chamber houses the ion guide and the sextupole ion guide (A). After acceleration, the mass separation is performed with a dipole magnet (B). At the focal plane of the magnet the beam can

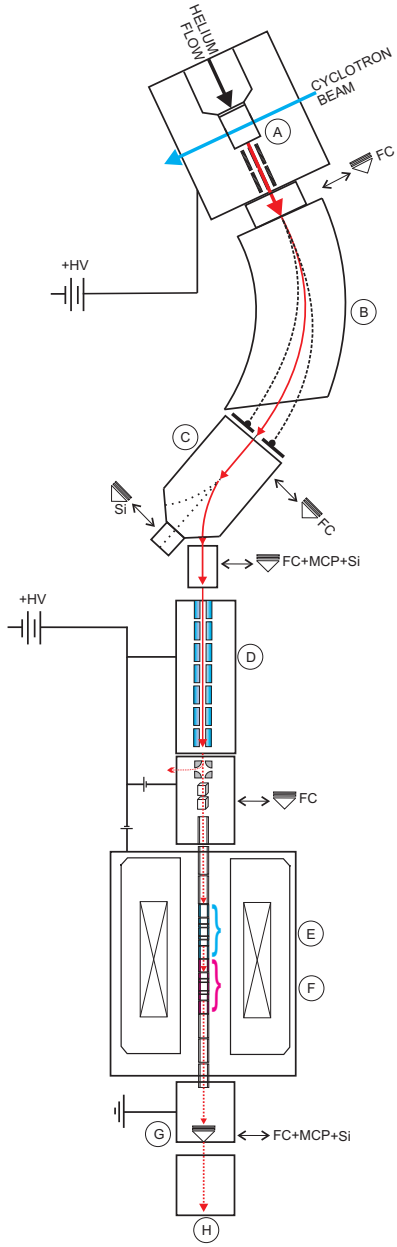


**Figure 4.1:** The layout of IGISOL. See text for explanation.

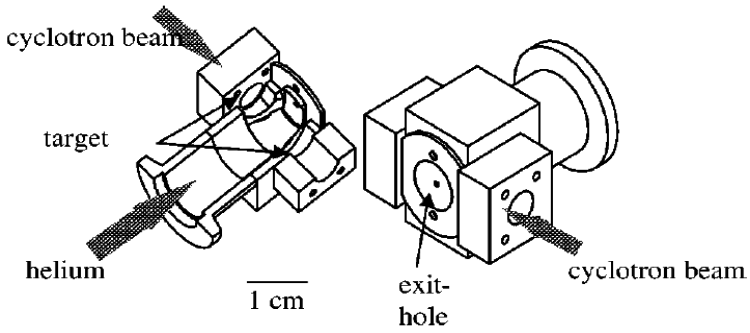


**Figure 4.2:** The light-ion fusion ion guide. Two separate targets can be used. To exchange the targets, the guide is rotated by 180°. This picture is from Ref. [65].

be steered to one of the three beam lines (C). The RFQ (D) and Penning traps (E,F) are further downstream on the trap beamline. The final detection and implantation point for ions are marked as (G) and (H). The RFQ and Penning traps are explained in section 4.2.

In this work the so-called light-ion fusion guide was used. A beam of protons or $^{3}$He was used to produce the ions of interest in fusion reactions. For instance, $^{54}$Co was produced with a 14 MeV proton beam in the $^{54}$Fe(p,n)$^{54}$Co reaction. A schematic drawing of the light-ion guide is shown in Fig. 4.2.

Other ion guides enable the use of different kind of reactions. The fission ion guide is designed for producing ions in proton-induced fission reactions. Also, fusion evaporation reactions can be used at IGISOL to produce neutron-deficient nuclei near the $N = Z$ line.

## 4.2 The JYFLTRAP setup

The JYFLTRAP system consists of three different traps which are the radio frequency quadrupole (RFQ) [66] and two Penning traps [67]. The first trap, the purification trap, is filled with helium gas ($p \approx 10^{-4}$ mbar) while the other is operated in vacuum. All three traps are needed to perform a mass measurement (or a $Q$-value measurement). Usually all of the traps are operated in parallel in order to achieve maximal efficiency. The JYFLTRAP setup is shown in Fig. 4.3.

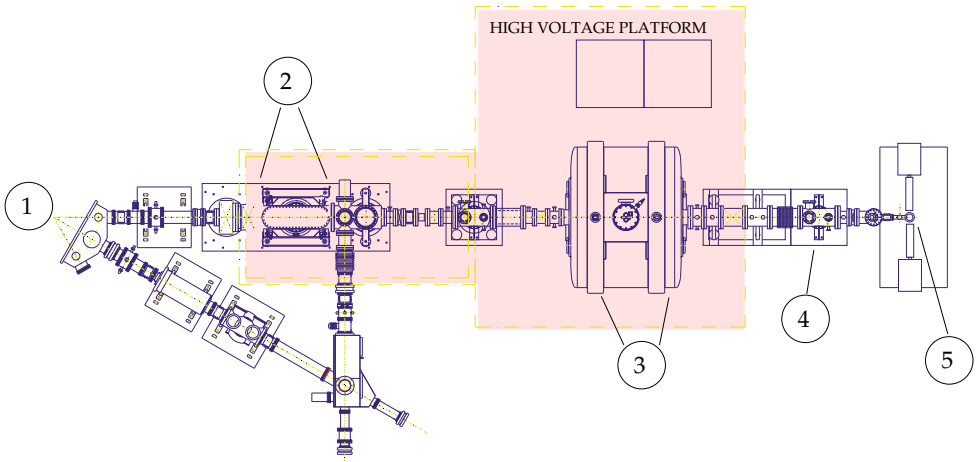


**Figure 4.3:** The JYFLTRAP setup. The focal point of the IGISOL separator has been marked (1). The location of the RFQ (2) and the Penning traps (3) has been marked. The beam diagnostics chamber (4) is used for ion time-of-flight detection and location (5) is reserved for post-trap spectroscopy. The area shaded with pink is the high-voltage platform.

### 4.2.1 The radiofrequency quadrupole cooler and buncher

The traps are operated in a bunched mode. The incident DC beam from IGISOL is electrostatically decelerated from 30 keV to $\approx$ 100 eV prior to injection to the RFQ structure. Three injection electrodes are used to focus the ion beam through a small aperture to the quadrupole structure that is filled with helium gas at a pressure of about $10^{-2}$ mbar. The remaining 100 eV is dissipated and the ions are cooled down with ion-atom collisions in the gas. The radiofrequency electric field keeps the ions confined in the trap. The quadrupole electrodes are segmented in the axial direction in order to apply a small voltage gradient. At the end of the structure, a switchable plate electrode is used to control the extraction of the ions. In accumulation mode, the voltage of the plate electrode is kept higher than the nearest quadrupole electrodes. The buffer gas cools the ions to the bottom of the potential well. This is illustrated in Fig. 4.4.

Once a sufficient amount of time has been spent collecting the ions, the extraction voltage is lowered and the bunch is released. A typical bunch width is $\approx 15\mu$s and the transverse emittance $3\pi$ mm mrad at 38 keV and energy spread about 1 eV [66]. The nominal transmission is 60 %, in both bunched and continuous mode for ions with

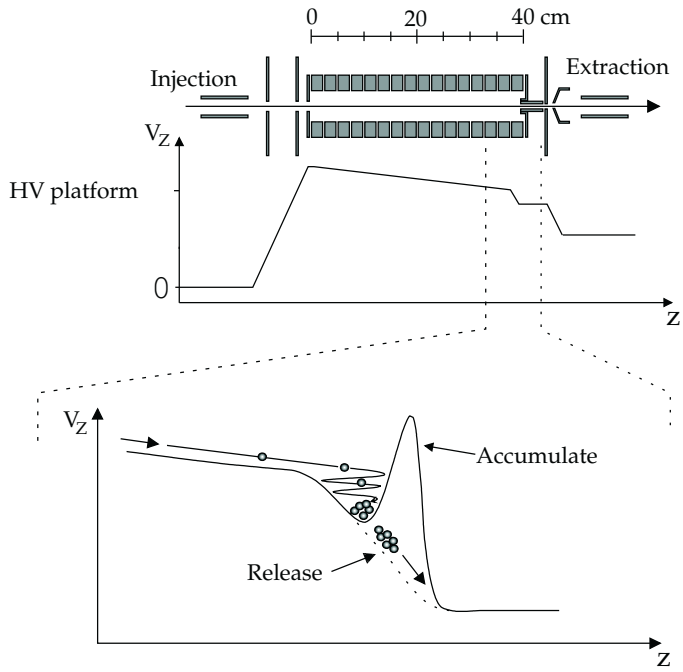


**Figure 4.4:** Schematic figure of the JYFL gas-filled radiofrequency cooler buncher. The injected high-energy ($\approx$ 30 keV) ion beam is electrostatically decelerated, cooled and accumulated in a potential well. The cooled ion cloud is released as a bunch.

$A > 40$. This, however, is intensity dependent. In continuous mode, the transmission drops below 50 % level if input current of 5 nA is exceeded. In bunched mode the width of the bunch has a $\sqrt[3]{N}$ dependence [68]. A kicker electrode is installed close to the focal point of the IGISOL separator (see Fig. 4.3), which can be used to control the amount of ions entering the RFQ.

Bunched beams are used, in addition to the Penning traps, for collinear laser spectroscopy studies [69]. The absolute constant background caused by laser scattered photons can be reduced significantly by bunching the ions in cycles of a few hundred milliseconds and then measuring for only about 25 $\mu$s in duration which is the width of the ion bunch. Thus, bunched beams suppress the background by a factor of about $10^4$.

### 4.2.2 Purification trap — sideband cooling technique

The purification trap [67] uses bunches of ions that are prepared with the RFQ. The ions are injected into the purification trap by lowering the RFQ side potential wall so that the ion bunch can enter as illustrated in Fig. 4.5. When the bunch is inside, the potential wall is restored within $\approx 2$ $\mu$s which is fast enough so that the ions will remain inside the potential well and not reflect back out of the trap. Since the purification trap is filled with low-pressure ($\approx 10^{-4}$ mbar) helium gas, the ions lose kinetic energy through ion-atom collisions and thus the ion cloud will eventually cool down to the bottom of the potential well. The cyclotron motion ($\nu_+$) will also cool down but the magnetron motion ($\nu_-$) amplitude will increase under the dissipative cooling force. The small barrier in the injection potential enables a new bunch to be captured without losing the one which is already in the trap (see Fig. 4.5).

The purification trap voltages are given in table 4.1. The values given in the column "trapped" show those when the trap is closed. The electrode geometry has been scaled from the ISOLTRAP purification trap [70]. Also the relative voltages have been given in the same reference. The injection side endcaps 1 and 2 are kept at a slightly lower voltage than the optimum 100 V to avoid possible kicking of ions over the extraction side wall when closing the injection wall.

#### Dipole magnetron excitation

Once the ions have been cooled down, an electric dipole excitation at the magnetron frequency ($\nu_-$) is switched on. The duration and amplitude is chosen such that the

**Table 4.1:** The voltages used in the purification trap. All voltages are given in Volts (V) and are relative to the ring electrode potential of the purification trap. For explanation, see text.

| Electrode | trapped | injection | extraction |
|---|---|---|---|
| 4 mm diaphragm | +100 | −20 | |
| Injection endcap 3 | +100 | −20 | |
| Injection endcap 2 | +90 | −20 | |
| Injection endcap 1 | +90 | +30 | |
| Injection correction 2 | +66 | +20 | |
| Injection correction 1 | +17 | +20 | |
| Ring | 0 | 0 | |
| Extraction correction 1 | +17 | | −1 |
| Extraction correction 2 | +66 | | −5 |
| Extraction endcap 1 | +100 | | −5 |
| Extraction endcap 2 | +100 | | −5 |
| Extraction endcap 3 (2 mm diaphragm) | +100 | | −5 |

diameter of the magnetron orbit of all ions at the end of the excitation will be more than 2 mm, which is the diameter of the extraction aperture (see Fig. 4.5, (3)). The magnetron frequency of the 100 V deep first trap is $\approx$ 1725 Hz. Typical magnetron excitation is switched on for a duration of 10 ms with an amplitude of 300 mV. The starting phase of the excitation is fixed relative to the instant in time when the trapped bunch was released from the RFQ. This will ensure that every bunch will be treated the same even if the ions are injected off-axis such that ions already have some magnetron motion prior to the magnetron excitation.

#### Quadrupole excitation in the gas-filled purification trap

After the magnetron excitation, the quadrupole excitation is switched on to re-center the ions-of-interest. As already explained in section 3.1.2, the quadrupole excitation couples the two radial motions with frequency $\nu_c$. As the ions are having only magnetron motion, the excitation will convert the magnetron motion to the cyclotron motion. As there is buffer gas present to cool any fast motion away (including $\nu_+$), the converted cyclotron motion gets cooled away. Due to the presence of dissipative forces, conversion from magnetron to cyclotron motion happens in a wider frequency

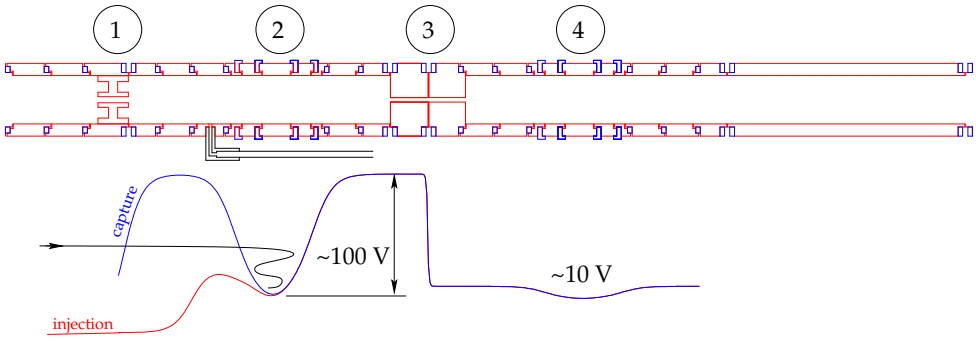


**Figure 4.5:** The two Penning traps: center of the purification trap (2) and the precision trap (4). The helium buffer gas is limited to the purification trap with two diaphragms (1) and (3) that have inner diameters of 4 mm and 2 mm, respectively. The lower graph shows the electric potential along the symmetry axis before and after the capture of the ion bunch.

range than is expected such as in Fig. 3.4. Generally, higher mass resolution is obtained with small bunch sizes and low buffer gas pressure, and the centering time needs to be longer. On the other hand, high transmission can be reached with reduced resolution and increased buffer gas pressure and bunch sizes. A full-width at half-maximum ($\Delta\nu_{\mathrm{FWHM}}$) as low as 7 Hz has been reached, which corresponds to a mass resolving power $R = M/\Delta M \approx 150{,}000$ for ions having $A/q = 100$.

An example of a "medium" resolution scan is shown in Fig. 4.6. A quadrupole excitation time of 40 ms and an amplitude of 500 mV was used. This is an example of a situation where the purification trap is used to clean rather exotic elements that have large mass differences. It is even possible to prepare isomerically clean beams with the purification trap if the mass difference is large enough to separate them.

Typically, $\approx$ 300 ms is needed for high-resolution isobaric cleaning. For the scan shown in Fig. 4.6, only 111 ms cycle time was used, resulting in a mass resolving power $M/\Delta M \approx 43{,}000$. The timing scheme is shown in Fig. 4.7. First a sufficient amount of ions are accumulated in the RFQ. Next, the bunch is released within 20 $\mu$s from the RFQ towards the purification trap. Simultaneously, the injection wall of the purification trap is kept open for ions to enter. The wall is closed 126 $\mu$s later when the bunch is in the purification trap. After capture, 40 ms is used for cooling the ions. Then, the magnetron excitation is switched on for 10 ms, which will drive all ions to a large magnetron orbit. The typical amplitude is of the order of 500 mV. Subsequently, a quadrupole excitation of 300 mV amplitude is switched

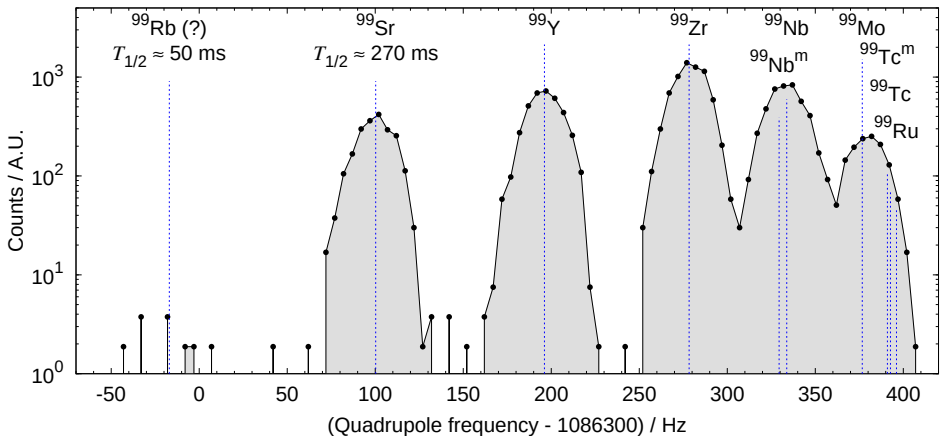


**Figure 4.6:** Quadrupole frequency scan of ions having $A = 99$ produced in proton-induced fission. Cyclotron resonance frequencies $\nu_c$ for various products has been labelled and marked with dashed lines. Half-lives of the marked elements are longer than 1 s except for those given below the label. The isomers and elements close to the stable $^{99}$Ru are not fully separated. A full-width at half-maximum ($\Delta\nu_{\mathrm{FWHM}}$) of 25 Hz is obtained, which corresponds to a mass resolving power $M/\Delta M \approx 43{,}000$.

on for 40 ms to mass-selectively bring the ions back to the center. After 20 ms of *radial* cooling time the bunch is ready to be extracted.

The cleaned bunch is either transferred to the precision trap for even higher resolution cleaning or for mass measurements. Alternatively the bunch can be ejected directly out from the trap setup for decay spectroscopy.

### 4.2.3 Precision trap

Transfer of ions from the purification trap to the precision trap is performed with fast switching of the potential walls between the traps. Typical transfer voltages are written in tables 4.1 (extraction column) and 4.2 (injection column).The depth of the precision trap is only 10 V opposed to 100 V of the purification trap to minimize axial energy spread. The 2 mm diaphragm electrode is not only used to reject isobaric contaminants but also to suppress the flow of helium buffer gas to the precision trap which is operated in as good vacuum as possible to minimize damping forces.

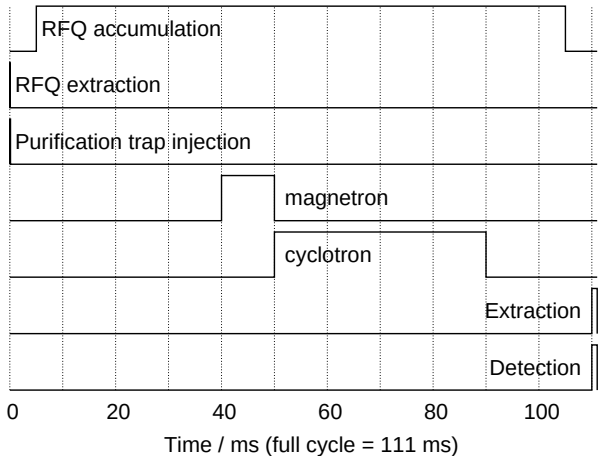


**Figure 4.7:** Timing scheme for isobaric purification in the purification trap. Accumulation of ions in the RFQ and the cleaning in the purification are performed in parallel.

**Table 4.2:** The voltages used in the precision trap. All voltages are given in Volts (V) and are relative to the ring electrode potential of the precision trap. Note that the purification trap ring electrode has 4.4 V lower potential than the precision trap ring electrode.

| Electrode | trapped | injection | extraction |
|---|---|---|---|
| Injection endcap 3 (2 mm diaphragm) | +10.0 | −9 | |
| Injection endcap 2 | +10.0 | −9 | |
| Injection endcap 1 | +10.0 | −9 | |
| Injection correction 2 | +6.6 | −9 | |
| Injection correction 1 | +1.7 | −9 | |
| Ring | 0 | 0 | |
| Extraction correction 1 | +1.7 | | −1 |
| Extraction correction 2 | +6.6 | | −1 |
| Extraction endcap 1 | +10.0 | | −1 |
| Extraction endcap 2 | +10.0 | | −1 |
| Extraction endcap 3 | +10.0 | | −1 |

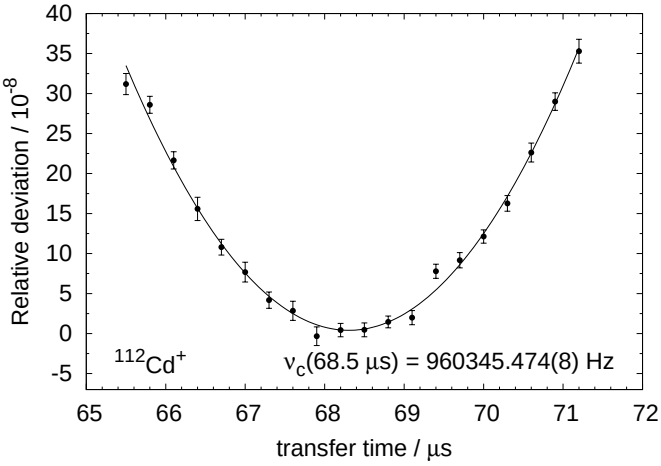


**Figure 4.8:** A transfer time scan for $^{112}Cd^{+}$ ions. The measured cyclotron frequency has a minimum at $T \approx 68.4$ $\mu$s, which is the optimum transfer time. As the frequency has a local minimum, it implies that the magnetic field in the center of the trap is weaker than on average at larger trap radii.

The optimum transfer time between the traps can be determined by checking the cyclotron frequency for the ions as a function of the transfer time. If the transfer time is not optimum, the ions gain axial energy and thus probe a longer extent of the axial magnetic field, which appears to have a small gradient near the geometric center of the trap. Since the ions will feel a different magnetic field strength, the resulting cyclotron frequency will be shifted. The optimum time of capturing will then be the local minimum or maximum of the cyclotron frequency. This is illustrated in Fig. 4.8. In the case of JYFLTRAP, the magnetic field is slightly weaker in the geometric center of the trap than *on average* around the center. In the case of $^{112}Cd^{+}$, the optimum transfer time is 68.4 $\mu$s. The transfer time scales with $\sqrt{m}$, which can be used as a scaling factor for ions having different $A/q$.

As the shimming data from the magnet manufacturer (Magnex Scientific) suggests, the magnetic field in the electric field axis has a local minimum in the center of the precision trap and a local maximum in radial plane. The magnetic field homogeneity in both traps is plotted in Fig. 4.9. The field homogeneity (maximum deviation ($\Delta B/B$) from the center-of-trap field) is about $4.3 \times 10^{-7}/\mathrm{cm}^3$ in both traps.

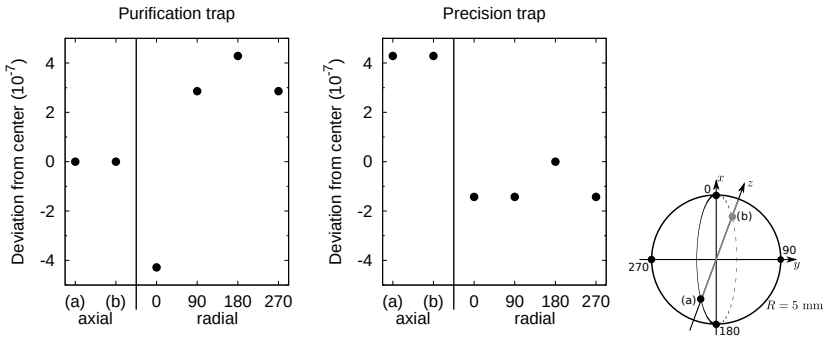


(a) Purification trap homogeneity.

(b) Precision trap homogeneity.

**Figure 4.9:** The magnetic field homogeneities of the traps. Plotted is the relative deviation of the magnetic field 5 mm away from the center of each trap. The points are measured 5 mm to each coordinate axis direction from the center. The $z$ direction is along the magnetic field lines and $xy$-plane the radial plane.

### Dipole cleaning

Once the bunch has been captured in the precision trap, the excitations of the ion motions can start immediately. In principle, there is no gas to damp the ion motion although some residual gas exists. The limited resolution that is found in the purification trap due to the residual gas does not exist in the precision trap. The amplitude increase due to dipolar excitation is shown in Fig. 3.6, right. An important point to note is that the resolution can be improved by increasing the excitation time.

The idea behind isomeric cleaning is to excite the unwanted ion species to a large radial orbit. In this case as the excitation needs to be highly mass selective, it is the cyclotron motion amplitude that is increased. The final amplitude should be such that the ions will either hit the electrode or at least have such a large radial extent that they will not reach the time-of-flight detector if extracted. High-resolution dipolar cleaning has been successfully implemented at the ISOLTRAP mass spectrometer, where isomeric states of $^{68}$Cu and $^{70}$Cu were separated in a cleaning process of several seconds [71, 72].

An alternative for the high-resolution cleaning was developed during the course of this thesis work. A cleaning procedure that is about ten times faster and employs

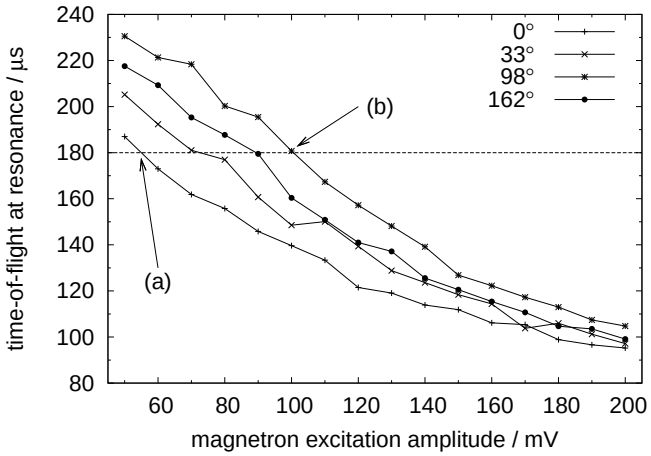


**Figure 4.10:** Effect of different magnetron excitation phases. For a given phase $\varphi$ the magnetron excitation amplitude is varied. After the dipole excitation, the magnetron motion is converted to cyclotron motion to see the difference in radius. The same radius can be obtained by using phase $\varphi = 0$ and amplitude of 55 mV (a) or by using phase $\varphi = 98^\circ$ and amplitude 100 mV (b).

excitations with time-separated oscillatory fields is described in chapter 4.4.

### Magnetron dipole excitation

The next step after isomeric cleaning (if it is needed) is to induce more magnetron motion for the ions. It is important to lock the starting phase of the magnetron excitation to the magnetron motion phase of the ions [73]. If the excitation is not phaselocked, the magnetron radius will vary from one bunch to the next since the magnetron excitation can also reduce magnetron radius. There can be even unnecessary frequency shifts involved since ions with different magnetron radius will probe different part of the magnetic field.

The effect of different magnetron excitation phases is illustrated in Fig. 4.10. Depending on the phase difference of the dipole excitation and the initial motion of the ions, the excitation changes the magnetron radius by different amounts when a constant amplitude is used for excitation. In fact, magnetron motion can even be used to *reduce* the magnetron radius of the ions provided that the ions have a well-defined magnetron phase prior to the excitation. If a fixed magnetron radius is

desired (for instance such that ions on resonance have a time-of-flight of 180 $\mu$s as marked with the dashed horizontal line in Fig. 4.10), the excitation phase needs to be fixed and the amplitude chosen so that the desired time-of-flight is obtained.

One way to avoid the need of magnetron excitation is to use electric fields between the traps which can be used to deflect the ions from the optical axis and thus ions would already have magnetron orbit when entering the trap. This, so-called Lorentz steerer is in use at the LEBIT trap [61, 74] and also at TITAN trap [56]. Magnetron excitation typically lasts for 1 magnetron period, which for JYFLTRAP is about 5.5 ms. Therefore, if very short-living ions are being measured it is even worth saving 5 ms using the Lorentz steerer.

### Quadrupole excitation in the precision trap

The quadrupole excitation is used to convert the radial motions from one to the other. If the ions prior to excitation have only magnetron motion — which usually is the case — a full conversion from one motion to the other occurs in 800 ms of excitation time if 14 mV of amplitude is used. This is experimentally determined by fixing the excitation frequency to the cyclotron frequency of the ion species and by scanning over the excitation amplitude, shown in Fig. 4.11.

If 28 mV of amplitude is used, the motion is converted from magnetron to cyclotron and again back to magnetron motion. Usually the amplitude is chosen so that only one conversion from magnetron to cyclotron motion occurs. At JYFLTRAP, one conversion occurs with

$$T_{RF}V_{RF} = 800 \text{ ms} \times 14 \text{ mV} = 11.2 \text{ mVs}. \tag{4.1}$$

For different excitation times the amplitude is easily scaled; for instance for 400 ms excitation time, an amplitude of 28 mV is needed in order to achieve one conversion from magnetron to cyclotron motion.

To create the quadrupolar r.f. electric field, an Agilent 33250A function generator[1] is used. The output of the generator is connected to the opposing quadrants of the ring electrode as shown in Fig. 3.3. The generator is set to `gated burst mode` and an external trigger is provided for the time duration that the excitation is required to be on. This particular function generator model outputs a wave that starts on a defined (zero) phase.

[1] see: `http://www.agilent.com`

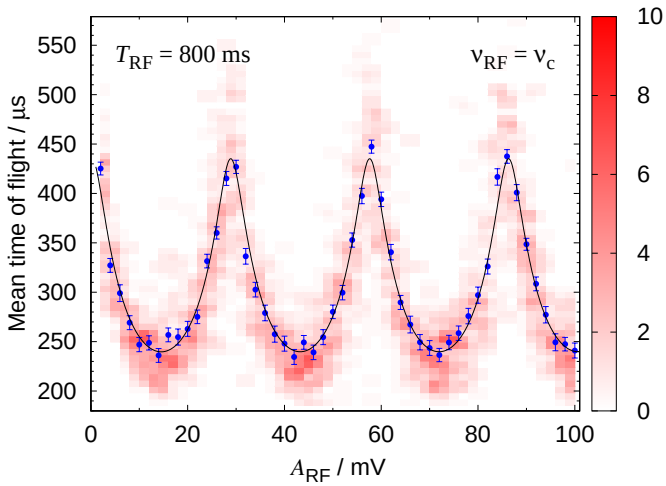


**Figure 4.11:** Mean time-of-flight of $^{85}Rb^{+}$ ions as a function of the quadrupole excitation amplitude. An excitation time of 800 ms was used. As amplitude is increased, more conversions between magnetron and cyclotron motion occurs. The faster the time of flight the more cyclotron motion. Ions have a pure cyclotron motion when an amplitude of $(2n + 1) \times 14$ mV, $n = 0, 1, 2, \ldots$ is used or have a pure magnetron phase when the amplitude is $2n \times 14$ mV, $n = 0, 1, 2, \ldots$. Ions per pixel is indicated on right; at most 10 ions per pixel was observed.

### Quadrupole excitation with initial cyclotron motion

So far the resonances shown have been obtained for ions having only magnetron motion prior to the cyclotron excitation. This effectively means that two fitting parameters have no effect on the fit: the initial cyclotron radius ($\rho_+(0)$) and the phase between the r.f. field and the initial cyclotron motion.

Any additional initial cyclotron motion considerably changes the lineshape of the resonance. Since conversion is not purely from one motion to the other, the phase between the exciting wave and the ion motion becomes an important parameter. Considering the origin of the initial cyclotron motion, it could be caused by three reasons:

1. Inadequate cooling of the ion motion in the purification trap
2. off-axis injection to the precision trap
3. deliberately adding cyclotron motion with a dipole electric field having frequency $\nu_+$.

The first source could originate from insufficient cooling of ions after the quadrupole (centering) excitation in the purification trap. This could happen if the buffer gas pressure in the purification trap is too low or too short a cooling time is used to cool the cyclotron motion away. As a result, ions still have some residual cyclotron motion left when they enter the precision trap. Since the motion is remnant from collisions with buffer gas atoms, the cyclotron motion phase and radius of the bunch in question are not well defined but distributed over an interval. This will result in scattering of cyclotron and magnetron radii after the quadrupole excitation and is definitely an undesired situation.

The second source could occur when ions are injected off-axis to the Penning trap. As the injection is a fast process, the resulting motion is well defined and thus phaselocking of the quadrupole excitation to the cyclotron motion can be done. This effect has been studied at the LEBIT [49], where a Lorentz steerer was used to introduce initial magnetron motion for the ions. In this process also a small component of cyclotron motion is given to the ions.

The third option is to deliberately introduce cyclotron motion amplitude for the ions. This could be done by using a dipole electric field having a frequency $\nu_+$ of the ions. To avoid a random phase, the excitation should be phase-locked for example to the instant of ion injection to the precision trap. Since the reduced cyclotron frequency

is about 1 MHz for ions having $A/q \approx 100$, the requirement from timing jitter is well below one cyclotron period; on the order of 0.01 $\mu$s. In addition, the quadrupole excitation phase need to be fixed to the dipole excitation phase to avoid random phase and scatter of ion motion amplitudes during the quadrupole excitation.

A test with added cyclotron amplitude was performed as shown in Fig. 4.12. $^{136}Xe^{+}$ ions were used which had a (reduced) cyclotron frequency of $\approx$ 850 kHz. First, magnetron motion was introduced with a phase-locked dipole electric field at the magnetron frequency for one magnetron period of 5.5 ms and then cyclotron motion with a phase-locked dipole r.f. electric field at the reduced cyclotron frequency for 15 ms. Subsequently, quadrupole r.f. excitation was switched on for 285 ms to convert the motions. The amplitude of the quadrupole excitation was chosen such that the effect of the excitation would be one conversion pulse as shown in Eq. (4.1). In the resonances shown in Fig. 4.12, the fitted magnetron radius was $\approx$ 0.65 mm and the fitted cyclotron radius $\approx$ 0.35 mm. The fitted phases are marked on the plot and the fitted cyclotron frequency is marked with a vertical bar.

It is important to notice that the time-of-flight minimum does not necessarily mark the resonance frequency $\nu_c$. If the ions could be prepared such that they would only have initial cyclotron motion prior to the quadrupole excitation, the phase term would again have no effect at all. As it is rather difficult to prepare ions with no magnetron motion at all, it is desirable to make the quadrupole resonance such that the magnetron motion is converted to cyclotron motion — not vice versa. In addition, fitting the resonances where ions had initially both motions might introduce frequency shifts.

#### Quadrupole excitation with time-separated oscillatory fields

The excitation with time-separated oscillatory fields (the Ramsey method) is obtained somewhat differently. In order for the Ramsey excitation to work, the fringes of the excitation have to be phase coherent as illustrated in Fig. 4.13.

If the Agilent 33250A function generator is operated in a `gated burst mode`, the excitation will resemble the one shown in (c) or (d) of Fig. 4.13. Case (c) is very unlikely since the start time of the second fringe is fixed relative to the first fringe; *not* to the exciting wave. Most likely the situation will look like (d), where no coherence is preserved. To achieve proper operation, the function generator is operated in `amplitude modulation mode`: another function generator is used to provide the modulating signal which in this case is a square wave. This will randomize the

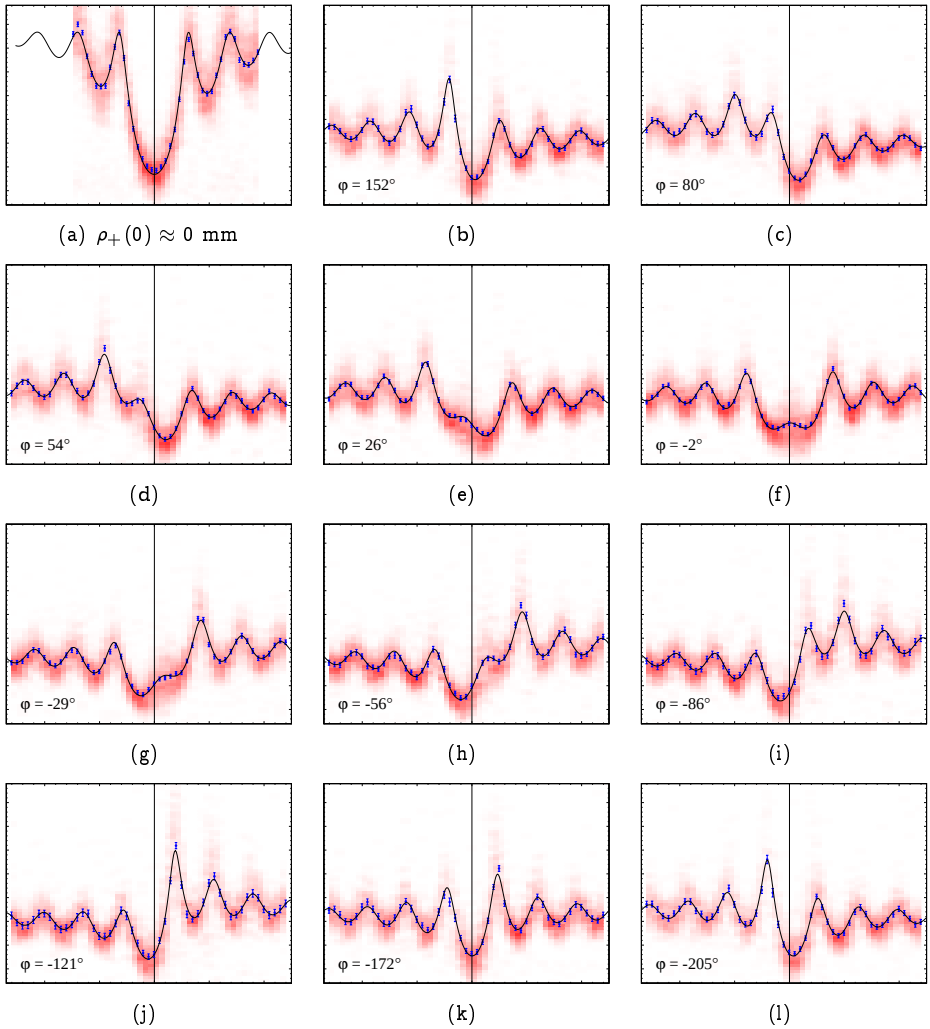


**Figure 4.12:** (a) Time-of-flight cyclotron resonance obtained for ions having initially only magnetron motion. (b)-(l) Resonances obtained for ions having initially both magnetron and cyclotron motion. Starting phase $\varphi$ of the quadrupole excitation (with respect to the starting time instant of the dipole excitation with $\nu_+$, which was used to induce initial cyclotron motion) was varied over 1 cyclotron period of $\approx 1.2$ $\mu$s with 0.1 $\mu$s steps. The fitted $\nu_c$ is indicated with a vertical bar.

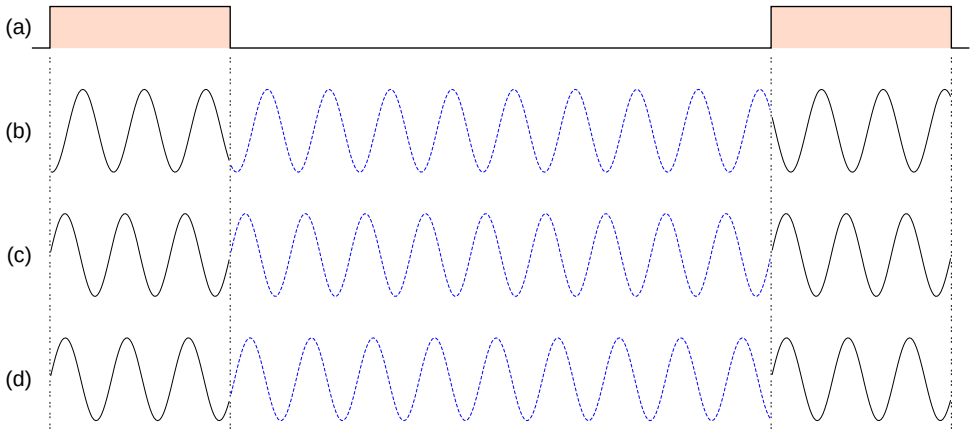


**Figure 4.13:** Phase coherence in excitation with time-separated oscillatory fields. (a) Amplitude of the exciting wave as a function of time. (b)-(d) solid line: excitation on; dashed line: excitation off period which is coherent to the first fringe. See text for further explanation.

starting phase of the first fringe but will keep phase coherence over the output-off period. This is the case (b) in Fig. 4.13. As the ions are only prepared with magnetron motion to start with, the starting phase is not critical. (c) would be the ideal case but to achieve that the starting time of the second fringe has to be matched to the first one with an external timing card. For that, high precision timing is needed — even small incoherence will result in a phase shift which will lead to a frequency shift. Furthermore, since the frequency is scanned over an interval, the starting time of the second fringe needs to be changed constantly. Thus it is easier and safer to operate the function generator in the `amplitude modulation mode`.

### 4.2.4 Ejection and detection

Once the motion excitations with radiofrequency electric fields have been finished, the ions are extracted from the trap. The potential wall of the extraction side is quickly (within 200 ns) lowered to let ions fly towards the micro channel plate (MCP) detector for time-of-flight determination. For cyclotron resonance frequency determination, the most important factor is how well the resonance can be distinguished from the "background", which in the absence of real contamination is the time-of-flight of ions from the trap to the detector without quadrupole excitation.

One way to quantify the resonance quality is to use the "time-of-flight" effect:

$$\mathrm{TOF}_{\mathrm{effect}} = \frac{\mathrm{TOF}(\nu_{\mathrm{RF}} \neq \nu_c) - \mathrm{TOF}(\nu_{\mathrm{RF}} = \nu_c)}{\mathrm{TOF}(\nu_{\mathrm{RF}} \neq \nu_c)}, \tag{4.2}$$

where $\mathrm{TOF}(\nu_{\mathrm{RF}} \neq \nu_c)$ is the time-of-flight of ions far from the resonance frequency and $\mathrm{TOF}(\nu_{\mathrm{RF}} = \nu_c)$ the time-of-flight of ions at the resonance frequency. Typically JYFLTRAP was tuned to have time-of-flight effect of $\approx 40$ %. Unfortunately the time-of-flight effect does not take the scattering of the ion flight times into account at all.

A more improved way of determining the resonance quality is to derive the so-called *signal-to-noise ratio*, $S/N$. It is rather similar to the time-of-flight effect but takes the time-of-flight scattering of ions into account:

$$S/N = \left| \frac{\overline{\mathrm{TOF}}_1 - \overline{\mathrm{TOF}}_2}{\sqrt{\sigma_1^2 + \sigma_2^2}} \right|, \tag{4.3}$$

where $\overline{\mathrm{TOF}}_1$ and $\sigma_1$ are the average time-of-flight of ions and the standard deviation of the time-of-flight of ions at the resonance frequency ($\overline{\mathrm{TOF}}_2$ and $\sigma_2$ similarly for off-resonance ions).

A resonance with a determined signal-to-noise ratio is shown in Fig. 4.14. In this case, an excellent signal-to-noise ratio of about 5 is obtained. To obtain high signal-to-noise ratios, the purification trap settings have to be carefully optimized such that the bunch leaving from the purification trap is properly centered and cooled.

### Time-of-flight recording

A micro-channel plate (MCP) detector setup with a two-plate chevron configuration is used for time-of-flight recording. The signal is amplified with a preamplifier and fed into an SR430 multi-channel scaler (MCS). The scaler is triggered at the same time instant as the ejection of ions from the trap. The detection times are binned (typically) to 640 ns slots. Once a trigger for the MCS has been registered, the number of ions as a function of time is recorded. The typical time window for registering ions is 1024 channels which corresponds to 655.36 $\mu$s with 640 ns bin width. Once the spectrum is collected, the Labview program running on the measurement PC reads the data from the MCS via a GPIB bus. Since the ions have 30 $q$keV of kinetic energy when hitting the detector, the detection efficiency is rather high. In 2006, the MCP efficiency was determined to be about 60 % with radioactive $^{26}\mathrm{Al}^m$

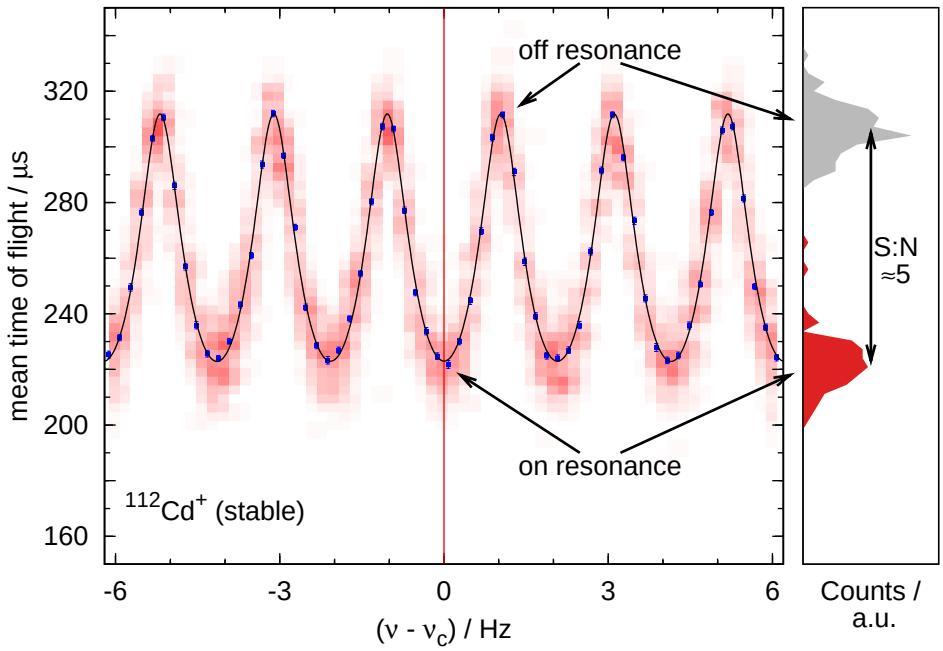


**Figure 4.14:** Signal-to-noise ratio of a resonance. Two frequency points are chosen for calculating the time-of-flight and its standard deviation for both on- and off-resonance ions. The distribution of ions as a function of time-of-flight in both cases is shown on the right. In this case, the baseline is clearly separated from the resonance and an excellent signal-to-noise ratio $S/N \approx 5$ is obtained.

ions by comparing the saturated beta-decay rate of $^{26}Al^m$ measured with a silicon detector to the counting rate of $^{26}Al^m$ ions measured with the MCP detector.

## 4.3 Isobarically clean beams for trap-assisted spectroscopy

The trap setup is not only used for mass measurements but also to provide isobarically clean beams for decay spectroscopy. Fur this purpose, the purification trap is used. Instead of transferring the cleaned bunches to the precision trap for mass measurements, the bunches are let through the second trap and all the way to the decay spectroscopy station.

Since the beam quality requirements — emittance and energy spread — are not as strict as for mass measurements, the trap can be optimized to perform cleaning as fast as possible. The fastest cleaning cycle so far has been in a branching ratio measurement of the superallowed beta emitter $^{62}$Ga [75]. The trap system was used to clean $^{62}$Ga ($T_{1/2} \approx 116$ ms) from overwhelming contaminations of $^{62}$Zn and $^{62}$Cu. A mass resolving power ( $R = M/\Delta M$) of 20,000 was reached, which was enough to separate $^{62}$Ga from the neighbouring contaminants. In this experiment, ions were first accumulated in the RFQ for 71 ms and then another 71 ms was used for isobaric cleaning. The accumulation and cleaning were done in parallel mode.

Isobaric cleanliness is especially important when ions are produced in fission. A large variety of different ion species are produced as can be seen for example in Fig. 4.6 and thus lots of isobaric background radioactivity is expected. If the trap is used for isobaric cleaning, only the ion-of-interest is transported through. The only background arises from decay daughters of the ion of interest. A tape transport system can be used to regularly transport away the build-up of background radioactivity. Several experiments using ions produced in fission have been performed [76, 77] and more are foreseen in the near future.

### 4.3.1 Multiple-injection mode

A special case of decay spectroscopy was the half-life measurement of the superallowed beta emitter $^{26}$Si [78]. In principle, the experiment was straightforward: accumulate ions for $\approx$25 seconds, clean the bunch of isobaric contaminants and release the bunch of $^{26}$Si to the detector setup for 25 seconds (about $10T_{1/2}$ of $^{26}$Si) of decay measurements. Another important requirement for the $^{26}$Si beam was that the

bunch had to implanted in a short, fixed, time instant and that only single implantation is allowed since the daughter activity ($^{26}\mathrm{Al}^m$, $T_{1/2} = 6.3$ s) will immediately start to grow in after the implantation and thus fitting of the decay period would be difficult.

Due to space charge limits, the RFQ and the purification trap could not be operated with a large number of ions which would be accumulated in parallel to the 25 seconds of the decay period. It was discovered that the purification trap reached the space charge limit with about 300 ms of accumulation, containing only about 50 ions of $^{26}$Si.

To overcome the space charge limit, the purification trap was operated in a multiple-injection mode, which is illustrated in Fig. 4.15. Firstly, a bunch of ions is accumulated in the RFQ, transferred to the purification trap and isobarically cleaned. The bunch is released from the purification trap towards the precision trap. The contaminants are rejected since they hit the diaphragm electrode having an aperture of 2 mm. Instead of extracting the ions to the decay spectroscopy setup, they are reflected back to the purification trap and recaptured. After a short while, the ions are axially recooled back to the center of the trap. At this stage, the purification trap is filled only with $\approx$ 50 ions of $^{26}$Si.

Next, a new bunch from the RFQ is transferred into the purification trap. The injection side potential wall is shaped such that the ions that are already in the trap do not escape towards the RFQ. The new bunch is axially cooled and the whole isobaric cleaning process is repeated. The already cleaned bunch of ions mix with the new bunch and undergo the isobaric cleaning again. The cleaning-rejection-recapturing can be repeated several times and with every extra bunch the fraction of desired ions ($^{26}$Si) is increased. When the amount of desired ion species is saturated, the isobarically clean bunch is released to the spectroscopy setup. A rate of $\approx$ 250 ions/bunch was obtained with 8 cycles of cleaning.

Prior to the $^{26}$Si on-line run, a study with stable $^{129}\mathrm{Xe}^+$ ions from the IGISOL off-line spark ion source was performed (see Ref. [79] for more details about the spark source). Up to four bunches were injected before the final extraction. The bunch size could be increased from individual 80 ions/bunch up to final accumulated 220 ions/bunch. In this case, the trap was saturated already with accumulated 4 bunches, being comparable to $^{26}$Si case. The results are shown in Fig. 4.16.

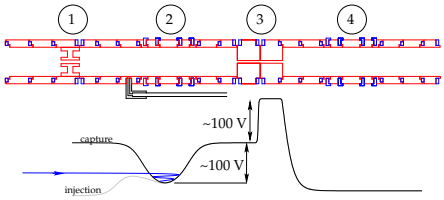


(a) Capturing of the first bunch from the RFQ.

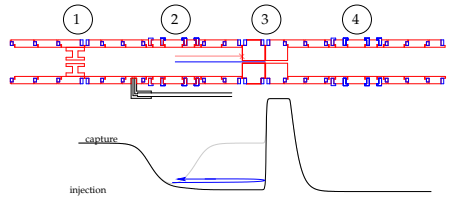


(b) Sideband cleaning to reject isobaric contaminants and recapturing the cleaned bunch in the purification trap.

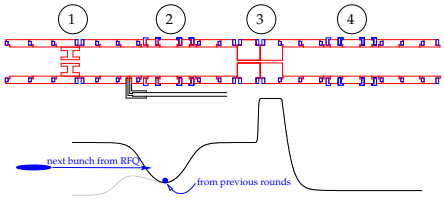


(c) Capturing another bunch from the RFQ and repeating the isobaric cleaning.

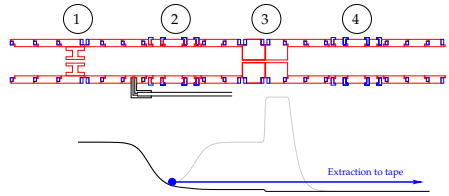


(d) The final extraction.

**Figure 4.15:** Multiple injection scheme. The steps (b) and (c) are repeated over several times to achieve the desired bunch size. See Fig. 4.5 for explanation of the numerical symbols (1)–(4).

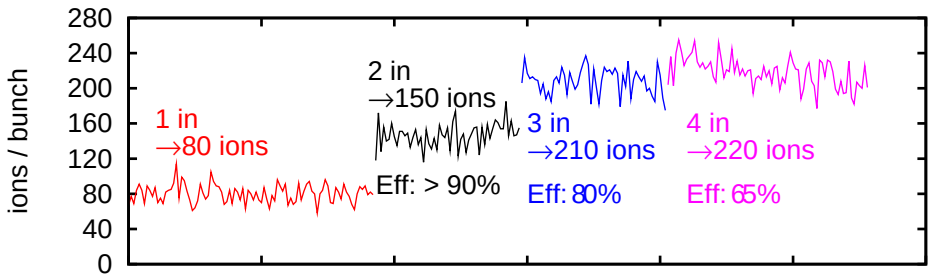


**Figure 4.16:** Accumulation of ions with the multiple-injection scheme. As the beam from the IGISOL off-line ion source was rather clean and composed mostly of stable $^{129}$Xe, the bunch size is maximized rather quickly.

## 4.4 Preparing isomerically clean beams

The resolution of the purification process in the purification trap is limited to about 10 Hz due to the presence of the buffer gas. If there would be ion species having cyclotron frequency differences of less than 10 Hz, the purification would not just transmit the ion species of interest but also a fraction of the other species. Since the set cyclotron (centering) frequency is not optimum for the other species, the different species end up having different residual magnetron orbits after quadrupole excitation. This will cause a different time-of-flight effect for the two species. Even worse, the different species will feel different parts of the magnetic field and thus there can be frequency shifts due to magnetic field inhomogeneity.

Often with isomeric states the separation energy between the states is so low that the peaks are completely unresolved in the purification trap. Since the precision trap is situated in ultra-high vacuum ($p \leq 10^{-7}$ mbar) and both the cooling and the re-centering effect of the buffer gas are missing, the ion motions have to be excited differently in order to produce clean ion samples. Here, a dipolar excitation at the reduced cyclotron frequency $\nu_+$ is typically used.

To remove contaminant ions prior to the measurement process, their radial amplitudes need to be increased such that they will not affect the ions of interest. The time profile of the excitation results in a finite lineshape in the frequency domain, given by the Fourier transformation, where $\Delta\nu_{\mathrm{FWHM}}$ of the resonance is determined by the time duration $T$ of the excitation, $\Delta\nu_{\mathrm{FWHM}} \propto \frac{1}{T}$. In addition to the normal dipolar cleaning, a Stored Waveform Inverse Fourier Transform (SWIFT) [80] can be used for a selective broadband cleaning.

### 4.4.1 Dipolar cleaning with a rectangular pulse

When using a rectangular excitation pulse, the corresponding Fourier-transformation results a typical resonance curve as shown in Fig. 3.4. This is not inconvenient if the frequency difference of the ion of interest and the impurity are well known. Excitation times and frequencies need to be properly set so that after the excitation the contaminants will have a large orbit while the ions of interest not. An excitation with a rectangular pulse is shown in Fig. 4.17 (a). One of the frequencies for an ion of interest remaining unexcited is marked with (2). Despite all care to avoid excitation of the ion of interest, there might still be some excitation, for example due to the residual gas damping effect. On the other hand, the cleaning process with

a square wave excitation is more than factor of two faster than that with a Gaussian envelope.

### 4.4.2 Dipolar cleaning with a Gaussian envelope

By using a Gaussian envelope in the excitation time profile, the excitation pattern in the frequency domain is also Gaussian. In this manner, the ion of interest just needs to be sufficiently separated from contaminants in order to avoid an unwanted increase of its motional amplitudes. The resolution can be adjusted with the excitation time. This corresponds to the excitation pattern (b) shown in fig. 4.17. The contaminant, marked (0), is excited maximally while the ion of interest (3) remains unaffected.

This method is routinely used in many trap setups such as ISOLTRAP [81], Canadian Penning trap [82] and LEBIT [83]. The advantage in using dipolar cleaning is that it can be applied either in low- or high-resolution modes: using a very short excitation duration and a high amplitude will remove ions within a bandwidth of several kHz. Or, the amplitude can be set low and the duration long to obtain a narrow-band cleaning.

ISOLTRAP has demonstrated a selection of nuclear isomers [84] in combination with selective laser ionization and decay spectroscopy. Here, states of $^{70}$Cu were separated with a Penning trap. In the cleaning process, a mass resolving power of about $2 \times 10^5$ was obtained with a 3-s excitation time. Although there was only one contaminant to be cleaned with the Penning trap, it should be noted that usually several contaminants are cleaned in parallel.

### 4.4.3 Dipolar cleaning with time-separated oscillatory fields

The resolution can be further enhanced by using an excitation scheme with time-separated oscillatory fields [38, 40, 46]. It has been shown that the linewidth is reduced by almost 40 % [39]. The reduction is illustrated in Fig. 4.17, comparing the width of the main peak for (a) and (c). In case (c) the ion of interest remains unexcited at the frequency position (1) which is the nearest of the three positions to the contaminant (0). As in the case of a rectangular excitation profile, both frequencies have to be known accurately beforehand and can be used for example in measurements of superallowed beta-emitters or stable ions. This method is less suited for studying short-lived nuclides with unknown mass values.

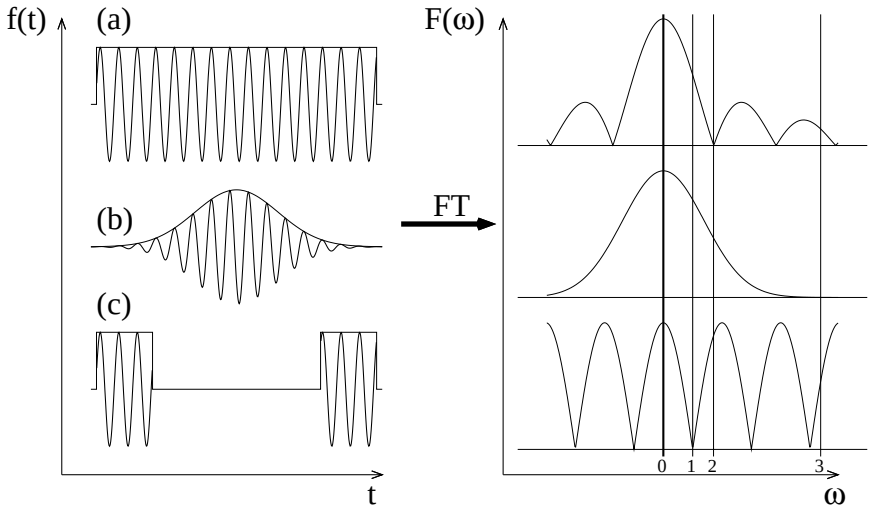


**Figure 4.17:** Examples of excitation time profiles $f(t)$ (left side) for (a) a rectangular excitation pulse, (b) a Gauss-modulated envelope and (c) an excitation with time-separated oscillatory fields. The corresponding Fourier transformations $F(\omega)$ in the frequency domain are shown on the right. The position (0) indicates the frequency of the contaminant ion species and (1) to (3) indicate a possible frequency of an ion of interest. For the discussion see text.

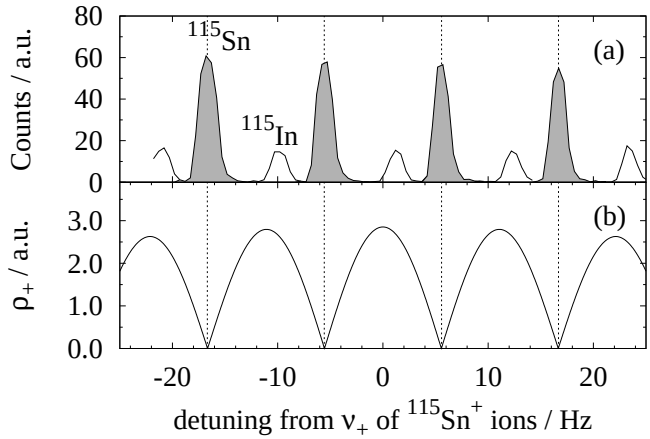


**Figure 4.18:** Number of detected ions as a function of the applied dipolar frequency in the precision trap (a). Here, an excitation time pattern of (10-80-10) ms (On-Off-On) was used. Prior to their ejection the ions have been extracted backwards, captured and re-centered in the purification trap. The individual peaks are the transmitted ions of $^{115}$Sn (grey) and $^{115}$In (white). The lower panel (b) shows the expected increase of the cyclotron radius $\rho_+$ for $^{115}$Sn as a function of the applied dipolar frequency. Here, the highest transmission occurs when least excited.

### 4.4.4 Isomeric cleaning with time-separated oscillatory fields and additional cooling

In the methods introduced so far, the cleaning is performed in such a way that the contaminants are driven to orbits with large radii such that they hit the ring electrode. To avoid excessive excitation, the ion sample can be extracted towards the purification trap. The contaminants will hit the electrode surface surrounding the 2-mm diaphragm between the traps, while the ions of interest can pass through. The remaining cleaned bunch of ions is then captured in the purification trap, where the ions are additionally cooled and re-centered by applying another quadrupole excitation. In this manner, it is possible to perform very-high resolution cleaning in a time-efficient manner. For instance, the $A/q$ doublet $^{115}$Sn$^+$ and $^{115}$In$^+$ has a cyclotron frequency difference of about 4.5 Hz. Using an excitation time pattern of (10-80-10) ms (On-Off-On) the different isotopes are fully separated. An example of a transmission curve after the second re-centering in the purification trap is shown in Fig. 4.18.

After a repeated centering and cooling in the purification trap the ion bunch is transferred to the precision trap for the actual cyclotron frequency determination. Figure 4.19 demonstrates the prospects of this cleaning procedure applied to the ground and isomeric states of $^{54}$Co. If no cleaning is applied, the ground state is rather suppressed (a). The ratio between the detected ions of isomer to ground state is about 3 to 1. In (b) the isomeric state was removed by a dipolar excitation at $\nu_+$ in the precision trap, as described in section 4.4.4, resulting in a clean resonance of the ground state. In (c), the ground state was removed in analogy to case (b). The timing scheme to perform the measurement is shown in Fig. 4.20.

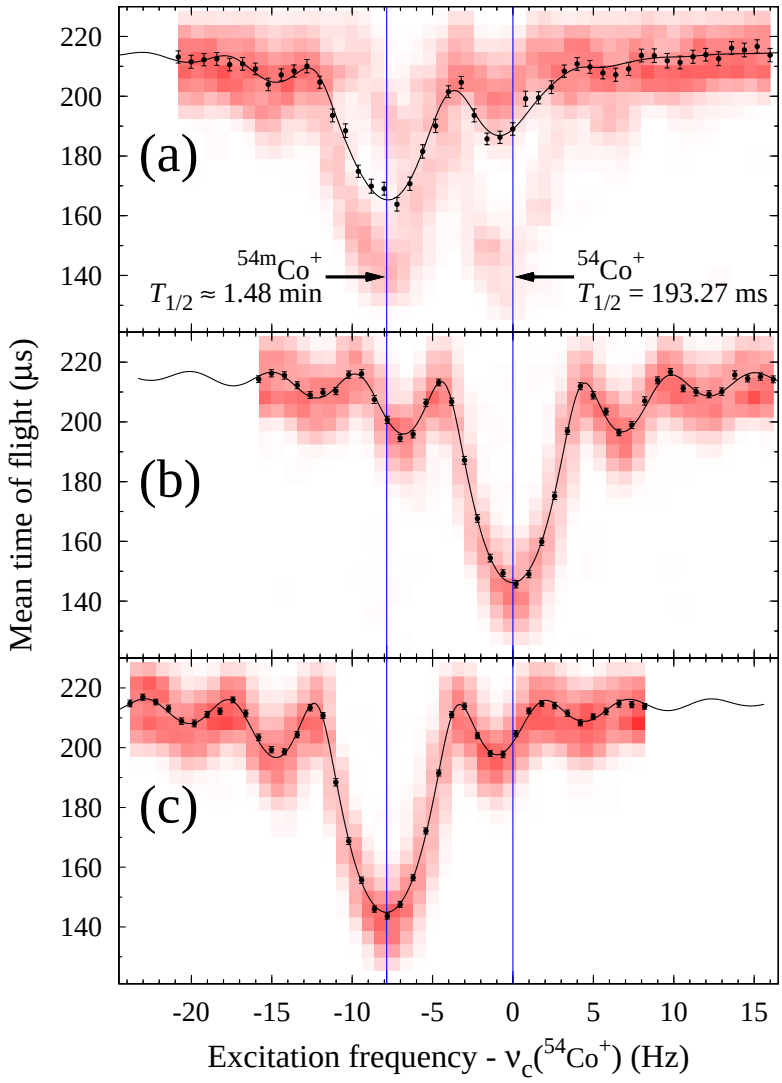


**Figure 4.19:** Time-of-flight ion cyclotron resonances and a two-peak fit for an uncleaned ion sample (a). In the middle panel (b), the isomeric state $^{54}Co^{m}$ has been cleaned away, which remarkably enhances the resonance of the ground state. In the bottom panel (c), the ground state has been removed from the precision trap.

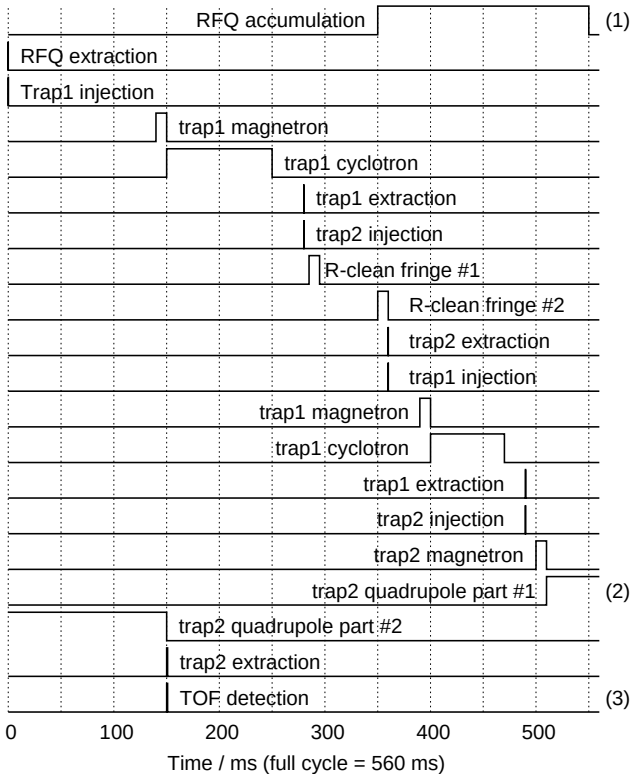


**Figure 4.20:** Timing scheme for Ramsey cleaning and time-of-flight ICR measurement. The steps are chronologically for one bunch of ions. The accumulation in the RFQ (1), the cleanings and part of the quadrupole excitation in the precision trap (2) and the other part of the quadrupole excitation and extraction (3) are performed in parallel.

# 5 Analysis procedure

The data obtained in Penning trap time-of-flight ion-cyclotron resonance (TOF-ICR) mass spectrometry consists of the time of flight of ions as a function of the frequency of the exciting r.f. field. This is usually the quadrupolar r.f. field having a frequency close to the cyclotron frequency of the ion of interest. The lineshape of the resonance is well described in Ref. [36] for a rectangular excitation amplitude shape and in Ref. [39] for time-separated oscillatory fields. The different fitting parameters and their physical meanings are described in chapter 3.1.2.

In this chapter a thorough explanation is given to how the data is treated such that the theoretical lineshape can be fitted. Also, different sources of error are presented and the moment in which they enter the calculations.

## 5.1 Determining the time of flight

The time of flight of an ion from the trap to the detector is a function of the ion's mass, charge and initial velocity. Also the shapes of the electric and magnetic fields play an important role. The fields can be simulated rather accurately for instance with the ion-optical simulator SIMION when the voltages applied to the electrodes are known. Since the mass and the charge of the ions are usually known, only the kinetic energy of the ions needs to be determined or fitted. The kinetic energy depends on the eigenmotion amplitudes, though magnetron motion can be neglected since $\nu_- \ll \nu_+$. The time of flight of an ion from the precision trap to the detector is thus given by Eq. (3.21). Since the fields are not directly available as analytical functions, the flight path can be divided into small pieces and the total time of flight $t$ can be approximated with a sum over the distance:

$$t = \sqrt{\frac{m}{2}} \sum_{z=z_0}^{z_n} \sqrt{\frac{1}{E_{tot} - q(E(z) - E(z_0)) - \mu(B(z) - B(z_0))}} \big(z_k - z_{k-1}\big), \qquad (5.1)$$

where $\mu$ is the magnetic moment, $m$ the mass, $q$ the charge and $E_{tot}$ the sum of all eigenmotion energies: axial kinetic energy, radial kinetic energy, electric potential energy and energy stored in the magnetic moment of the ion; $z_k$ are the distance

steps. The fields can be extracted from SIMION. For example with 1 mm intervals the time of flight is obtained by summing over the distance between the precision trap and the detector, which will take 1600 summing steps as the distance is ∼1.6 m.

Another approach is to approximate the fields with polynomial functions. In order to do this, the electric field is assumed to be constant over each electrode and the shape of the magnetic field can be approximated with four parabolas that each extend over a certain length. In this manner, the summing over 1600 steps is reduced to about ten definite, analytically solvable integrals which will considerably simplify and speed up time-of-flight calculations.

The integral in Eq. (3.21) is thus of the form

$$\int \frac{dx}{\sqrt{ax^2+bx+c}} \tag{5.2}$$

and the analytical solution

$$\begin{cases} \frac{1}{\sqrt{a}} \ln\left(2\sqrt{a}\sqrt{ax^2+bx+c}+2ax+b\right) & \text{if } b^2-4ac>0 \text{ and } a>0 \\ -\frac{1}{\sqrt{-a}} \sin^{-1}\left(\frac{2ax+b}{\sqrt{b^2-4ac}}\right) & \text{if } b^2-4ac<0 \text{ and } a<0 \\ \frac{1}{\sqrt{a}} \sinh^{-1}\left(\frac{2ax+b}{\sqrt{4ac-b^2}}\right) & \text{if } b^2-4ac<0 \text{ and } a>0 \\ \frac{2\sqrt{bx+c}}{b} & \text{if } a=0 \text{ and } |b|>0 \\ \frac{1}{\sqrt{c}} & \text{if } a=0 \text{ and } b=0. \end{cases} \tag{5.3}$$

With this, Eq. (3.21) simplifies to about 10 steps of summing. The approximated and realistic electric potentials along the optical axis are plotted in Fig. 5.1 and similarly for the magnetic field in Fig. 5.2. The approximation might not reproduce flight times of ions having big $A/q$ differences. It only affects the fitted initial axial energy value and does not shift the fitted frequency.

## 5.2 Experimental data

A time-of-flight ion-cyclotron resonance measurement proceeds one bunch at a time and only the excitation frequency is changed between the bunches. Usually 41 or 81 frequency points are scanned depending on whether conventional or Ramsey excitation schemes are used. The whole scan consists of several *scan rounds* so that for each frequency point several bunches will be recorded. How many rounds are needed depends on the production rate and the desired statistics. Often, a few thousand ions are collected.

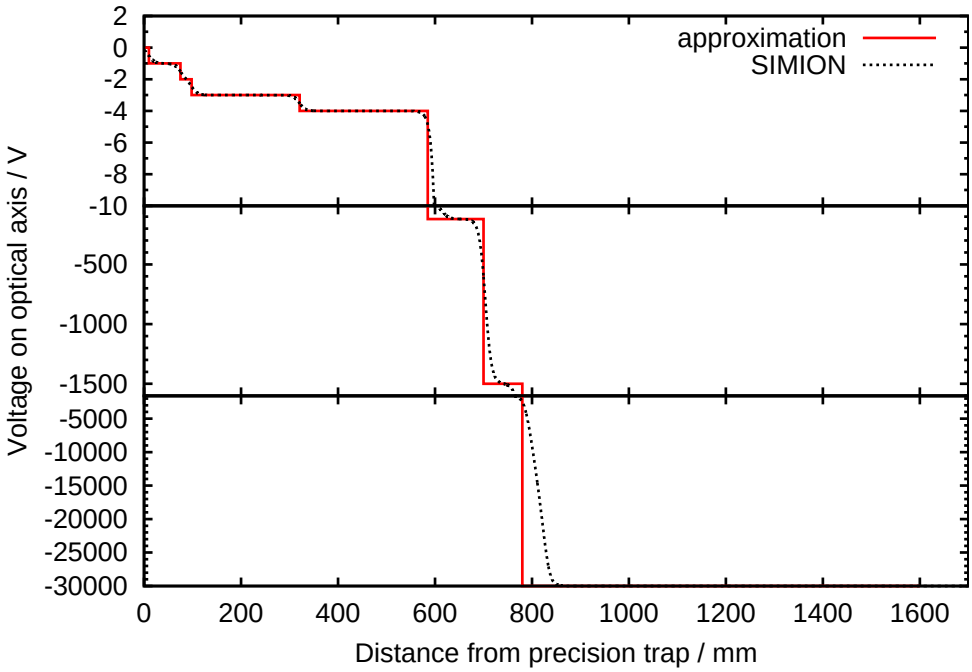


**Figure 5.1:** Comparison of the realistic (from SIMION) and the approximated electric fields. The zero-potential is chosen to be the potential of the ring electrode of the precision trap. The earth-ground in this scale is then at −30 kV. The MCP detector is located about 1600 mm away from the precision trap. The approximation reproduces the most crucial low voltage part at 0–600 mm very well.

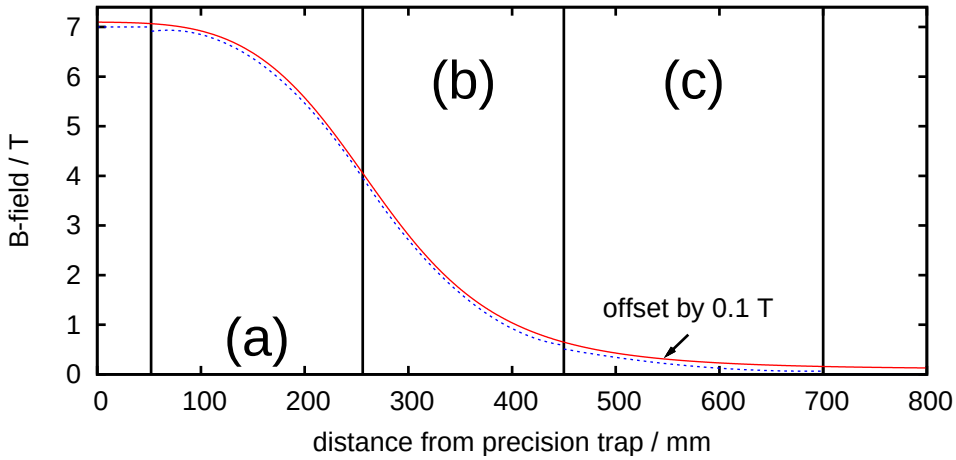


**Figure 5.2:** Comparison of the realistic and the approximated magnetic fields. The field is split in five parts, where two sections have constant 7 T and 0 T and the three sections marked (a-c) in between are well described with second order polynomial functions (dashed blue line). The realistic field shape from SIMION (solid red line) is offset by 0.1 T for clarity.

### 5.2.1 Filtering data

In general, no recorded data should be rejected without a reason. In order to provide transparency for the data, it is often a good practice to set some conditions to accept or reject bad data values.

#### Time-of-flight gate

In order to suppress the background, a gate is usually imposed which limits accepted ions possessing only a certain time of flight. This is illustrated in Fig. 5.3, where the number of ions as a function of time of flight is plotted for a resonance curve similar to Fig. 3.5. Figure 5.3 is very typical for short-lived ions. If a singly charged ion $\beta^+$ decays in vacuum (like in a Penning trap), a fraction of the decay daughter nuclei will be a neutral atom

$$ {}_{Z}A_{N}^{1+} \xrightarrow{\beta^+} {}_{Z-1}A_{N+1}^{\text{neutral}}. \tag{5.4} $$

In electron capture decay the daughter remains as singly charged

$$ {}_{Z}A_{N}^{1+} \xrightarrow{\text{EC}} {}_{Z-1}A_{N+1}^{1+} \tag{5.5} $$

and in $\beta^-$ decay the daughter becomes doubly charged

$$ {}_{Z}A_{N}^{1+} \xrightarrow{\beta^-} {}_{Z+1}A_{N.1}^{2+}. \tag{5.6} $$

However, in each case electron shake-offs [85] can occur which may modify charge state distribution of the daughter. The daughter ions have a good chance of surviving in the trap as the maximum recoil energy from $\beta$ decay is about 100 eV for decay energy of 10 MeV for $A = 100$ ions. If the ion recoils perpendicular to the magnetic field axis, it remains in the trap and once the bunch is extracted the recoil flies fast to the MCP detector due to the extra energy. This shows as a broad peak in the front of the spectrum shown in Fig. 5.3(b). Additional peaks can also appear due to charge-exchange processes of ions with the background gas atoms. Usually these contaminants have a rather fast time of flight in comparison to the ions of interest so that they can be filtered out with the time-of-flight gates.

### Countrate gate

Another useful data filtering method is to impose countrate restrictions. This limit is set on a bunch, which should only have certain number of ions. Additionally, the ions outside the time-of-flight gate are counted since the interesting quantity is the number of ions in the trap during the excitation process. Typically a gate is set to accept only 0 to 10 ions per bunch. In addition, the data can be divided into countrate classes in order to check for systematic shifts of the cyclotron frequency as a function of the number of simultaneously stored ions in the trap. This is discussed in more detail in section 5.4. A typical countrate spectrum is shown in Fig. 5.4.

## 5.3 Experimental time of flight and its uncertainty

After proper time-of-flight and countrate gates are set as described above, the time of flight and the associated uncertainty can be calculated. Since each ion has the same weight the time of flight is calculated as an average of the time of flight of each detected ion. If an ion $k$ has a time of flight $T_k$, the average time of flight, $\overline{T}$, over $N$ ions is

$$ \overline{T} = \frac{1}{N} \sum_{k=1}^{N} T_k. \tag{5.7} $$

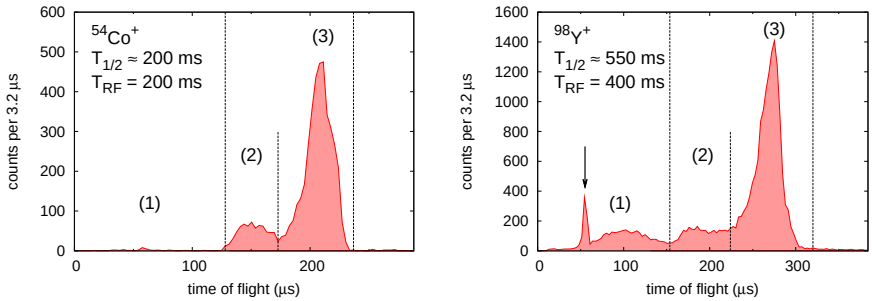


(a) Detected ions as a function of time of flight in the case of initial trapping of short-lived $\beta^+$ emitters.

(b) Detected ions as a function of time of flight in the case of initial trapping of short-lived $\beta^-$ emitters. The sharp peak (marked with arrow) are $He^+$ ions, formed in charge-exchange reactions or in collisions of $\beta$ decay recoils with residual gas atoms.

**Figure 5.3:** A typical time-of-flight spectrum of ions consisting of all ions regardless of excitation frequency. The peaks at (2) and (3) mark the ions excited with $\nu_{RF} \approx \nu_c$ and $\nu_{RF} \neq \nu_c$, respectively. The peak (1) in Fig. 5.3(b) consists of doubly-charged $\beta^-$-decay daughter ions. Their time of flight is short not only because they are doubly charged but also due to recoil energy gained in the decay process. The peak (1) in Fig. 5.3(a) is much smaller since in $\beta^+$ decay the daughter becomes a neutral atom and is lost from the trap. In any case the peak (1) can be gated out by imposing a time-of-flight interval extending between the full vertical bars.

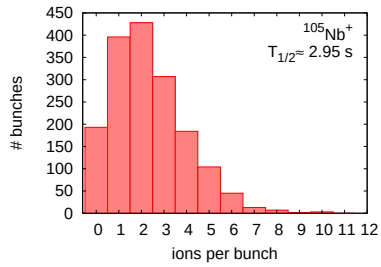


**Figure 5.4:** A typical distribution of bunches as a function of detected ions. Usually the countrate maximum is optimized to be approximately 1 to 3 ions per bunch.

The average is calculated for each excitation frequency.

As the number of detected ions for each frequency is usually rather small, it is not always possible to assign the uncertainty simply as the standard deviation of the mean for each frequency point individually. However, if statistics allow (one hundred of ions per frequency point or more), the uncertainty is obtained for each frequency as

$$\sigma\left(\overline{T}\right) = \sqrt{\frac{\sum_{k=1}^{N}\left(\overline{T} - T_k\right)^2}{N(N-1)}}, \tag{5.8}$$

which is the standard deviation of the mean.

### Low statistics cases

Often there are not too many counts per frequency point. Calculating the uncertainty with Eq. (5.8) will cause problems when

- there is only one detected ion at particular frequency — there is no deviation,
- there are several ions in one time-of-flight bin — still there is no deviation,
- there are few ions very close in time — deviation is strongly underestimated.

The situation can be improved by using *sum statistics*. There the standard deviation ($\sigma$) is calculated from all ions, regardless of their excitation frequency.

### Sum statistic

The so-called sum statistics -method assumes that the TOF distribution of ions is independent of the excitation frequency which then allows summing up of ions of every frequency and calculating the standard deviation of the whole ion distribution (for example shown in fig. 5.3). The standard deviation ($\sigma$) is

$$\sigma\left(\overline{T}\right) = \sqrt{\frac{\sum_{k=1}^{N}\left(\overline{T} - T_k\right)^2}{N-1}}. \tag{5.9}$$

After, the time-of-flight uncertainty $\sigma\left(\overline{T_k}\right)$ for frequency $k$ is

$$\sigma\left(\overline{T_k}\right) = \frac{\sigma\left(\overline{T}\right)}{\sqrt{N_k}}, \tag{5.10}$$

where $N_k$ is the number of ions detected at that frequency. The advantage of using sum statistics is that it can be used in cases with very low statistics — even frequencies with single detected ions will have a time-of-flight uncertainty. The drawback of this method is the assumption that ions at every frequency have the same mean time of flight. This is not the case since the mean time of flight is different for each frequency point. This so-called sum statistics method is in use in several Penning trap facilities such as ISOLTRAP, SHIPTRAP, TITAN, MLLTRAP and LEBIT. It should be noted that often there are so few ions available that this method is the only reasonable method to use even though it strongly overestimates uncertainties.

### Sum statistics with mean correction

Another, slightly improved way to deal with low statistics data is to use the sum statistics but correct each frequency point with its own mean time of flight and then sum every point such that the distributions have center around the mean. In order to do so, there needs to be at least ten ions in each frequency point for this treatment to give a reasonable result. If there are only very few ions per frequency point, the same problems arise as with the individual time-of-flight uncertainty determination. The advantage of the mean-correction is that the ions are allowed to distribute around their own mean value on a given frequency, not to just distribute around the mean of every frequency point.

This kind of treatment is especially fair for resonances obtained with the Ramsey technique since the whole distribution of ions have a large scatter, depending on the excitation frequency. Particularly in this case the sum statistics would strongly overestimate the uncertainty.

The standard deviation ($\sigma$) in this case is

$$\sigma\left(\overline{T}\right) = \sqrt{\frac{\sum_{\nu=1}^{M}\left[\sum_{k=1}^{N_\nu}\left(\overline{T}_\nu - T_{k,\nu}\right)^2\right]}{N-1}}, \tag{5.11}$$

where inner sum is over all ion $k$ having frequency $\nu$ and $\overline{T}_\nu$ is the mean time of flight obtained using Eq. (5.7) at frequency $\nu$. The outer sum is over all frequencies and $N$ is the total number of ions of every frequency.

### Comparison

Differences between each method are illustrated in Fig. 5.5. As expected, due to $1/\sqrt{N}$ scaling of the error bar, the fitted frequency obtained using sum statistics or mean-corrected sum statistics is the same. However, the uncertainties differ widely. Since the sum statistics do not take into account shifting of the mean values as a function of the excitation frequency, the standard deviation and thus the individual errors will be large. In the case of sum statistics, $\chi^2/N$ is low, 0.26, which indicates that individual time-of-flight error bars are overestimated (see Fig. 5.5(b)). The individual statistics method works reasonably well though the $\chi^2/N$ of the fit is somewhat large, indicating slightly underestimated time-of-flight uncertainties (see Fig. 5.5(a)). The mean-corrected sum statistics works rather well and $\chi^2/N$ is relatively close to one (see Fig. 5.5(c)).

The distributions with and without the mean corrections are shown in Fig. 5.6. The distributions have enough ions so that the mean correction could be applied. The difference is clear: without the mean correction scattering is much larger due to fact that ions excited with resonance frequency have a naturally faster time of flight. The effect would be even more pronounced when the Ramsey excitation scheme is used since roughly half of the ions have a short time of flight (near resonance and within the sidebands) and the other half a long time of flight (baseline).

## 5.4 Countrate class analysis

It is known that different ion species stored simultaneously in the trap cause frequency shifts. This has been extensively studied for instance at ISOLTRAP [36, 86, 87]. In the countrate class analysis, the obtained data is split into a few smaller "countrate classes". That is, the data is separated according to how many ions per bunch were detected. Typically data is split into three parts (or more if the number of ions permits). For instance, the first part could consist of all bunches having 1–3 ions/bunch, the second part bunches with 4–5 ions per bunch and the third all bunches with 6–10 ions per bunch. The division is made such that about the same number of ions are included for each class. An example is shown in table 5.1 and in Fig. 5.7 for $\beta^+$-decaying $^{54}Co^+$ ions having $T_{1/2} \approx 200$ ms.

If there are not enough data to make a proper countrate class analysis, all of the data is used for just one single class. With two or more classes, the fitted frequencies are plotted as a function of the average number of ions per bunch. If there were

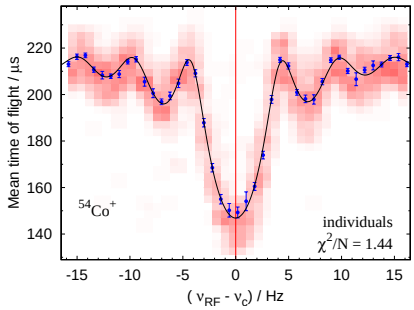


(a) Individuals: $\nu_c = 1991668.815(24)$ Hz.

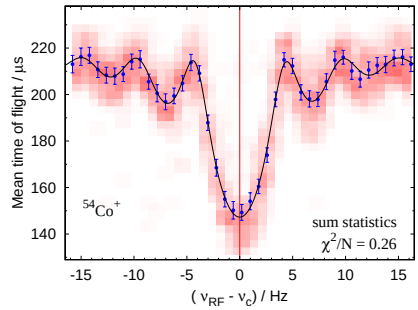


(b) Sum statistics: $\nu_c = 1991668.822(50)$ Hz.

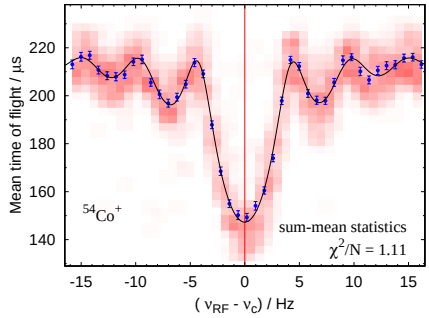


(c) Mean-corrected sum statistics: $\nu_c = 1991668.822(25)$ Hz.

**Figure 5.5:** Three methods for time-of-flight uncertainty determination. The time-of-flight uncertainties are not scaled with $\chi^2/N$ of the fit. Total number of ions in the spectrum was 1833 and an excitation time of 200 ms was used.

**Table 5.1:** A $^{54}$Co scan that has been analyzed by using the countrate class division. Data is fitted using the mean-corrected sum statistics. Results are plotted in Fig. 5.7.

| Class No. | ions/bunch | No. of ions | $\nu_c$ / Hz |
|---|---|---|---|
| 1 | 1 | 876 | 1991668.842(35) |
| 2 | 2 | 1341 | 1991668.912(58) |
| 3 | 3 | 1229 | 1991668.832(44) |
| 4 | 4–10 | 876 | 1991668.875(54) |
| Extrapolation to 0.6 ions/bunch | | | 1991668.847(45) |

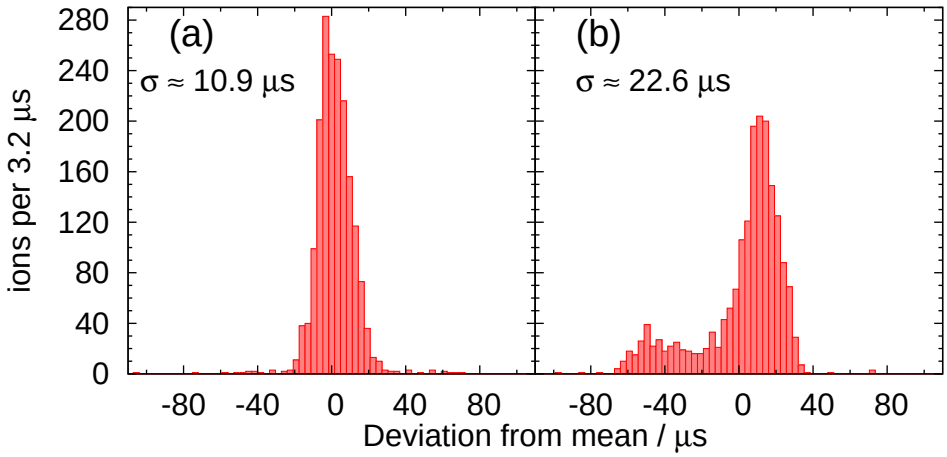


**Figure 5.6:** Distribution of ions around their mean time-of-flight value. The distribution on the left (a) is obtained with the mean correction while the distribution on the right (b), without.

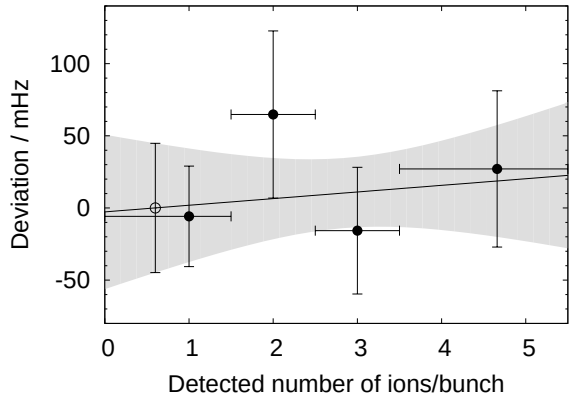


**Figure 5.7:** A scan of $^{54}$Co which has been analyzed using the countrate class analysis. The solid points are results of fitted data and the hollow point is the result of extrapolation to 0.6 ions/bunch, which corresponds to one ion/bunch when corrected with the detector efficiency of 60 %. The zero of the vertical axis is chosen as the extrapolated frequency (see table 5.1 for used data). The grey band shows one standard deviation around the fitted line used for extrapolation.

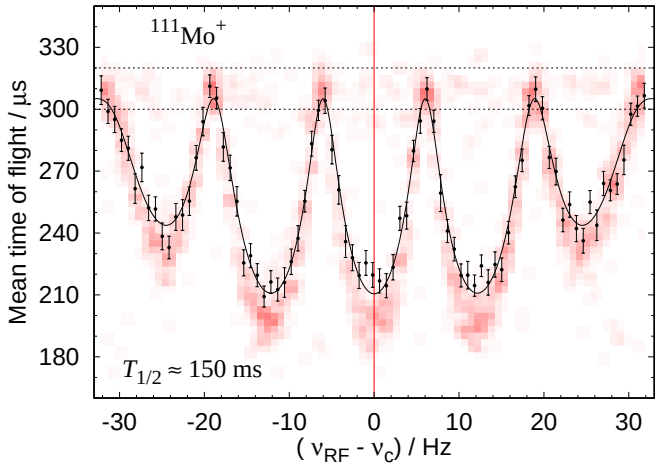


**Figure 5.8:** A time-of-flight resonance for $^{111}$Mo ($T_{1/2} \approx 150$ ms) measured in October 2008 with a Ramsey excitation pattern of (25-50-25) ms (On-Off-On). There are ions having a time of flight in the range of 300–320 $\mu$s independent of excitation frequency. The origin of the contamination is most probably due to inefficient cleaning in the purification trap. The dashed horizontal lines mark the time-of-flight range of ions without quadrupole excitation or that have cyclotron frequency far from the scan range.

contaminating ions, the frequency would shift as a function of ions per bunch. In the case described in table 5.1 and shown in Fig. 5.7, the slope (5±17 mHz/(ion/bunch)) is consistent with zero. Usually this is the case and as can be seen from the resonance quality (see for example Fig. 5.5), there are no contaminants. An example resonance with contaminants is shown in Fig. 5.8. Unfortunately the ion detection rate was too low to perform a proper countrate class analysis in order to see the shifting of the cyclotron frequency as a function of the number of contaminating ions. If the rate of ions allows one to do a countrate class analysis, it is performed and the obtained extrapolated frequency is used. In this manner, shifts due to contaminating ions are taken into account.

## 5.5 Frequency ratio determination

Having fitted every resonance — both the reference and the ion of interest scans — the next step is to determine the frequency ratio. Every measurement is performed

such that reference scans are interleaved with the scans of the "unknown" species. The interleaving is performed in order to take into account changes in the experimental conditions, including magnetic field fluctuations. For a single measurement consisting of a reference scan (at time $t_0$ having frequency $\nu_0$), an ion-of-interest scan (at time $t_1$ having frequency $\nu_{\mathrm{meas}}$) and a reference scan again (at $t_2$ with $\nu_2$), the interpolated reference ion frequency $\nu_{\mathrm{ref}}$ at the time of $\nu_{\mathrm{meas}}$ is

$$\nu_{\mathrm{ref}} = \frac{1}{t_2 - t_0}\left[\nu_0\left(t_2 - t_1\right) + \nu_2\left(t_1 - t_0\right)\right] \tag{5.12}$$

with uncertainty $\Delta\nu_{\mathrm{ref}}$

$$\Delta\nu_{\mathrm{ref}} = \frac{1}{t_2 - t_0}\sqrt{\left(t_2 - t_1\right)^2 \Delta\nu_0^2 + \left(t_1 - t_0\right)^2 \Delta\nu_2^2}. \tag{5.13}$$

After having both the interpolated reference frequency ($\nu_{\mathrm{ref}}$) and the frequency of the ion of interest ($\nu_{\mathrm{meas}}$), the frequency ratio $r$ is

$$r = \frac{\nu_{\mathrm{meas}}}{\nu_{\mathrm{ref}}} \tag{5.14}$$

with uncertainty

$$\Delta r = r\sqrt{\left(\frac{\Delta\nu_{\mathrm{ref}}}{\nu_{\mathrm{ref}}}\right)^2 + \left(\frac{\Delta\nu_{\mathrm{meas}}}{\nu_{\mathrm{meas}}}\right)^2}. \tag{5.15}$$

As there is usually more than one resonance of the ion of interest, the final frequency ratio is obtained by averaging over all individual frequency ratios. It should be noted that when calculating the frequency ratios from a chain of interleaved measurements (REF-MEAS-REF-...-MEAS-REF), the two consecutive scans of the ion of interest both depend on the same reference scan in between.

## 5.6 Magnetic field fluctuation

The interpolation procedure of the reference frequencies only accounts for a linear change of the magnetic field. Also additional fluctuations need to be considered. These fluctuations are studied by recording the cyclotron frequency of the same species for several days in order to see the temporal change of the cyclotron frequency. One such study was performed with stable $^{57}Fe^{+}$ ions from the IGISOL off-line ion source. Data were collected for 70 hours and separated afterwards to convenient 22 minute bins. A real measurement process was simulated by taking

three consecutive parts, the $n$th and the $(n+2)$th part as a reference and the intermediate, $(n+1)$, part as the ion of interest. The reference frequency is interpolated to the time of the intermediate file and the deviation of the magnetic field is obtained from the difference of the interpolated value and the measured one. The whole 70 hours of data is used to obtain the deviation. The deviations are binned and fitted with a Gaussian (see inset of Fig. 5.9). The standard deviation of the Gaussian is the "deviation of the deviations". This will result in the deviation when the time-difference of the ion-of-interest measurement from the reference measurements is 22 minutes.

Next, the same data is used so that the time between reference files is increased to 44 minutes, 66 minutes and so on. The "deviations of the deviations" are plotted as a function of time difference between the reference and ion-of-interest scans as shown in Fig. 5.9. The data is fitted with a straight line. The y-axis crossing of the fit ($9.2 \times 10^{-9}$) represents the statistical uncertainty of an individual file whereas the slope ($3.22(16) \times 10^{-11}$ min$^{-1}$) is interpreted as the magnetic field fluctuation on top of the linear drift. This number, multiplied by the time difference of the reference frequency measurements is added to the frequency ratio uncertainty. It should be noted that in most of the cases, the contribution from the magnetic field fluctuation to the final frequency ratio uncertainty is negligible unless the ion-of-interest frequency measurement extends for more than an hour. Even then it can be compensated by measuring the ion of interest several times in order to average out the magnetic field fluctuation term (see Ref. [88] for more details). As the JYFLTRAP magnet quenched in June 2007, the fluctuation had to be remeasured after the re-energization of the magnet. Prior to the quench (before June 2007), the fluctuation was $3.22(16) \times 10^{-11}$ min$^{-1}$ and it was measured to be $5.7(9) \times 10^{-11}$ min$^{-1}$ after the quench in November-December 2007.

## 5.7 Mass-dependent uncertainty

The misalignment of the magnetic and electric field axis or imperfections in the quadrupolar electric field causes shifts from the expected $\nu_c \propto \frac{1}{m}$ mass dependence. This effect is investigated by using very well known mass standards, usually carbon clusters or hydrocarbon compounds. An extensive study of the mass-dependent uncertainty has been carried out at ISOLTRAP [86] and at SHIPTRAP [89]. Since the SHIPTRAP magnet has quenched after the carbon cluster measurements by Chaudhuri *et al.* [89], the applicability of the results to the present re-energized system is not known since the alignment has certainly changed.

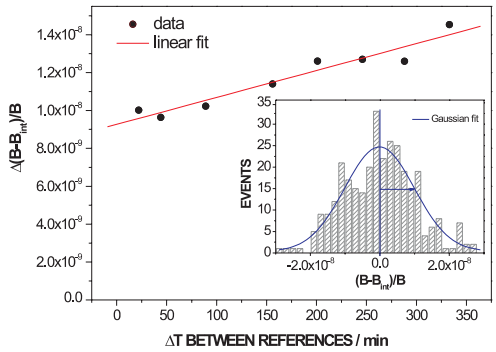


**Figure 5.9:** Deviation of the interpolated frequency from the measured frequency as a function of time difference between the reference scans. The offset of the fit represents the statistical uncertainty of an individual file and the slope gives the magnetic field fluctuation. This plot is from Ref. [88].

The mass dependent uncertainty to be added quadratically to the frequency ratio uncertainty at ISOLTRAP is (see Ref. [86])

$$\frac{u_{\mathrm{m}}(r)}{r} = 1.6 \times 10^{-10}/\mathrm{u} \times (m - m_{\mathrm{ref}}). \tag{5.16}$$

Although it would be possible to correct for the shift, it was decided to expand the uncertainties by that magnitude. In addition to the mass-dependent uncertainty, a residual systematic uncertainty was derived from the same data. On top of the mass-dependent uncertainty, an absolute, residual uncertainty of $\Delta r/r = 8 \times 10^{-9}$ is added. These two uncertainties added on top of the statistical one (including magnetic field fluctuation) fully satisfied the data given in Ref. [86] with normalized $\chi^2$ of 1. This also implies that any frequency ratio measurement performed at ISOLTRAP can not reach better precision than $\Delta r/r = 8 \times 10^{-9}$.

At SHIPTRAP, the carbon cluster measurements did not reveal any mass-dependent offsets but a systematic uncertainty of $4.5 \times 10^{-8}$ was discovered [89].

At JYFLTRAP, the carbon cluster studies [90] have been performed and results are expected to be published soon [91]. For the time being, a mass-dependent uncertainty of

$$\frac{u_{\mathrm{m}}(r)}{r} = 7 \times 10^{-10}/\mathrm{u} \times (m - m_{\mathrm{ref}}) \tag{5.17}$$

has been used which was derived from the mass difference of singly charged $O_2$ molecule and $^{132}$Xe (see Ref. [92] for more details).

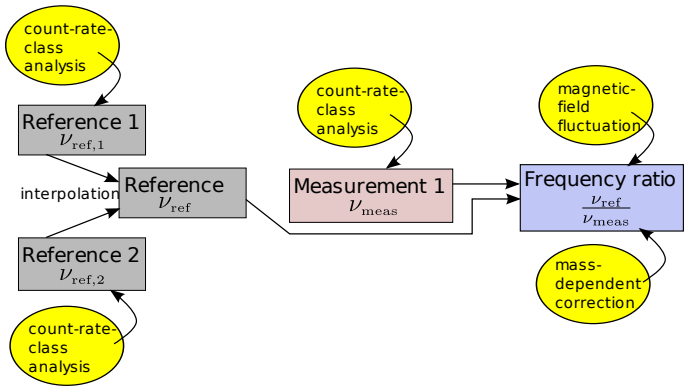


**Figure 5.10:** Determination of a single frequency ratio using two reference ion scans and an ion-of-interest scan. The countrate class analysis is performed for each scan. The magnetic field fluctuation is added to the frequency ratio and if mass-dependent correction is available, it should also be applied to the frequency ratio at this stage.

## 5.8 Analysis summary

The analysis steps are summarized in Fig. 5.10, in which the simplest case is shown where two reference frequency scans and one ion-of-interest scan is used to determine a frequency ratio. The countrate class analysis is performed for each scan and the final result is used for further calculations. The magnetic field fluctuation is added only to the frequency ratio as well as the mass-dependent correction.

Typically, at least 3 different ion-of-interest scans are recorded and the final frequency ratio is the weighted average of the individual frequency ratios as shown in Fig. 5.10. Both the inner and outer errors are calculated to obtain the Birge ratio [93]. If both the inner error

$$\sigma_{\mathrm{int}}^2 = \frac{1}{\sum_i \frac{1}{\sigma_i^2}} \tag{5.18}$$

and the outer error

$$\sigma_{\mathrm{ext}}^2 = \frac{\sum_i \frac{1}{\sigma_i^2} (r_i - \overline{r})^2}{(n-1) \sum_i \frac{1}{\sigma_i^2}} \tag{5.19}$$

are about equal, the fluctuation around the mean value is purely statistical. Common practise has been that if either of the error is larger, then the larger one is used as the final error. If the mass-dependent shift was not corrected for before, the error is

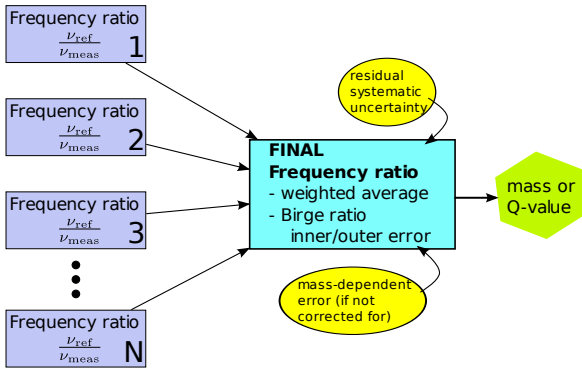


**Figure 5.11:** Determination of the final frequency ratio. Using $N$ individual frequency ratios (as shown in Fig. 5.10) the final frequency ratio is obtained by calculating the weighted average of the individual values. The inner and outer errors are calculated. The residual systematic uncertainty is then added at the very end.

added now in this stage. Also, the final residual systematic uncertainty is added in this stage. It should be noted that the statistical uncertainty will go down if more frequency ratio measurements are performed. However, the systematic errors — the mass-dependent and the residual — are added at the very end since those determine the very limits of the experimental setup and thus can not be averaged out.

## 5.9 Mass determination

The data analysis produces frequency ratios. The mass or $Q_{\mathrm{EC}}$ value is easily derived from those when the mass of the reference is well-known. If the reference ion has a mass $m_{\mathrm{ref}}$ and charge $q_{\mathrm{ref}}$ and the "unknown" ion had charge $q_{\mathrm{meas}}$, the mass of the unknown $m_{\mathrm{meas}}$ is

$$m_{\mathrm{meas}} = r \times (m_{\mathrm{ref}} - q_{\mathrm{ref}} m_e + B_{\mathrm{ref}}) + q_{\mathrm{meas}} m_e - B_{\mathrm{meas}}, \tag{5.20}$$

where $m_e$ is the mass of an electron and $r$ the measured cyclotron frequency ratio $\frac{\nu_{c,\mathrm{ref}}}{\nu_{c,\mathrm{meas}}}$. $m_{\mathrm{ref}}$ and $m_{\mathrm{meas}}$ are the *atomic* masses of the reference and the unknown, respectively. $B_i$ is the sum of the atomic binding energies of the missing electrons. So far only singly- or doubly-charged ions have been used and atomic binding energies are still negligible in the level of precision obtained in current studies. For singly charged ions Eq. (5.20) simplifies to (neglecting atomic electron binding energies)

$$m_{\mathrm{meas}} = r \times (m_{\mathrm{ref}} - m_e) + m_e \tag{5.21}$$

with an uncertainty (neglecting the uncertainty in $m_e$)

$$\Delta\left(m_{\mathrm{meas}}\right) = \sqrt{(\Delta r)^2 (m_{\mathrm{ref}})^2 + (\Delta m_{\mathrm{ref}})^2 r^2}. \tag{5.22}$$

A mass value can never be more accurate than the reference mass value.

## 5.10 $Q_{EC}$ value determination

A special case of mass determination is the $Q_{\mathrm{EC}}$ value determination. Effectively, the $Q_{\mathrm{EC}}$ value is the mass difference between mother ("unknown") and daughter ("reference") atoms

$$Q_{\mathrm{EC}} = m_{\mathrm{mother}} - m_{\mathrm{daughter}} = [r-1]\left(m_{\mathrm{daughter}} - m_e\right). \tag{5.23}$$

As the mother and daughter are mass doublets having the same $A/q$, the frequency ratio is very close to one and thus the term inside the square brackets, $r-1$, is on the order of $10^{-3}$. Thus, the contribution from the uncertainty of the reference mass is negligible. What is also convenient with mass doublets is that the mass-dependent error is negligible due to the small difference in their cyclotron frequencies. The uncertainty of a $Q_{\mathrm{EC}}$ value is mainly due to the uncertainty in the frequency ratio

$$\begin{aligned} \Delta Q_{\mathrm{EC}} &= \sqrt{(\Delta r)^2 (m_{\mathrm{daughter}} - m_e)^2 + (\Delta m_{\mathrm{daughter}})^2 (r-1)^2} \\ &\approx \Delta r \times (m_{\mathrm{daughter}} - m_e). \end{aligned} \tag{5.24}$$

# 6 Results and discussion

For this thesis work, several $Q_{\mathrm{EC}}$ values of superallowed $\beta$ emitters with $T = 1$ were measured with high precision. As the IGISOL could in each case provide not only the ion-of-interest (parent) nuclei but also the reference (daughter) nuclei simultaneously as an ion beam, the measurement is performed as a mass doublet measurement by interleaving frequency measurements of daughter and mother nuclei.

The results presented here include $Q_{\mathrm{EC}}$ values of $^{26}\mathrm{Al}^{m}$, $^{26}$Si, $^{42}$Sc, $^{46}$V, $^{50}$Mn, $^{54}$Co and $^{62}$Ga. Also the $Q_{\mathrm{EC}}$ value of $^{42}$Ti was measured and the data had been analyzed. The result will be published in a joint article which will also include superallowed branching ratio and half-life measurement results also measured at JYFLTRAP. All of the nuclei were produced using the light-ion fusion guide. The parent nuclei were produced with (p,$x$n) reactions with the exception of $^{42}$Sc and $^{42}$Ti which were produced with $^{40}$Ca($^{3}$He,p)$^{42}$Sc or $^{40}$Ca($^{3}$He,n)$^{42}$Ti reactions. The yields of these ions were relatively high and in most of the cases the ideal number of 1 to 3 ions/bunch could be reached. A summary of all superallowed emitters and the other states relevant for the present study are tabulated in table 6.1.

The first $Q_{\mathrm{EC}}$ value measurement at JYFLTRAP was performed in 2005 when the $Q_{\mathrm{EC}}$ value of $^{62}$Ga was measured [95]. By the time of the measurement, the other experimental quantities ($t_{1/2}$ and branching ratio) needed for the $\mathcal{F}t$ value determination were already rather well known so that the improved $Q_{\mathrm{EC}}$ value would bring the precision of the $\mathcal{F}t$ value to a comparable level with the other well known $\mathcal{F}t$ values [1].

The $Q_{\mathrm{EC}}$ value result of $^{46}$V from the Canadian Penning trap [96] was controversial. Their value was about $2.5\sigma$ higher than the previously adopted value in the 2005 Hardy & Towner compilation [1]. A similar offset was later measured also at JYFLTRAP in 2006 [97]. To confirm if such large offsets would be present in other well known superallowed emitters, two accurate $Q_{\mathrm{EC}}$ values were chosen to be remeasured at JYFLTRAP. The two, $^{26}\mathrm{Al}^{m}$ and $^{42}$Sc, were also measured in 2006 [97]. No large $Q_{\mathrm{EC}}$ value deviation was found in the two nuclei but clearly there was a need to confirm the $Q_{\mathrm{EC}}$ values of the other well known superallowed $\beta$ emitters by Penning trap technique since many $Q_{\mathrm{EC}}$ values originate from the same data set as

**Table 6.1:** The superallowed $\beta$ emitters having isospin $T = 1$ studied in this work. The half-life of the parent and daughter states and the superallowed branching ratio are given. The values are from Ref. [1] except $^{62}$Ga from Ref. [94] and $^{26}$Si from Ref. [78].

| Parent | $T_z$ | $T_{1/2}$ (ms) | $BR$ (%) | Daughter | $T_{1/2}$ |
|---|---|---|---|---|---|
| $^{26}$Al$^m$ | 0 | $6345.0 \pm 1.9$ | $100.000^{+0}_{-0.003}$ | $^{26}$Mg | stable |
| $^{42}$Sc | 0 | $680.72 \pm 0.26$ | $99.9941 \pm 0.0014$ | $^{42}$Ca | stable |
| $^{46}$V | 0 | $422.50 \pm 0.11$ | $99.9848^{+0.0013}_{-0.042}$ | $^{46}$Ti | stable |
| $^{50}$Mn | 0 | $283.24 \pm 0.13$ | $99.9423 \pm 0.0030$ | $^{50}$Cr | stable |
| $^{54}$Co | 0 | $193.271 \pm 0.063$ | $99.9955^{+0.0006}_{-0.0300}$ | $^{54}$Co | stable |
| $^{62}$Ga | 0 | $116.121 \pm 0.021$ | $99.858 \pm 0.008$ | $^{62}$Zn | 9.13 h |
| $^{26}$Si | $-1$ | $2228.8 \pm 2.6$ | $75.48 \pm 0.58$ | $^{26}$Al$^m$ | 6.345 s |

$^{46}$V, namely the reaction-based measurements by Vonach *et al.* [98]. They measured $Q$ values using ($^3$He,t) reactions by means of the precision time-of-flight measuring system and Q3D spectrograph at the Munich Tandem laboratory.

The next cases studied at JYFLTRAP were $^{26}$Si and $^{42}$Ti. These $Q_{\mathrm{EC}}$ values were measured in September 2006. Both of these are $T_z = -1$ nuclei. More than a ten-fold improvement in the $Q_{\mathrm{EC}}$ values was obtained. The half-life and branching ratio have also been measured using JYFLTRAP as a high-resolution mass filter. The branching ratio and half-life results of $^{26}$Si have been recently published [78] while the $Q_{\mathrm{EC}}$ value has been submitted for publication. Although all experimental quantities were improved for $^{26}$Si, the precision of the $\mathcal{F}t$ value is not quite good enough for $^{26}$Si to contribute to testing of the Standard Model. The half-life and branching ratio of $^{42}$Ti have been measured at JYFLTRAP by the same group that measured $^{26}$Si. An article which will include all experimental results — $T_{1/2}$, $Q_{\mathrm{EC}}$ and branching ratio — is in preparation.

To continue verifying the well known superallowed $\beta$ emitters, the $Q_{\mathrm{EC}}$ values of $^{50}$Mn and $^{54}$Co were measured in December 2006 and in May 2007 [99]. Both of these cases have isomers at about 200 keV excitation energy. In order to remove those the Ramsey cleaning method (see section 4.4) was used. Also in the May 2007 beamtime, the Ramsey method was used for time-of-flight ion-cyclotron resonances which enhanced the obtained precision. Excitation times were limited due to short half-lives of the studied ions. The resulting $Q_{\mathrm{EC}}$ values and thus $\mathcal{F}t$ values of $^{50}$Mn and $^{54}$Co were off compared to the Hardy and Towner compilation [1] by a similar

**Table 6.2:** Comparison of JYFLTRAP $Q_{\mathrm{EC}}$ values to values given in the 2005 Hardy & Towner compilation [1]. The difference ($\Delta Q_{\mathrm{EC}}$) between JYFLTRAP and Ref. [1] values are given and also how many days of beamtime was used to measure the transition.

| Parent | $T_z$ | Daughter | JYFL (keV) | [1] (keV) | $\Delta Q_{\mathrm{EC}}$ (keV) | days |
|---|---|---|---|---|---|---|
| $^{26}\mathrm{Al}^m$ | 0 | $^{26}\mathrm{Mg}$ | 4232.83(13) | 4232.55(17) | 0.28(21) | 3 |
| $^{42}\mathrm{Sc}$ | 0 | $^{42}\mathrm{Ca}$ | 6426.13(21) | 6425.63(38) | 0.50(43) | 3 |
| $^{46}\mathrm{V}$ | 0 | $^{46}\mathrm{Ti}$ | 7052.72(31) | 7050.71(89) | 2.01(94) | 2 |
| $^{50}\mathrm{Mn}$ | 0 | $^{50}\mathrm{Cr}$ | 7634.48(7) | 7632.43(23) | 2.05(24) | 6 |
| $^{54}\mathrm{Co}$ | 0 | $^{54}\mathrm{Co}$ | 8244.54(10) | 8242.60(29) | 1.94(31) | 6 |
| $^{62}\mathrm{Ga}$ | 0 | $^{62}\mathrm{Zn}$ | 9181.07(54) | 9171(26) | 10(26) | 3 |
| $^{26}\mathrm{Si}$ | $-1$ | $^{26}\mathrm{Al}^m$ | 4840.85(10) | 4836.9(30) | 4(3) | 3 |

amount than that of the $^{46}$V case. By the time of publishing [99], Towner and Hardy had re-evaluated the theoretical corrections [12]. The $\mathcal{F}t$ value of $^{46}$V was not anymore anomalously higher than the others but was shifted down. Also the $^{50}$Mn and $^{54}$Co $\mathcal{F}t$ values were shifted down compared to the earlier compilation [1]. The main change in the theoretical shell-model calculations of the isospin mixing correction $\delta_C$ by Towner and Hardy was opening of the core orbitals in the core nucleus of $^{40}$Ca. As a consequence, the $\mathcal{F}t$ values of heavier ($A \geq 40$) nuclei increased while the $\mathcal{F}t$ values of lighter nuclei did not change much. When using the new corrections from Ref. [12] and the new $Q_{\mathrm{EC}}$ values from Refs. [96, 97, 99] the world average $\mathcal{F}t$ value is again consistent with all of the individual $\mathcal{F}t$ values.

Figure 6.1 shows a part of the chart of nuclei, where superallowed isospin $T = 1$ emitters having $A \leq 74$ are indicated. The JYFLTRAP contribution to improving the $Q_{\mathrm{EC}}$ values is significant. The work will continue at JYFLTRAP to measure the lightest well known cases $^{10}$C, $^{14}$O, $^{34}$Cl and $^{38}\mathrm{K}^m$. Since the $^{34}$Cl and $^{38}\mathrm{K}^m$ cases have low-lying isomeric states, the Ramsey cleaning method need to be used in these cases. The lighter cases $^{10}$C and $^{14}$O will be otherwise problematic due to contaminating stable-ion beams from IGISOL. For example, stable nitrogen at mass number 14 will be several orders of magnitude more intense than the radioactive $^{14}$O beam. Therefore, particular attention to production method will be required.

The $Q_{\mathrm{EC}}$ values measured at JYFLTRAP are summarized in table 6.2. Also, the previously adopted $Q_{\mathrm{EC}}$ values in Ref. [1] are given with the deviation from the JYFLTRAP values.

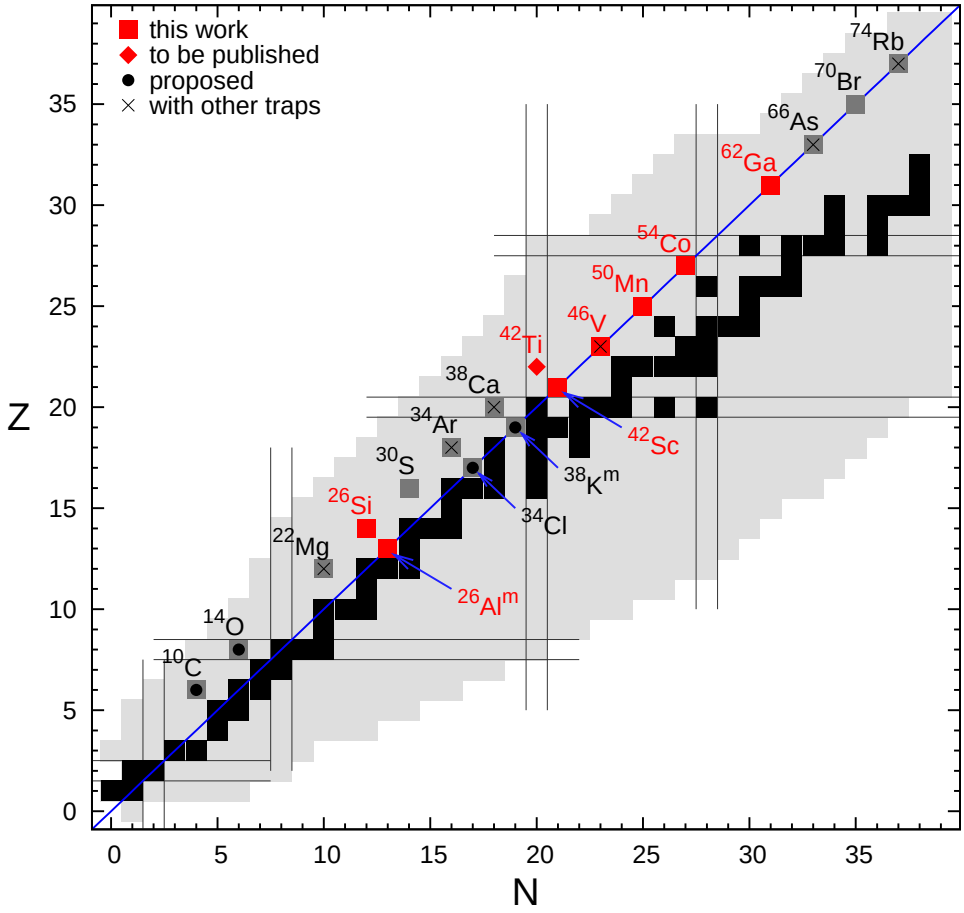


**Figure 6.1:** Most of the superallowed $\beta$ emitters having $A \leq 74$ (marked with dark gray). The $Q_{\mathrm{EC}}$-values of the nuclides marked with red squares have been measured in this work. The mass excess (or the $Q_{\mathrm{EC}}$ value in the case of $^{46}$V) of nuclei marked with a cross has been measured with other Penning trap facilities. An accepted proposal to measure the $Q_{\mathrm{EC}}$ values of nuclei are indicated with filled circles.

## 6.1 $Q_{\mathrm{EC}}$ values from other trap experiments

There are several contributions to the superallowed $\beta$ decay studies from other Penning trap facilities. The mass excess values of $T_z = -1$ emitters $^{22}$Mg, $^{34}$Ar and $^{74}$Rb have been measured with ISOLTRAP [100, 101]. $^{22}$Mg has also been measured with the Canadian Penning trap [102]. The mass of the $T_z = -1$ emitter $^{38}$Ca has been measured at LEBIT [103] and also at ISOLTRAP [47]. The mass of the $T_z = 0$ emitter $^{66}$As has been measured at LEBIT [104]. All these experiments have determined the $Q_{\mathrm{EC}}$ value by measuring the absolute mass of the emitter and by using the absolute mass value of the daughter from other source the $Q_{\mathrm{EC}}$ value is obtained. In the case of $^{74}$Rb, the mass of the daughter, $^{74}$Kr, was measured at ISOLTRAP also. The only experiment — in addition to JYFLTRAP experiments — that has directly determined the $Q_{\mathrm{EC}}$ value is the $^{46}$V experiment by Savard *et al.* [96].

## 6.2 Isomeric states

Several $T_z = 0$ nuclei have isomeric states with very long ($>$ seconds) half-lives. These often pose a difficulty in Penning trap mass spectroscopy since if the measurement is performed with a mixed sample of two different states, the obtained frequency is shifted. On the other hand, if the states can be separated, the superallowed $Q_{\mathrm{EC}}$ values can also be determined using the high-spin states. In this work, the $Q_{\mathrm{EC}}$ values of $^{26}$Al$^m$, $^{26}$Si, $^{42}$Sc, $^{50}$Mn and $^{54}$Co were, in addition to a direct measurement, also determined via the high-spin state. These are summarized in table 6.3. Additionally, the cyclotron frequency differences between the states for singly-charged ions in $\approx 7$ T magnetic field are given. With the purification trap it is possible to obtain a resolution of about 8 Hz but with rather poor transmission. It is more efficient to make the purification trap resolution worse (and therefore improve the transmission) and to perform isomeric cleaning in the precision trap as described in section 4.4. For reference, isomeric states in the superallowed $\beta$ emitters $^{34}$Cl and $^{38}$K$^m$ are given.

**Table 6.3:** Isomeric and ground states states of $T_z = 0$ nuclei relevant for the current study. Given are the excitation energy in keV and cyclotron frequency difference for singly-charged ions in 7 T magnetic field. The $J^\pi = 0^+$ states are given in boldface.

| State | $J^\pi$ | $T_{1/2}$ | $\Delta E$ (keV) | $\Delta\nu_c$ (Hz) |
|---|---|---|---|---|
| $^{26}$Al | $5^+$ | 717 ky | 228.305(13) | $\sim 40$ |
| $^{26}\mathbf{Al}^m$ | $0^+$ | 6.35 s | | |
| $^{34}\mathbf{Cl}$ | $0^+$ | 1.53 s | 146.36(3) | $\sim 15$ |
| $^{34}$Cl$^m$ | $3^+$ | 32.0 min | | |
| $^{38}$K | $3^+$ | 7.64 min | 130.50(28) | $\sim 10$ |
| $^{38}\mathbf{K}^m$ | $0^+$ | 924 ms | | |
| $^{42}\mathbf{Sc}$ | $0^+$ | 681 ms | 616.62(24) | $\sim 40$ |
| $^{42}$Sc$^m$ | $(5-7)^+$ | 61.7 s | | |
| $^{46}\mathbf{V}$ | $0^+$ | 423 ms | - | - |
| $^{50}\mathbf{Mn}$ | $0^+$ | 283 ms | 225.28(9) | $\sim 9$ |
| $^{50}$Mn$^m$ | $5^+$ | 1.75 min | | |
| $^{54}\mathbf{Co}$ | $0^+$ | 193 ms | 197.64(13) | $\sim 7$ |
| $^{54}$Co$^m$ | $(7)^+$ | 1.48 min | | |

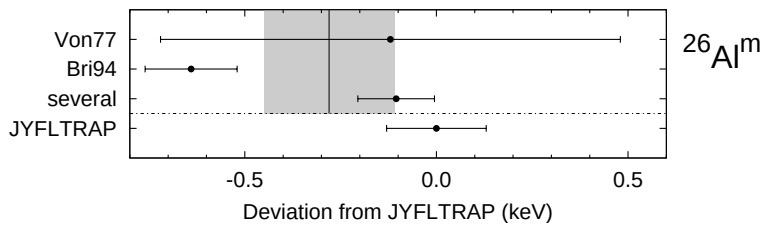


**Figure 6.2:** The $Q_{\mathrm{EC}}$ value measurements of $^{26}\mathrm{Al}^{m}$. Plotted is the deviation to the JYFLTRAP measurement for each reference. The vertical bar denotes the adopted value in Ref. [1] with one standard deviation (shaded); the points below the dashed horizontal line are newer and not included in the average. Von77: Vonach *et al.* [98], Bri94: Brindhaban *et al.* [107] and several: see Ref. [1] for references.

## 6.3 Discussion

### 6.3.1 $^{26}\mathrm{Al}^{m}$

Prior to the JYFLTRAP measurements of $^{26}\mathrm{Al}^{m}$ there had been several high-precision $Q_{\mathrm{EC}}$ value measurements (see Ref. [1] for references). The excitation energy of the $0^{+}$ isomeric state is also well known [105]. The final adopted $Q_{\mathrm{EC}}$ value of $^{26}\mathrm{Al}^{m}$ is not only composed of direct measurements but also from measurements of $Q_{\mathrm{EC}}$ value differences (see Ref. [106], for instance). The different measurements are shown in Fig. 6.2. The JYFLTRAP value is in excellent agreement with all previous values except with the value from Ref. [107]. The motivation to measure the $Q_{\mathrm{EC}}$ value of the already accurately known superallowed $\beta$ emitter $^{26}\mathrm{Al}^{m}$ was to clarify whether Penning trap mass measurements in general have an offset to the reaction-based $Q$-value measurements, since $^{46}\mathrm{V}$ had a large deviation. Clearly the JYFLTRAP and the reaction-based measurements agree in this case.

### 6.3.2 $^{42}\mathrm{Sc}$

The $Q_{\mathrm{EC}}$ value was measured for the same reason as $^{26}\mathrm{Al}^{m}$ — to clarify whether a deviation of the same magnitude as in $^{46}\mathrm{V}$ would be present in the case of $^{42}\mathrm{Sc}$. The different $Q_{\mathrm{EC}}$ values are plotted in Fig. 6.3. Here, the $Q_{\mathrm{EC}}$ value by Vonach *et al.* is off by about 2 keV from the JYFLTRAP value. The adopted value in Ref. [1] does not have much weight from the Vonach value. Nevertheless a scaling factor of 3.2 had to be used in order to make the weighted average of the two discrepant values

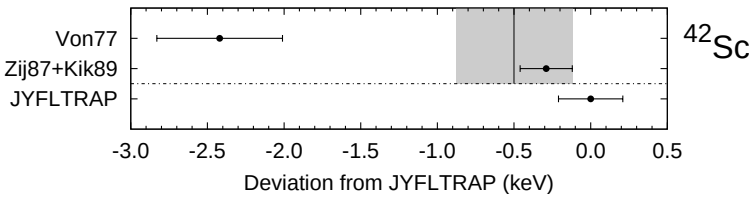


**Figure 6.3:** The $Q_{\mathrm{EC}}$ value measurements of $^{42}$Sc. Plotted is the deviation to the JYFLTRAP measurement for each reference. The vertical bar denotes the adopted value in Ref. [1] with one standard deviation (shaded); the points below the dashed horizontal line are newer and not included in the average. Von77: Vonach *et al.* [98], Zij87+Kik89: Zijderhand *et al.* [108] and Kikstra *et al.* [109].

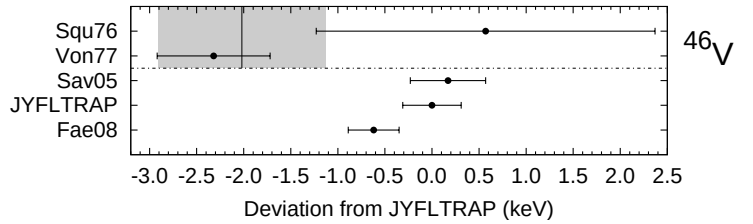


**Figure 6.4:** The $Q_{\mathrm{EC}}$ value measurements of $^{46}$V. Plotted is the deviation to the JYFLTRAP measurement for each reference. The vertical bar denotes the adopted value in Ref. [1] with one standard deviation (shaded); the points below the dashed horizontal line are newer and not included in the average. Squ76: Squier *et al.* [112], Von77: Vonach *et al.* [98], Sav05: Savard *et al.* [96] and Fae08: Faestermann *et al.* [113].

to be statistically consistent.

It should also be noted that the excitation energy of the isomeric state was also measured at JYFLTRAP [97]. The excitation energy from JYFLTRAP, 616.62(24) keV, is somewhat higher than the energy obtained from gamma spectroscopy measurements, 616.28(6) keV [110]. There has been a new measurement of the excitation energy which seems to agree better with the JYFLTRAP result rather than with the older one [111].

### 6.3.3 $^{46}$V

A remeasurement of the $Q_{\mathrm{EC}}$ value first by Savard *et al.* [96] and later at JYFLTRAP [97] revealed a large discrepancy to the $Q_{\mathrm{EC}}$ value measured by Vonach *et al.* [98].

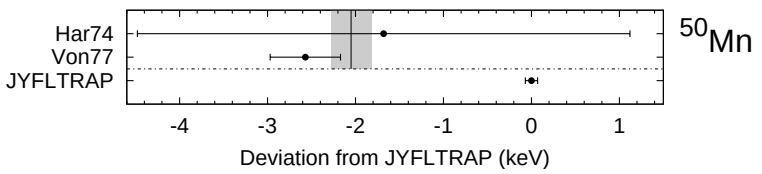


**Figure 6.5:** The $Q_{\mathrm{EC}}$ value measurements of $^{50}$Mn. Plotted is the deviation to the JYFLTRAP measurement for each reference. The vertical bar denotes the adopted value in Ref. [1] with one standard deviation (shaded); the points below the dashed horizontal line are newer and not included in the average. Har74: Hardy *et al.* [114] and Von77: Vonach *et al.* [98].

Just recently, the $Q_{\mathrm{EC}}$ value of $^{46}$V was remeasured using essentially the same experimental conditions as Vonach *et al.* [98]. Instead of calibrating the ion energies with over 100 m long time-of-flight system, the same reaction was used on another titanium isotope within the same target for calibration [113]. The new result deviates from the older reaction measurement and is much closer to the Penning trap results. The different $Q_{\mathrm{EC}}$ values are plotted in Fig. 6.4.

### 6.3.4 $^{50}$Mn and $^{54}$Co

The $Q_{\mathrm{EC}}$ values for these emitters were measured during the same beam time periods [99]. The cases are very similar since both are rather short-lived ($T_{1/2} \approx 200$ ms) and have close-lying isomeric states at $\approx 200$ keV excitation energy. The isomeric (or the ground state) was removed using the Ramsey cleaning method (see sec. 4.4). Also, the time-of-flight ion-cyclotron resonances were obtained using the Ramsey excitation method. The results are compared to the old measurements in Figs. 6.5 and 6.6.

In both cases the results in Ref. [98] deviate by about 2 keV from the the JYFLTRAP values. It should be noted that the difference of the $Q_{\mathrm{EC}}$ values of $^{50}$Mn and $^{54}$Co is 610.06(12) keV, which is in fine agreement with the value of 610.1(5) keV reported in Ref. [106]. On the other hand the $Q_{\mathrm{EC}}$ value difference between $^{42}$Sc and $^{54}$Co calculated from the JYFLTRAP data deviates by 1.2(3) keV from the value given in Ref. [106].

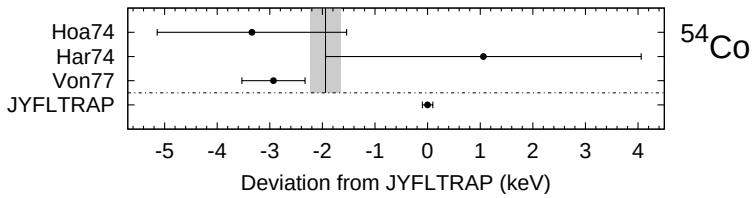


**Figure 6.6:** The $Q_{\mathrm{EC}}$ value measurements of $^{54}$Co. Plotted is the deviation to the JYFLTRAP measurement for each reference. The vertical bar denotes the adopted value in Ref. [1] with one standard deviation (shaded); the points below the dashed horizontal line are newer and not included in the average. Hoa74: Hoath *et al.* [115], Har74: Hardy *et al.* [114] and Von77: Vonach *et al.* [98].

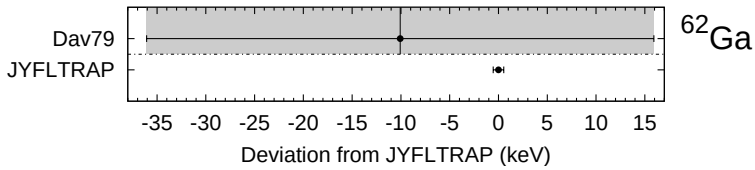


**Figure 6.7:** The $Q_{\mathrm{EC}}$ value measurements of $^{62}$Ga. Plotted is the deviation to the JYFLTRAP measurement. Dav79: Davids *et al.* [116].

### 6.3.5 $^{62}$Ga

The first superallowed $Q_{\mathrm{EC}}$ value measured at JYFLTRAP was $^{62}$Ga [97]. Before the JYFLTRAP measurement only one measurement existed with a modest, 27 keV uncertainty on the $Q_{\mathrm{EC}}$ value [116]. The JYFLTRAP measurement pushed the uncertainty down to a level that enabled $^{62}$Ga to contribute to the derivation of $V_{\mathrm{ud}}$. The two measurements are plotted in Fig. 6.7.

### 6.3.6 $^{26}$Si

Not only the $Q_{\mathrm{EC}}$ value [117] but also the half-life and the branching ratio of $^{26}$Si were determined [78] at JYFLTRAP. Combined, these measurements improved dramatically the $\mathcal{F}t$ value of $^{26}$Si although the branching ratio has still to be improved in order that $^{26}$Si may contribute to the world average $\mathcal{F}t$ value.

Since the compilation by Hardy and Towner [1], one new mass measurement for $^{26}$Si has been performed using (p,t) reactions [118] before the JYFLTRAP $Q_{\mathrm{EC}}$ value measurement. The results are plotted in Fig. 6.8.

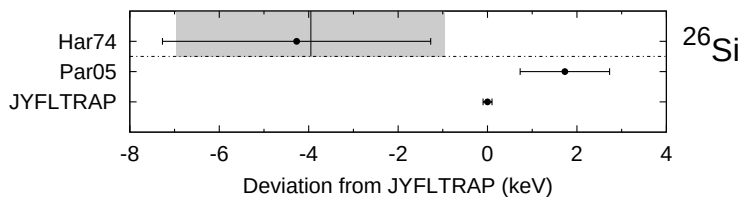


**Figure 6.8:** The $Q_{\mathrm{EC}}$ value measurements of $^{26}$Si. Plotted is the deviation to the JYFLTRAP measurement for each reference. The vertical bar denotes the adopted value in Ref. [1] with one standard deviation (shaded); the points below the dashed horizontal line are newer and not included in the average. Har74: Hardy *et al.* [119] and Par05: Parikh *et al.* [118].

## 6.4 $\mathcal{F}t$-values

The latest compilation of the $\mathcal{F}t$ values from the superallowed $T = 1$ $\beta$ decays by Towner and Hardy [12] updates the previous compilation [1]. Not only were new experimental data included but also a re-evaluation of the theoretical corrections. The reason for the re-evaluation was primarily due to the controversial results of $^{46}$V $Q_{\mathrm{EC}}$ values [96,97], and in part due to the new values of $^{50}$Mn and $^{54}$Co.

To see the effect of the new experimental data that has been published since the 2005 evaluation [1], the $\mathcal{F}t$ values using $ft$ values from Ref. [1] but corrections from Ref. [12] are plotted among the recent $ft$ values in Fig. 6.9. The recent results are from Ref. [12] have been added with the branching ratio of $^{62}$Ga [94], half-life of $^{10}$C [120], branching ratio of $^{38}$K$^{m}$ [121] and the half-life and the branching ratio of $^{26}$Si [78]. Additionally, the JYFLTRAP $Q_{\mathrm{EC}}$ values of $^{26}$Si [117], $^{50}$Mn and $^{54}$Co [99] have been included. The $Q_{\mathrm{EC}}$ values of $^{26}$Al$^{m}$, $^{42}$Sc, $^{46}$V and $^{62}$Ga are already included in Ref. [12]. Using these data, the world average is $\overline{\mathcal{F}t} = 3072.2(8)$ s.

## 6.5 Unitarity of the CKM matrix

The $V_{\mathrm{ud}}$ element of the Cabibbo-Kobayashi-Maskawa quark-mixing matrix can be calculated from the world average $\overline{\mathcal{F}t}$ value using Eq. (2.31)

$$V_{\mathrm{ud}}^2 = \frac{K}{2G_F^2(1+\Delta_R^V)\overline{\mathcal{F}t}}, \tag{6.1}$$

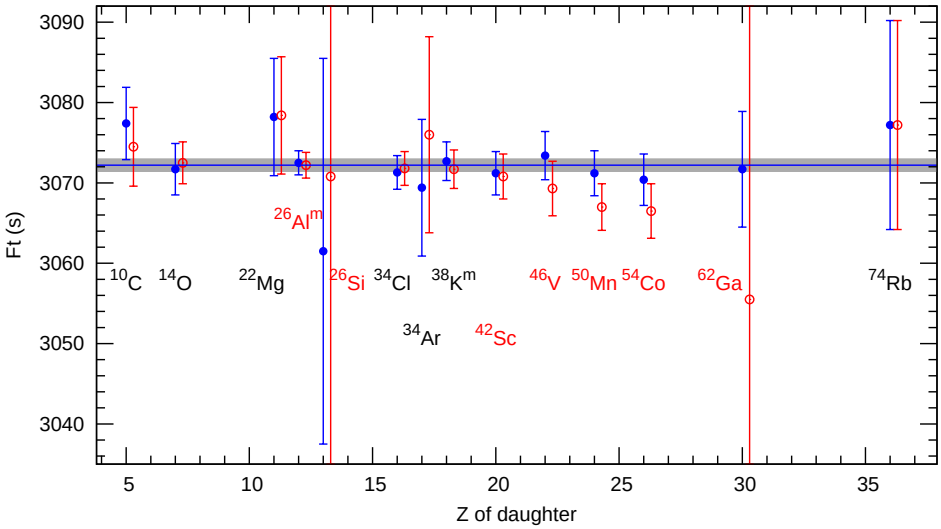


**Figure 6.9:** $\mathcal{F}t$ values of the most precisely known superallowed $T = 1$ $\beta$ emitters. The solid blue circles are the $\mathcal{F}t$ values from Ref. [12] with updated results that have been published since the publication of the compilation. The empty red circles are plotted using $ft$ values from Ref. [1] while using theoretical corrections from Ref. [12]. The points labelled with red color have contribution from JYFLTRAP.

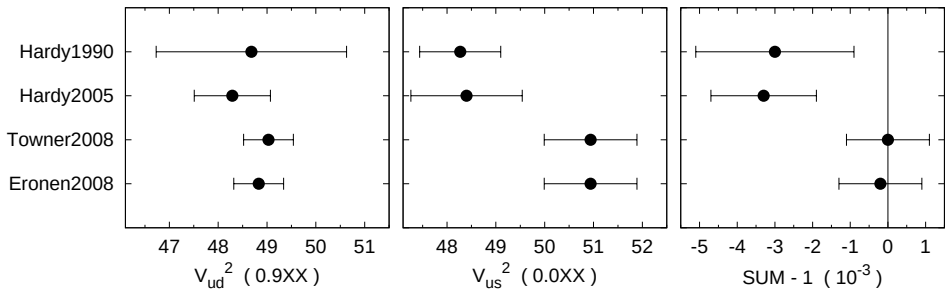


**Figure 6.10:** Change in $V_{ud}^2$, $V_{us}^2$ and in the unitarity sum. $V_{ud}^2$ has significantly improved during the recent years. Controversial experiments in the determination of $V_{us}^2$ has resulted in a significant change in the value between the two evaluation by Hardy and Towner. Hardy1990: Hardy *et al.* [122], Hardy2005: Hardy and Towner [1], Towner2008: Towner and Hardy [12], Eronen2008: Eronen *et al.* [99].

where $G_F = 1.16637(1) \times 10^{-5}$ GeV$^{-2}$ [21], the inner radiative correction $\Delta_R^V = 2.361(38)$ % and $K/(\hbar c)^6 = 8120.278(4) \times 10^{-10}$ GeV$^{-4}$s. The $\overline{\mathcal{F}t}$ value is increased by 0.85(85) s to take into account possible systematic errors in the calculation of $\delta_C$ (see Ref. [12] for more details).

Using the latest $\mathcal{F}t$ for $^{50}$Mn and $^{54}$Co from Ref. [99] and for the 11 others from Ref. [12], the $|V_{ud}| = 0.97408(26)$. Incorporating new $\mathcal{F}t$ values from Ref. [99] changed the latest compilation value only marginally but improved the overall data consistency — the normalized $\chi^2$ decreased from 0.6 to 0.22.

The top row of the CKM matrix now fulfills the unitarity condition perfectly. The sum-squared of the top row (see Eq. (2.33))

$$V_{ud}^2 + V_{us}^2 + V_{ub}^2 = 0.9998(10), \tag{6.2}$$

which is in excellent agreement with Standard Model expectations. The element $V_{ub}^2$ is so small that it does not contribute to the sum at all.

The change in the last two decades in $V_{ud}^2$, $V_{us}^2$ and in the sum of the three top-row matrix elements of the CKM matrix are plotted in Fig. 6.10. Since 1990, the precision of $V_{ud}^2$ has improved by a factor of four and that of the sum-squared of the top-row, doubled. At the moment the limiting factors are the theoretical corrections and in order to improve these, high-precision experimental information is needed for emitters that have large theoretical corrections — especially $T_z = -1$ emitters and emitters with $A > 62$.

# 7 Summary and outlook

In total, 8 superallowed $Q_{\mathrm{EC}}$ values were measured with high precision. Additionally, several isomeric excitation energies were measured. The IGISOL facility has proven to be a powerful tool in these studies since the nuclei studied in this work are close to stability and are easy to produce in vast quantities. Some of these are refractory elements and can only be extracted as ISOL beams at IGISOL. What is also important is the easy access to the daughter nuclei which are simultaneously available in the beam. The $Q_{\mathrm{EC}}$ value measurement could be done by directly measuring the frequency — and thus mass — ratio of the parent and daughter ions. This has a huge impact on the obtained precision since most of the systematical errors cancel out. Having both the parent and the daughter simultaneously available as an ion beam is not at all trivial for other radioactive ion beam facilities. So far, only the $Q_{\mathrm{EC}}$ value of $^{46}$V by Savard *et al.* [96] has been measured as a doublet. Other Penning trap results have been obtained by measuring the absolute masses and usually only the parent nucleus has been measured.

The Ramsey cleaning method proved to be a very efficient way of removing isomeric contaminants from the trap. A cleaning time of only 200 ms was needed to separate and remove the isomeric state of $^{54}$Co ($\Delta E \approx 200$ keV or 7.5 Hz), leaving a clean sample of the ground state to be measured. This cleaning method has then been used several times to separate the unwanted isomeric or contaminant states. The isomerically clean samples of ions are not only available for mass determinations but also for post-trap decay spectroscopy.

The $Q_{\mathrm{EC}}$ value measurements will be continued in the future. The light cases $^{10}$C, $^{14}$O, $^{34}$Cl and $^{38}$K$^{m}$ remain to be measured with JYFLTRAP in the near future. The beamtime is already approved for these measurements. The $^{10}$C and $^{14}$O cases will be challenging due to contaminating beams from IGISOL. One possibility might be to transform the ions of interest into molecular ions and thus avoid possible contamination. Another possibility might be to use a cryogenic ion guide at liquid nitrogen temperature and freeze out or at least suppress most of the contaminants.

The obtainable precision can be still improved. Using time-separated oscillatory fields was a step in the right direction as the resolution could be improved by almost

a factor of two. The trap electrodes are eight-fold segmented which enables octupolar excitation to be applied in the future. Even a factor of ten improvement has been reported but the excitation procedure is not yet fully understood. Also the charge state of the measured ions could be increased. Since the cyclotron frequency is directly proportional to the charge of the ion, the precision will increase as well. Some studies with doubly-charged ions have already been performed at JYFLTRAP with promising results.

# A The potential used for time-of-flight calculation

Approximated electric and magnetic fields were used in calculation of time-of-flight of ions from the precision trap to the MCP detector. The analytical formula given in eq. (5.1) is used to calculate total time-of-flight. Electric field is assumed to be constant over electrodes, so

$$E_k(x) = E_k, x \in [a_k, b_k], \tag{A.1}$$

where $a_k$ and $b_k$ are the starting and ending location of the $k$th electrode. The magnetic field $B$ is approximated with a second order polynomial such that

$$B_k(x) = B_{0k} + B_{1k}x + B_{2k}x^2, x \in [a_k, b_k] \tag{A.2}$$

inside boundary $a_k$ and $b_k$. The following table A.1 shows all parameters for calculating time of flight properly. The shape of the fields can be seen in figs. 5.1 and 5.2.

**Table A.1:** The electric potential and magnetic flux density values of the trap extraction side for time-of-flight calculations. Given are the starting and ending locations $a_k$ and $b_k$, respectively, and different values for constant $E$-field and second order polynomial for $B$-field calculation. The constants $a$-$i$ are given in table A.2.

| $a_k$ | $b_k$ | $E_k$ | $B_{0k}$ | $B_{1k}$ | $B_{2k}$ | description |
|---|---|---|---|---|---|---|
| 0 | 10 | -1 | 7 | 0 | 0 | Ring electrode |
| 10 | 23 | -1 | 7 | 0 | 0 | correction 1 |
| 23 | 30 | -1 | 7 | 0 | 0 | correction 2 |
| 30 | 52 | -1 | 7 | 0 | 0 | endcap 1 |
| 52 | 75 | -1 | $a$ | $b$ | $c$ | endcap 2 |
| 75 | 98 | -2 | $a$ | $b$ | $c$ | endcap 3 |
| 98 | 256 | -3 | $a$ | $b$ | $c$ | drift 1 |
| 256 | 321 | -4 | $d$ | $e$ | $f$ | drift 2 |
| 321 | 418 | -4 | $d$ | $e$ | $f$ | drift 3 |
| 418 | 450 | -4 | $d$ | $e$ | $f$ | drift 4 (1/2) |
| 450 | 585 | -4 | $g$ | $h$ | $i$ | drift 4 (2/2) |
| 585 | 700 | -120 | $g$ | $h$ | $i$ | extraction 1 |
| 700 | 780 | -1500 | 0.05 | 0 | 0 | extraction 2 |
| 780 | 1600 | -30000 | 0.02 | 0 | 0 | earth-ground |

**Table A.2:** Constants for table A.1.

| constant | value |
|---|---|
| $a$ | 6.543833 |
| $b$ | 0.011493 |
| $c$ | $-8.444330\times10^{-5}$ |
| $d$ | 16.940540 |
| $e$ | -0.069614 |
| $f$ | $7.393477\times10^{-5}$ |
| $g$ | 3.804822 |
| $h$ | -0.010879 |
| $i$ | $7.909835\times10^{-6}$ |

# B Analysis programs

All the data collected in the $Q_{\mathrm{EC}}$ value measurements have been analysed using self-developed programs. There are two main programs — one for fitting and the other for further processing. Both of the programs have graphical user interfaces. The programs are programmed with C++ with `Gtkmm` graphical libraries which uses `Cairo` for drawings. The fitting procedure can be in some degree automatized so that a series of resonance curves can be fitted consecutively without user interference. Some tasks can be automatized using a simple settingfile. The fitting program outputs fitting results to a text file which can be later imported for instance to Open Office Spreadsheets. A screenshot of the fitting program is shown in Fig. B.1.

The other program is for interpolating the reference frequencies and to calculate the final frequency ratios, $Q_{\mathrm{EC}}$ values and such. Also it is a convenient program to quickly plot different fit parameters and see how those vary from one resonance to other and also how reference parameters differ from the ion-of-interest parameters. A screenshot of the post-processing program is in Fig. B.2.

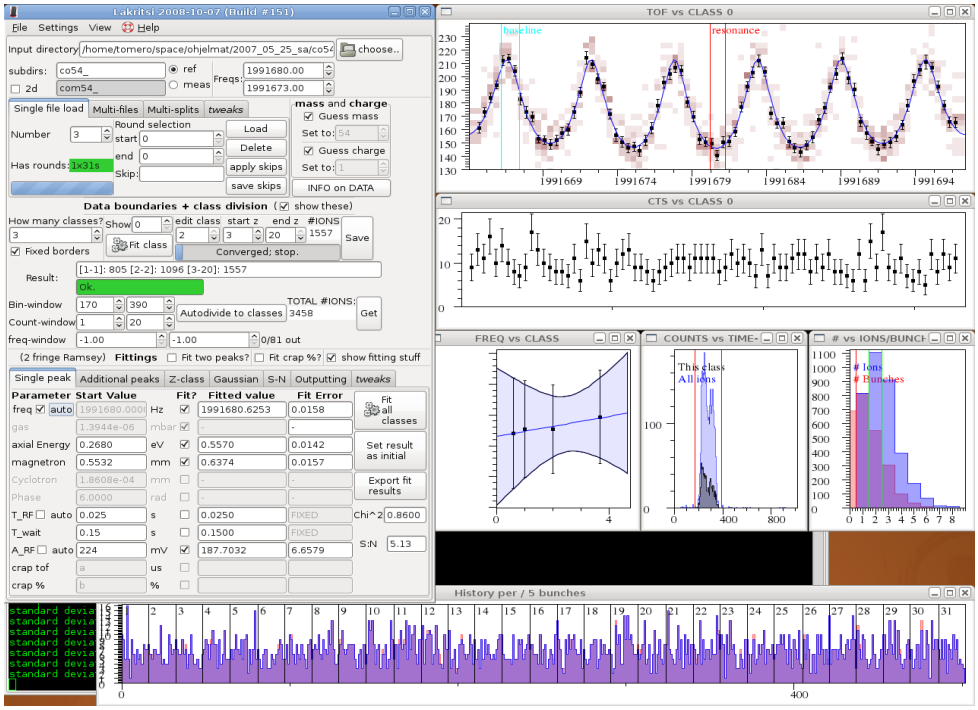


**Figure B.1:** Screenshot of the analysis program. A Ramsey resonance of $^{54}$Co is being fitted with three countrate classes. This resonance only consists of single ions detected per cycle. Time-of-flight gate of 170–390 bins (1 bin = 0.640 $\mu$s) is used. Signal-to-noise ratio for this resonance is about 5.

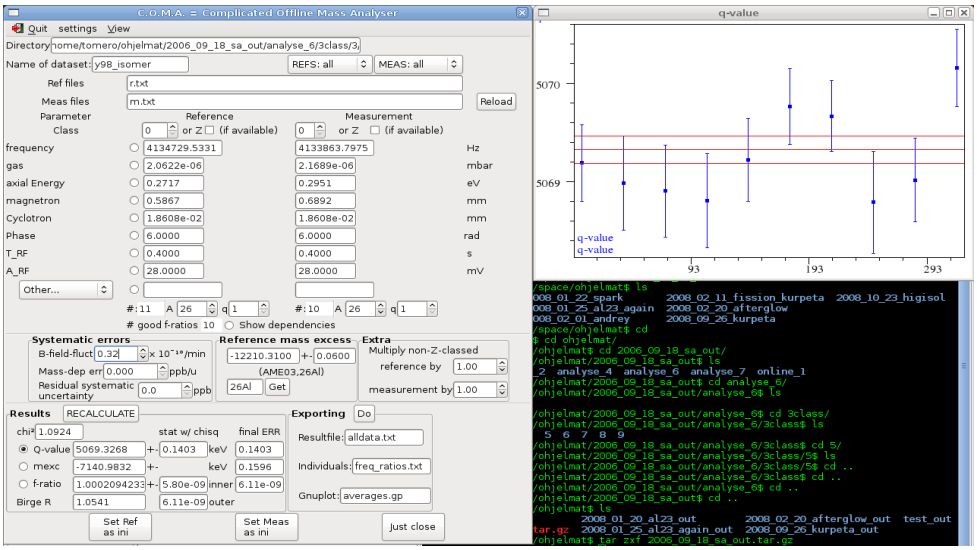


**Figure B.2:** Screenshot of the post-processing program. Various information for the dataset is shown. The $Q_{\mathrm{EC}}$ values calculated from individual resonances are shown on the smaller window.

# Bibliography


[1] J. C. Hardy and I. S. Towner, Phys. Rev. C **71**, 055501 (2005).

[2] G. Audi, Nucl. Phys. A **729**, 337 (2003).

[3] C. B. Collins, C. D. Eberhard, J. W. Glesener, and J. A. Anderson, Phys. Rev. C **37**, 2267 (1988).

[4] D. G. Raich *et al.*, Z. Phys. A **279**, 301 (1976).

[5] A. Piechaczek *et al.*, Phys. Rev. C **62**, 054317 (2000).

[6] D. N. Poenaru and M. Ivascu, J. Phys. G: Nucl. Phys. 965 (1981).

[7] C. Rauth *et al.*, Phys. Rev. Lett. **100**, 012501 (2008).

[8] B. Blank and M. Ploszajczak, Rep. Prog. Phys. **71**, 046301 (2008).

[9] V. Tretyak and Y. Zdesenko, Phys. At. Nucl. **66**, 514 (2003).

[10] A. Serebrov *et al.*, Phys. Lett. B **605**, 72 (2005).

[11] P. J. Brussaard and P. W. M. Glaudemans, *Shell-Model Applications in Nuclear Spectroscopy* (North-Holland, Amsterdam, 1977).

[12] I. S. Towner and J. C. Hardy, Phys. Rev. C **77**, 025501 (2008).

[13] X. D. Liu *et al.*, Phys. Rev. C **69**, 064313 (2004).

[14] E. P. Wigner, *Proceedings of the Robert A. Welch Conferences on Chemical Research*, edited by W. O. Milligan (Robert A. Welch Foundation, Houston, Texas, 1958), Vol. 1, p. 67.

[15] S. Weinberg and S. B. Treiman, Phys. Rev. **116**, 465 (1959).

[16] A. Sirlin, Phys. Rev. **164**, 1767 (1967).

[17] I. S. Towner and J. C. Hardy, Phys. Rev. C **66**, 035501 (2002).

[18] W. J. Marciano and A. Sirlin, Phys. Rev. Lett. **96**, 032002 (2006).

[19] H. Behrens and W. Bühring, *Electron radial wave functions and nuclear beta-decay* (Clarendon press, Oxford, 1982).

[20] W. Bambynek *et al.*, Rev. Mod. Phys. **49**, 77 (1977).

[21] W.-M. Yao *et al.*, J. Phys. G: Nucl. Part. Phys. **33**, 1 (2006).

[22] S. Eidelman *et al.*, Phys. Lett. B **592**, 1 (2004).

[23] J. Charles *et al.*, Eur. Phys. J. C **41**, 1 (2005).

[24] C. Amsler *et al.*, Physics Letters B **667**, 1 (2008).

[25] D. Počanić *et al.*, Phys. Rev. Lett. **93**, 181803 (2004).

[26] O. Naviliat-Cuncic and N. Severijns, arXiv:0809.0994v1 (2008).

[27] N. Severijns, M. Tandecki, T. Phalet, and I. Towner, arXiv:0807.2201v1 (2008).

[28] V. Kozlov *et al.*, Int. J. Mass Spectrom. **251**, 159 (2006).

[29] M. Bhattacharya *et al.*, Phys. Rev. C **77**, 065503 (2008).

[30] K. Blaum *et al.*, Phys. Rev. Lett. **91**, 260801 (2003).

[31] L. S. Brown and G. Gabrielse, Rev. Mod. Phys. **58**, 233 (1986).

[32] H. Dehmelt, Rev. Mod. Phys. **62**, 525 (1990).

[33] V. Kolhinen *et al.*, Nucl. Instrum. Methods Phys. Res., Sect. B **266**, 4547 (2008).

[34] S. Rahaman *et al.*, Int. J. Mass Spectrom. **251**, 146 (2006).

[35] L. S. Brown and G. Gabrielse, Phys. Rev. A **25**, 2423 (1982).

[36] M. König *et al.*, Int. J. Mass Spectrom. Ion Processes **142**, 95 (1995).

[37] G. Gräff, H. Kalinowsky, and J. Traut, Z. Phys. A **297**, 35 (1980).

[38] M. Kretzschmar, Int. J. Mass Spectrom. **264**, 122 (2007).

[39] S. George *et al.*, Int. J. Mass Spectrom. **264**, 110 (2007).

[40] N. F. Ramsey, Rev. Mod. Phys. **62**, 541 (1990).

[41] I. I. Rabi, J. R. Zacharias, S. Millman, and P. Kusch, Phys. Rev. **53**, 318 (1938).

[42] I. I. Rabi, J. R. Zacharias, S. Millman, and P. Kusch, Phys. Rev. **55**, 526 (1939).

[43] J. M. B. Kellogg, I. I. Rabi, N. F. Ramsey, and J. R. Zacharias, Phys. Rev. **55**, 729 (1939).

[44] J. M. B. Kellogg, I. I. Rabi, N. F. Ramsey, and J. R. Zacharias, Phys. Rev. **56**, 728 (1939).

[45] J. M. B. Kellogg, I. I. Rabi, N. F. Ramsey, and J. R. Zacharias, Phys. Rev. **57**, 677 (1940).

[46] G. Bollen *et al.*, Nucl. Instrum. Methods Phys. Res., Sect. B **70**, 490 (1992).

[47] S. George *et al.*, Phys. Rev. Lett. **98**, 162501 (2007).

[48] S. George *et al.*, to be submitted, 2008.

[49] R. Ringle *et al.*, Int. J. Mass Spectrom. **262**, 33 (2007).

[50] S. Eliseev *et al.*, Int. J. Mass Spectrom. **262**, 45 (2007).

[51] E. Kugler, Hyperfine Interact. **129**, 23 (2000).

[52] M. Dombsky *et al.*, Rev. Sci. Instrum. **71**, 978 (2000).

[53] M. V. Ricciardi *et al.*, Nucl. Phys. A **701**, 156 (2002).

[54] M. Mukherjee *et al.*, Eur. Phys. J. A **35**, 1 (2008).

[55] J. Dilling *et al.*, Int. J. Mass Spectrom. **251**, 198 (2006).

[56] M. Smith *et al.*, Phys. Rev. Lett. **101**, 202501 (2008).

[57] J. Wang *et al.*, Nucl. Phys. A **746**, 651 (2004).

[58] H. Geissel *et al.*, Nucl. Instrum. Methods Phys. Res., Sect. B **70**, 286 (1992).

[59] D. J. Morrissey *et al.*, Nucl. Instrum. Methods Phys. Res., Sect. B **204**, 90 (2003).

[60] T. Kubo, Nuclear Instruments and Methods in Physics Research Section B: Beam Interactions with Materials and Atoms **204**, 97 (2003).

[61] S. Schwarz *et al.*, Hyperfine Interact. **173**, 113 (2006).

[62] J. Äystö, Nucl. Phys. A **693**, 477 (2001).

[63] J. Huikari *et al.*, Nucl. Instrum. Methods Phys. Res., Sect. B **222**, 632 (2004).

[64] P. Karvonen *et al.*, Nucl. Instrum. Methods Phys. Res., Sect. B **266**, 4794 (2008).

[65] J. Huikari *et al.*, Hyperfine Interact. **127**, 511 (2000).

[66] A. Nieminen *et al.*, Phys. Rev. Lett. **88**, 094801 (2002).

[67] V. S. Kolhinen *et al.*, Nucl. Instrum. Methods Phys. Res., Sect. A **528**, 776 (2004).

[68] A. Nieminen, Ph.D. thesis, University of Jyväskylä, 2002.

[69] B. Cheal *et al.*, Phys. Lett. B **645**, 133 (2007).

[70] H. Raimbault-Hartmann *et al.*, Nucl. Instrum. Methods Phys. Res., Sect. B **126**, 378 (1997).

[71] J. V. Roosbroeck *et al.*, Phys. Rev. Lett. **92**, 112501 (2004).

[72] K. Blaum *et al.*, Europhys. Lett. **67**, 586 (2004).

[73] K. Blaum *et al.*, J. Phys. B: At., Mol. Opt. Phys. **36**, 921 (2003).

[74] R. Ringle *et al.*, Int. J. Mass Spectrom. **263**, 38 (2007).

[75] A. Bey *et al.*, Eur. Phys. J. A **36**, 121 (2008).

[76] S. Rinta-Antila *et al.*, Eur. Phys. J. A **31**, 1 (2006).

[77] J. Kurpeta *et al.*, Eur. Phys. J. A **31**, 263 (2007).

[78] I. Matea *et al.*, Eur. Phys. J. A **37**, 151 (2008).

[79] S. Rahaman *et al.*, Acta Phys. Pol. B **39**, 463 (2008).

[80] S. Guan and A. G. Marshall, Int. J. Mass Spectrom. Ion Processes **157-158**, 5 (1996).

[81] G. Bollen *et al.*, Nucl. Instrum. Methods Phys. Res., Sect. A **368**, 675 (1996).

[82] J. Clark *et al.*, Nucl. Instrum. Methods Phys. Res., Sect. B **204**, 487 (2003).

[83] P. Schury *et al.*, Eur. Phys. J. A **25(S1)**, 51 (2005).

[84] K. Blaum *et al.*, Hyp. Int. **162**, 173 (2005).

[85] T. A. Carlson, C. W. Nestor, T. C. Tucker, and F. B. Malik, Phys. Rev. **169**, 27 (1968).

[86] A. Kellerbauer *et al.*, Eur. Phys. J. D **22**, 53 (2003).

[87] G. Bollen *et al.*, Phys. Rev. C **46**, R2140 (1992).

[88] S. Rahaman *et al.*, Eur. Phys. J. A **34**, 5 (2007).

[89] A. Chaudhuri *et al.*, Eur. Phys. J. D **45**, 47 (2007).

[90] V.-V. Elomaa *et al.*, Nucl. Instrum. Methods Phys. Res., Sect. B **266**, 4425 (2008).

[91] V.-V. Elomaa *et al.*, to be published (2008).

[92] U. Hager, Ph.D. thesis, University of Jyväskylä, 2007.

[93] R. T. Birge, Phys. Rev. **40**, 207 (1932).

[94] P. Finlay *et al.*, Phys. Rev. C **78**, 025502 (2008).

[95] T. Eronen *et al.*, Phys. Lett. B **636**, 191 (2006).

[96] G. Savard *et al.*, Phys. Rev. Lett. **95**, 102501 (2005).

[97] T. Eronen *et al.*, Phys. Rev. Lett. **97**, 232501 (2006).

[98] H. Vonach *et al.*, Nucl. Phys. A **278**, 189 (1977).

[99] T. Eronen *et al.*, Phys. Rev. Lett. **100**, 132502 (2008).

[100] M. Mukherjee *et al.*, Phys. Rev. Lett. **93**, 150801 (2004).

[101] F. Herfurth *et al.*, Eur. Phys. J. A **15**, 17 (2002).

[102] G. Savard *et al.*, Phys. Rev. C **70**, 042501 (2004).

[103] G. Bollen *et al.*, Phys. Rev. Lett. **96**, 152501 (2006).

[104] P. Schury *et al.*, Phys. Rev. C **75**, 055801 (2007).

[105] P. M. Endt, Nucl. Phys. A **633**, 1 (1998).

[106] V. T. Koslowsky *et al.*, Nucl. Phys. A **472**, 419 (1987).

[107] S. A. Brindhaban and P. H. Barker, Phys. Rev. C **49**, 2401 (1994).

[108] F. Zijderhand, R. C. Makkus, and C. Van Der Leun, Nucl. Phys. A **466**, 280 (1987).

[109] S. W. Kikstra *et al.*, Nucl. Phys. A **496**, 429 (1989).

[110] P. M. Endt, Nucl. Phys. A **521**, 1 (1990).

[111] G. Savard *et al.*, private communication, 2008.

[112] G. T. A. Squier *et al.*, Phys. Lett. B **65**, 122 (1976).

[113] T. Faestermann *et al.*, arXiv:0810.3437v1 (2008).

[114] J. C. Hardy *et al.*, Phys. Rev. Lett. **33**, 320 (1974).

[115] S. D. Hoath *et al.*, Phys. Lett. B **51**, 345 (1974).

[116] C. N. Davids, C. A. Gagliardi, M. J. Murphy, and E. B. Norman, Phys. Rev. C **19**, 1463 (1979).

[117] T. Eronen *et al.*, Phys. Rev. C (submitted) (2008).

[118] A. Parikh *et al.*, Phys. Rev. C **71**, 055804 (2005).

[119] J. C. Hardy *et al.*, Phys. Rev. C **9**, 252 (1974).

[120] V. E. Iacob *et al.*, Phys. Rev. C **77**, 045501 (2008).

[121] K. G. Leach *et al.*, Phys. Rev. Lett. **100**, 192504 (2008).

[122] J. C. Hardy *et al.*, Nucl. Phys. A **509**, 429 (1990).